VOLUME 3 NUMBER 1 2016 ISSN 2409-6121

Physical Sciences and Technology

National Nano Laboratory of Open Type
Research Institute of Experimental and Theoretical Physics

Physical Sciences and Technology is publishing two number in a year by al-Farabi Kazakh National University, al-Farabi ave., 71, 050040, Almaty, the Republic of Kazakhstan
website: http://phst.kaznu.kz/

Any inquiry for subscriptions should be send to:
Abdiadil Askaruly, al-Farabi Kazakh National University
al-Farabi ave., 71, 050040, Almaty, the Republic of Kazakhstan
e-mail: Abdiadil.Askaruly@kaznu.kz

SCOPE AND AIM

Physical Sciences and Technology provides an original paperback for the publication of peer-reviewed research and review articles in all fields of Physics and related Technology. The topics, included in the scope, especially emphasize understanding of the physics underlying modern technology.

Subject areas may include, but are not limited to the following fields: Astronomy and Space Research, Theoretical Physics and Astrophysics, Plasma Physics and Related Technology, Chemical Physics and Radio Physics, Condensed Matter Physics and Related Technology, Thermal physics and Related Technology, Nuclear Physics and Related Technology, Nanomaterials and Nanotechnology, Applied Atomic and Molecular Physics, Material Sciences and Related Technology, Electronics and Related Technology, Instrumentation, Photonics and Quantum Electronics, Signal processing.

The Journal is issued under the auspices of the National Nano Laboratory of Open Type and the Research Institute of Experimental and Theoretical Physics and is published two times a year by the "Kazakh University" Publishing House. The International Editorial Board of the Journal consists of leading researchers from different countries of the world. The Journal is wide open for contributions that both lie at the far frontiers of contemporary physics and are particularly aimed at applications of the scientific principles of physics to modern technological problems.

ABOUT WORKSHOP 2016

The 3rd International Workshop«Nuclear Physics and Astrophysics»follows the series of 2012 and 2014, which were in Almaty, Kazakhstan.

The main aim of workshop: the main purpose is to increase the research of young scientists and the development of scientific disciplines and collaboration with experienced scientists of international level.

The International Workshop «Nuclear Physics and Astrophysics», organized by the Chair of Theoretical and Nuclear Physics, Physical-Technical Faculty and the Institute for Experimental and Theoretical Physics of the al-Farabi Kazakh National University will take place on April 14 – 16, 2016 at the Physical-Technical Faculty of the al-Farabi Kazakh National University, Almaty, Kazakhstan.

Co-organizers: Institute of Nuclear Physics of the Republic of Kazakhstan, National Center for Space Research and Technologies, Fesenkov' Astrophysical Institute, Almaty, Kazakhstan

Workshop Language - English. All reports, abstracts and papers accepted for publication are to be in English. The papers for publication in the journal abroad will be peer reviewed.

International Organizing committee: Bum-Hoon Lee (Asia Pacific Center for Theoretical Physics, Republic of Korea), Kiyoshi Kato (Hokkaido University, Japan), Shinsho Oryu (Tokyo University of Science, Japan), Roman Kezerashvili (New-York City University, USA), V.S. Vasilevsky (Bogolyubov Institute for Theoretical Physics, Ukraine), R. Ruffini (ICRANET Sapiensa, University of Roma, Italy), K. Spitaleri (University of Catania, Italy), ChingisOmarov (National Center of Space Researches and Technologies; Fesenkov' Astrophysical Institute, Almaty, Kazakhstan), S. Sakhiev (Institute of Nuclear Physics, Almaty, Kazakhstan), V.N.Melnikov (Russia, MSU, RUDN), T. S. Ramazanov, T.A. Kozhamkulov, A.E. Davletov, M.E.Abishev, N.Takibayev (al-FarabiKazNU, Almaty, Kazakhstan).

Local Organizing committee: N.Zh. Takibayev (chair) E-mail: takibayev@gmail.com, V. Kurmangaliyeva (scientific secretary), M.E. Abishev, B. Abdykadyrov, K. Boshkayev, A. Duisenbay, Zh. Omar (al-Farabi Kazakh National University, Almaty, Kazakhstan)

The scientific secretary of the Organizing committee (E-mail: venera_baggi@mail.ru) the names of the authors, titles and abstracts of your talks (not more than 1 page for one report).

The International Workshop will cover areas like nuclear cluster physics, few-body systems, light nuclei and nuclear reactions in astrophysics, physics of neutron stars and white dwarfs, galaxies and other aspects of modern problems of nuclear physics and astrophysics.

Venue: Conference room – room № **330**, Physical-Technical Faculty, al-FarabiKazNU, av. al-Farabi 71, Almaty

The Workshop was supported by Physical-Technical Department of al-Farabi Kazakh National University

List of III International Workshop participants:

V.S. Vasilevsky Bogolyubov Institute for Theoretical Physics, Kiev, Ukraine

M. Ito Department of Pure and Applied Physics, Kansai University, 3-3-35; Yamatecho, Suita, Osaka 564-8680, Japan.

K. Katō Nuclear Reaction Data Centre, Faculty of Science, Hokkaido University, Sapporo, Japan

S. Yamaki Nishina Center, RIKEN, Wako, Saitama 351-0198, Japan

Daiki Nishimura Department of Physics, Tokyo University of Science, Noda, Chiba 278-8510, Japan

Claudio Spitaleri Department of Physics and Astromomy, University of Catania, Catania, Italy and INFN-Laborator

Nurgali Takibayev Al-Farabi Kazakh National University, Almaty, Kazakhstan

Marzhan Nassurlla Al-Farabi Kazakh National University, Almaty, Kazakhstan

Daniyar Janseitov ENU, Astana, Kazakhstan

ISBN 978-601-04-1790-8

ErnazarAbdikamalov Nazarbayev University, Astana, Kazakhstan
Daniele Malafarina Nazarbayev University, Astana, Kazakhstan
P. Krasovitsky Institute of Nuclear Physics, Almaty, Kazakhstan
Kabatayeva R.S. Kazakh National University named after Al-Farabi, Almaty, Kazakhstan
M. Abishev Kazakh National University named after Al-Farabi, Almaty, Kazakhstan
S.Kunakov International IT University, Almaty, Kazakhstan
F.Sagimbaeva Joint institute for nuclear research, Dubna, Russia
B.Baimurzinova Joint institute for nuclear research, Dubna, Russia
V. Dzhunushaliev Kazakh National University named after Al-Farabi, Almaty, Kazakhstan
Z.Zh.Zhanabaev Kazakh National University named after Al-Farabi, Almaty, Kazakhstan

List of participants who presented reports and video-materials via Skype connection:
H. Quevedo National Autonomous University of Mexico and University of Rome
K. Boshkayev Kazakh National University named after Al-Farabi, Almaty, Kazakhstan
YuliyaLashko Bogolyubov Institute for Theoretical Physics, Kiev, Ukraine
Roman Kezerashvili Physics Department, The City University of New York, Brooklyn, NY 11201, USA; The Graduate School and University Center, New York, NY 10016, USA

The 3rd International Workshop «Nuclear Physics and Astrophysics»
al-Farabi Kazakh National University, Almaty, Kazakhstan, April 14-16, 2016. – Almaty: Kazakh University, 2016 – 48 p.

UDC 539

Photodisintegration and Virtual State in the Complex Scaling Method

Kato K.[1*], Odsuren M.[2], Kikuchi Y.[3], Myo T.[4], Vasilevsky V.S.[5], Takibayev N.[6]

[1]*Nuclear Reaction Data Centre, Faculty of Science, Hokkaido University, Sapporo 060-0810, Japan*
[2]*School of Engineering and Applied Sciences, National University of Mongolia, Ulaanbaatar 14200, Mongolia* [3]*RIKEN Nishina Center, Wako 351-0198, Japan*
[4]*General Education, Faculty of Engineering, Osaka Institute of Technology, Osaka 535-8585, Japan*
[5]*Bogolyubov Institute for Theoretical Physics, Kiev, Ukraine*
[6]*IETP, Department of Physics and Technology, al-Farabi Kazakh National University, 71 al-Farabi av., 050040 Almaty, Kazakhstan*
[*]*e-mail: kato-iku@gd6.so-net.ne.jp*

The photodisintegration cross section observed just above the neutron threshold energy in ^{9}Be is discussed in the framework of an $\alpha + \alpha + n$ three-cluster model and the complex scaling method. The observed cross sections shows a remarkable sharp peak, which has been discussed in association with photo-neutron reactions in nucleo-syntheses of chemical elements. It is discussed that the enhancement of the peak is understood by taking into account a virtual state but not a resonant state. The complex scaling method cannot reproduce an eigenvalue corresponding to the virtual pole, but provides us with a useful tool for investigation of the photodisintegration cross section.

Key words: photodisintegration cross section, $1/2_1^+$ state of ^{9}Be, virtual state, cluster model, complex scaling method
PACS number(s): 27.20.+n $6 \le A \le 19$, 21.60.Gx, 24.30.Gd, 25.20.Lj

1 Introduction

It is a longstanding problem to determine its resonance energy and width of the first excited $1/2^+$ state of ^{9}Be, which is closely connected with the problem to clarify whether it is a resonant state or not [1 – 7]. Recently, we studied the $1/2^+$ state of ^{9}Be and the photodisintegration cross section (PDXS) applying the complex scaling method (CSM) [8 – 11] to the $\alpha + \alpha + n$ three-cluster model [12, 13]. The results indicate that there is no sharp resonant state corresponding to the distinct peak observed just above the ^{8}Be+n threshold in the photodisintegration cross section of ^{9}Be. On the other hand, the recent experimental cross section data [14 – 16] can be well explained by the $\alpha + \alpha + n$ calculation. From these results, we concluded that the first excited $1/2^+$ state in ^{9}Be is a $^8\mathrm{Be}+n$ virtual state but not resonant one.

The virtual states in nuclear systems have been discussed in the $T = 1$ states of two-nucleon systems for a long time [17, 18], and recently they attract much interest again in association with weak binding problems of neutron rich nuclei [19 – 21]. The low-energy photodisintegration reaction of ^{9}Be has also received much attention from the viewpoint of the astrophysical interest [22, 23]. The photodisintegration cross section has been discussed to be negligibly small in the energy region between thresholds of $\alpha + \alpha + n$ (1.5736 MeV) and $^8\mathrm{Be}+n$ (1.6654 MeV) [14, 15, 16]. The observed cross section above the $^8\mathrm{Be}+n$ shows a prominent peak, although there are some discrepancies among the experimental absolute values. The cross section profile has an asymmetric shape and cannot be explained by a simple resonance formula like the Breit-Wigner form.

In next section, we briefly explain the framework of the $\alpha + \alpha + n$ three-body model and the CSM. In section 3, the results are shown. A conclution is given in section 4.

2 Framework

2.1 α + α + n model

We briefly explain the $\alpha + \alpha + n$ three-body model employed in the present work, whose details are given in Ref. [12]. We here solve the Schrödinger equation for the $\alpha + \alpha + n$ system using the orthogonality condition model [26]. The Schrödinger equation is given as

$$\hat{H}\Psi^{\nu}_{J^{\pi}} = E_{\nu}\Psi^{\nu}_{J^{\pi}}, \qquad (1)$$

where J^π is the total spin and parity of the $\alpha + \alpha + n$ system and v is the index of eigenstates. The energy eigenvalue E_v is measured from the $\alpha + \alpha + n$ threshold of ^{9}Be. The Hamiltonian for the relative motion of the $\alpha + \alpha + n$ three-body system is given as

$$\hat{H} = \sum_{i=1}^{3} t_i - T_{c.m.} + \sum_{i=1}^{2} V_{\alpha n}(\xi_i) + V_{\alpha\alpha} + V_{PF} + V_3, \quad (2)$$

where t_i and $T_{c.m.}$ are kinetic operators for each particle and the center-of-mass of the system, respectively. The interaction between the neutron and the*i*th α particle is given as $V_{\alpha n}(\xi_i)$, where ξ_i is the relative coordinate between them. We here employ the KKNN potential [27] for $V_{\alpha n}$. For the α – α interaction $V_{\alpha\alpha}$ we employ the same potential as used in Ref. [12], which is a folding potential of the effective *NN* interaction and the Coulomb interaction. The pseudopotential $V_{PF} = \lambda |\Phi_{PF}\rangle\langle\Phi_{PF}|$ is the projection operator to remove the Pauli forbidden states from the relative motions of α – α and α – n [28]. The Pauli forbidden state Φ_{PF} is defined as the harmonic oscillator wave functions by assuming the $(0s)^4$ configuration, whose oscillator length is fixed to reproduce the observed charge radius of the α particle. We here take λ as 10^6 MeV.

In the present calculation, we introduces the $\alpha + \alpha + n$ three-body potential V_3. The explicit form of V_3 is given as

$$V_3 = v_3 \exp(-\mu\rho^2), \quad (3)$$

where ρ is the hyper-radius of the $\alpha + \alpha + n$ system. The hyper-radius is defined as $\rho^2 = 2r^2 + (8/9)R^2$, where r is the distance between two α's and R is that between the neutron and the center-of-mass of the α – α subsystem. To reproduce the ground-state properties, we take the strength v_3 and the width μ as 1.10 MeV and 0.02 fm^{-2}, respectively. For other spin-parity states, we employ the same value of μ as used in $3/2^-$ states, but different strengths are used to reproduce the energy positions of the observed peaks in the photodisintegration cross section.

We solve the Schrödinger equation with the coupled rearrangement-channel Gaussian expansion method [29]. In the present calculation, the ^{9}Be wave function $\Phi^v_{J^\pi}$ is described in the Jacobi coordinate system as

$$\Phi^v_{J^\pi} = \sum_{cij} C^v_{cij}(J^\pi)\left[\left[\phi^i_l(r_c)\phi^j_L(R_c)\right]_I, \chi_{1/2}\right]_{J^\pi}, \quad (4)$$

where $C^v_{cij}(J^\pi)$ is a expansion coefficient and $\chi_{1/2}$ is the spin wave function. The relative coordinates$\mathbf{r}_c$ and $\mathbf{R}_c$ are those in three kinds of the Jacobi coordinate systems indexed by c = (1, 2, 3), and the indices for the basis functions are represented as i and j. The spatial part of the wave function is expanded with the Gaussian basis functions [29].

2.2 Complex scaling method

To calculate the photodisintegration cross section, we use the complex scaling method (CSM) [24, 25]. In the CSM, the relative coordinates ξ ($\mathbf{r}_c$ and $\mathbf{R}_c$) are transformed as

$$U(\theta)\xi U^{-1}(\theta) = \xi e^{i\theta}, \quad (5)$$

where $U(\theta)$ is a complex scaling operator and θ is a scaling angle being a real number. Applying this transformation to Eq. (1), we obtain the complex-scaled Schrödinger equation as

$$\hat{H}^\theta \Psi^v_{J^\pi}(\theta) = E^\theta_v \Psi^v_{J^\pi}(\theta). \quad (6)$$

By solving the complex-scaled Schrödinger equation with appropriate L^2 basis functions, we obtain the energy eigenvalues E^θ_v and eigenstates $\Psi^v_{J^\pi}(\theta)$ (their biorthogonal states $\tilde{\Psi}^v_{J^\pi}(\theta)$) [24, 25].

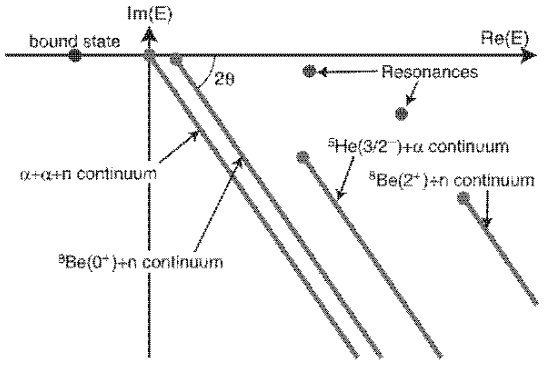

Figure 1 – Schematic picture of energy eigenvalue distribution on the complex energy plane for the $\alpha + \alpha + n$ system

The energy eigenvalues E_ν^θ obtained on the complex energy plane are governed by the ABC theorem [8, 9]. A schematic picture of the energy eigenvalue distribution is shown in Fig. 1. In the CSM, the energies of bound states are given by real numbers and are invariant under the complex scaling. On the other hand, resonances and continuum states are obtained as eigenstates with complex energy eigenvalues. The resonances are obtained as isolated eigenstates on the complex energy plane, whose energies are given as $E_\nu^\theta = E_\nu^r - i\Gamma_\nu/2$. The resonance energies E_ν^r and the decay widths Γ_ν are independent of the scaling angle θ. The complex-scaled continuum states are obtained on branch cuts rotated down by 2θ as shown in Fig. 1. The branch cuts start from the different thresholds for two- and three-body continuum states in the case of the $\alpha + \alpha + n$ system as shown in Fig. 1. This classification of the continuum states is useful in investigation of properties of the ^{9}Be photodisintegration.

Using the energy eigenvalues and eigenstates of the complex-scaled Hamiltonian $\hat{H}^\theta$, we define the complex-scaled Green's function as

$$G^\theta(E;\xi,\xi') = \left\langle \xi \left| \frac{1}{E-\hat{H}^\theta} \right| \xi' \right\rangle = \sum_\nu \int \frac{\Psi^\nu_{J^\pi}(\theta)\tilde{\Psi}^\nu_{J^\pi}(\theta)}{E-E\theta_\nu}. \quad (7)$$

In the derivation of the right-hand side of Eq. (7), we use the extended completeness relation, whose detailed explanation is given in Ref. [30].

We calculate the cross section of ^{9}Be $(3/2^-) + \gamma \to \alpha + \alpha + n$ in terms of the electromagnetic multipole responses. In the present calculation, we focus on the low-lying region of the photodisintegration cross section and take into account only the dipole responses. The photodisintegration cross section σ^γ is given by the sum of those by the $E1$ and $M1$ transitions as

$$\sigma^\gamma(E_\gamma) = \sigma_{E1}(E_\gamma) + \sigma_{M1}(E_\gamma), \quad (8)$$

where E_γ is the incident photon energy. The energy E in Eq. (7) is related to E_γ as $E = E_\gamma - E_{gs}$, where E_{gs} is the binding energy of the ^{9}Be ground state measured from the $\alpha + \alpha + n$ threshold. The cross sections for the electromagnetic dipole transitions σ_{EM1} are expressed as the following form:

$$\sigma_{EM1}(E_\gamma) = \frac{16\pi^3}{9}\left(\frac{E_\gamma}{\hbar c}\right)\frac{dB(EM1,E_\gamma)}{dE_\gamma}. \quad (9)$$

Using the complex-scaled Green's function given in Eq. (7), the electromagnetic dipole transition strength is given as

$$\frac{dB(EM1,E_\gamma)}{dE_\gamma} = -\frac{1}{\pi}\frac{1}{2J_{gs}+1} Im\left[\sum_\nu \int \langle\tilde{\Psi}_{gs}(\theta)\| \hat{O}^\theta_{EM1} \|\Psi^\nu(\theta)\rangle \times \frac{1}{E-E^\theta_\nu}\langle\tilde{\Psi}^\nu(\theta)\| \hat{O}^\theta_{EM1} \|\Psi_{gs}(\theta)\rangle\right], \quad (10)$$

where J_{gs} and Ψ_{gs} (θ) are the total spin and the wave function of the ground state, respectively, and $\hat{O}^\theta_{EM1}$ is an electromagnetic dipole transition operator.

3 Results

We first show the calculated ground-state properties of ^{9}Be and their v_3 dependence. The calculated binding energy and charge and matter radii are listed in Table 1. Without the three-body potential in Eq. (2), the binding energy of the ^{9}Be ground state is overbound and the charge radius is slightly small compared to experiments. To reproduce these quantities, we need the repulsive three-body potential whose parameters are given as $v_3 = 1.10$ MeV and $\mu = 0.02$ fm^{-2}. As results, we reproduce the binding energy and charge radius of the ^{9}Be ground state simultaneously, while the matter radius is slightly larger than the observed one.

Table 1 – ^{9}Be ground-state properties in comparison with experiments. The calculated binding energies E_{gs} in MeV, charge radii R_{ch}, and matter radii R_m with different three-body potential strengths v_3 are listed.

v_3 (MeV)	E_{gs} (MeV)	R_{ch} (fm)	R_m (fm)
.0	2.14	2.50	2.39
.10	1.57	2.53	2.42
exp.	1.5736[32]	2.519 ± 0.012 [33]	2.38 ± 0.01 [34]

Next we confirm that no resonance of the $1/2^+$ state is found with the three-body potential given in Table 1 for the θ = 15° case. We discuss the photodisintegration cross section to $1/2^+$ states. In the present calculation, we fix the ground-state wave function obtained with the three-body potential in Table 1. In Fig. 2, we show the calculated cross sections using Eq. (9) in comparison with the two sets of the observed data [14, 15] which commonly have peaks just above the ^{8}Be $+n$ threshold. The dashed and dotted lines show the cross sections with and without the three-body potential for excited $1/2^+$ states, respectively, whose parameters are the same as those in Table 1. In both results, the calculated cross sections underestimate the low-lying peak above the ^{8}Be $+n$ threshold.

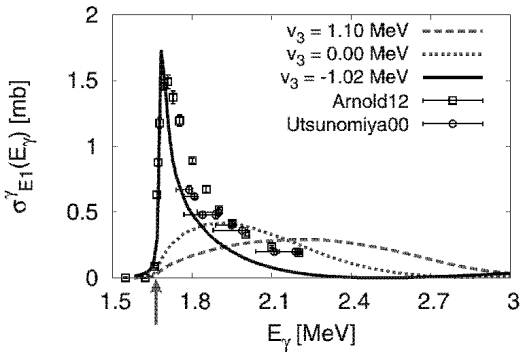

Figure 2 – Calculated photodisintegration cross sections in comparison with experimental data. The arrow indicates the threshold energy of the ^{8}Be(0^+) + n channel

To discuss the observed sharp peak just above the ^{8} Be $+n$ threshold in the photodisintegration cross section, we change the strength v_3 for the $1/2^+$ state to fit the observed data, but its range μ is fixed as the same as used in the ground state. We here take the strength as v_3 = – 1.02 MeV for the $1/2^+$ state and obtain the cross section as shown by the solid line in Fig. 2. Our result reproduces the observed peak by using the attractive three-body potential. The origin of the three-body potential would be a strong state-dependent tensor force and an antisymmetrization of the nucleon among different three clusters. It can be estimated that the tensor force gives a repulsive effect for a p -shell neutron around two α clusters but an attractive one for a higher s-shell neutron [31]. We confirm that the calculated cross section rapidly increases just above the ^{8}Be $+n$ threshold and there is negligibly small strength below this threshold. We also find that the calculated cross sections show the strong dependence on the strengths of the three-body potentials as shown in Fig. 2. This result is interesting and suggests the existence of the three-body unbound state of ^{9}Be$(1/2^+)$, such as a resonance or virtual state. In relation to the cross section, we discuss the character of the $1/2^+$ state.

To see the origin of the low-lying peak above the ^{8}Be $+n$ threshold in more detail, we show the distribution of the energy eigenvalues of the $1/2^+$ states by using the CSM. In the CSM, continuum states are obtained along the branch cuts which start from the threshold energies and are rotated down by 2θ. A resonance is obtained as a solution with a complex energy of $E_\nu^r - i\Gamma_\nu / 2$ which is isolated from the continuum states. However, the virtual states and broad resonances, which are located on the second Riemann sheet covered by the rotated first Riemann sheet, cannot be obtained as the isolated pole in the CSM. The contributions from these states to the cross section are scattered into the continuum states located on the 2θ lines. In Fig. 3, we show the distribution of the energy eigenvalues for the $1/2^+$ states calculated with v_3 = – 1.02 MeV, which reproduces the observed peak as shown in Fig. 2. In the present calculation, we find no resonances in the energy eigenvalue distribution. All energy eigenvalues are located on the 2θ lines, corresponding to the branch cuts for the $\alpha + \alpha + n$, ^{8}Be $(0^+) + n$, and ^{5}He$(3/2^-)$+α continuum states.

We investigate the contributions of two- and three-body continuum states to the cross section to understand the mechanism of the photodisintegration.

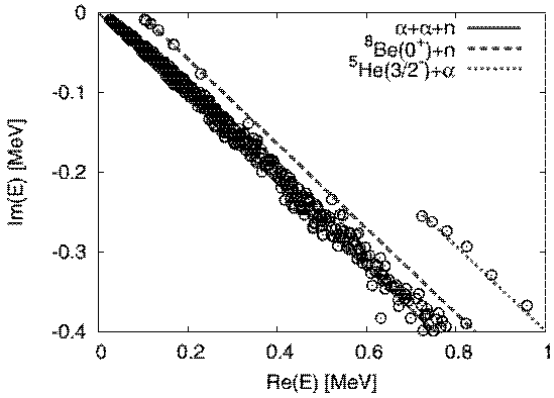

Figure 3 – Distribution of energy eigenvalues of $1/2^+$ states solved with the strength $v_3 = -1.02$ MeV and the scaling angle $\theta = 15^\circ$

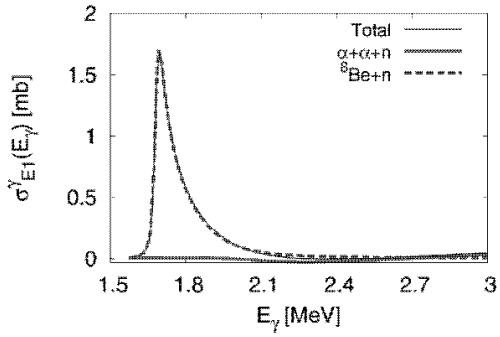

Figure 4 – Decomposed photodisintegration cross sections. The solid and dashed lines are contributions of the $\alpha + \alpha + n$ and ^{8}Be+n continuum states. The black thin line is the same as that in Figure 3

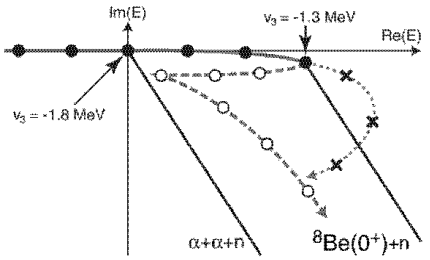

Figure 5 – Pole trajectory of the ^{9}Be $1/2^+$ state in a complex energy plane by changing the three-body potential. The closed circles represent the poles obtained as isolated three-body resonances in CSM. The open circles and crosses are speculated pole positions for the virtual states and broad resonances, respectively

We decompose the cross section calculated with $v_3 = -1.02$ MeV into ^{8}Be$+n$ and $\alpha + \alpha$ components as shown in Fig. 4, to see the dominant contribution in the cross section. The ^{5}He$+\alpha$ contribution is found to be negligible in the low-lying region, and we do not show it in Fig. 4. From Fig. 4, we see that the ^{8}Be$+n$ component is almost identical to the total cross section. This fact indicates that the ^{8}Be+n breakup is dominant in the photodisintegration. This breakup process should be related to the structure of the $1/2^+$ state of ^{9}Be. To investigate the structure of the $1/2^+$ state of ^{9}Be, we calculate the energy eigenvalues of the $\alpha + \alpha + n$ system by changing the strength of the three-body potential v_3, which is shown in Fig. 5. In the present calculation, when the strength of the three-body potential $v_3 = -1.3$ MeV, the resonance pole suddenly appears just below the ^{8}Be$(0^+) + n$ threshold. This resonance pole with a narrow decay width moves smoothly to the bound state region as the three-body potential becomes more attractive, and we finally obtain the ^{9}Be bound state with the region of $v_3 < -1.8$ MeV. On the other hand, we consider the pole trajectory in the opposite case of the three-body potential with $v_3 = -1.3$ MeV. If the resonance exists, the pole with a narrow decay width should appear above the ^{8}Be$+n$ threshold as the analytical continuation from the resonance pole as shown with the crosses in Fig. 5. However, we found that no resonances appear above the ^{8}Be$(0^+) + n$ threshold for $v_3 = -1.3$ MeV of the three-body potential. These facts in the pole trajectory show the possibility of the virtual state of the $1/2^+$ state consisting of ^{8}Be$(0^+) + n$ when we take $v_3 = -1.02$ MeV, which reproduces the experimental cross section. The existence of the virtual state is consistent with the dominant decay into ^{8}Be + n in the photodisintegration of ^{9}Be.

4 Conclusion

We investigate the character of the $1/2^+$ state of ^{9}Be using the photodisintegration reaction with the $\alpha + \alpha + n$ three body model and the CSM. The calculated photodisintegration cross sections into the $1/2^+$ states are shown to have a strong dependence on the strength of the three-body potential for the $1/2^+$ state. The experimental cross section shows a sharp peak just above the ^{8}Be$+n$ threshold, which is nicely reproduced with the attractive three-body potential. We cannot find any resonance poles for the $1/2^+$ states in explaining the peak in the cross section. From the decomposition of the calculated cross section, it is shown that the ^{8}Be $+n$ continuum states dominate the cross section to the $1/2^+$ states. These results indicate the possibility of the virtual-state nature of the first excited $1/2^+$ state. In addition, the pole trajectory suggests that the pole of the $1/2^+$ state is located on the second Riemann sheet of ^{8}Be$+n$ instead of the broad resonances of $\alpha + \alpha + n$.

Acknowledgements

This work was supported by JSPS KAKENHI Grants No. 25400241 and No. 15K05091. The authors are also thankful for the support of the International Collaboration with Al-Farabi Kazakh National University (Grants No. 3106/GF4 and No. 1550/GF3).

References

[1] F. C. Barker. Consistent Description of Unbound States Observed in Scattering and Reactions // Aust. J. Phys. – 1988. – Vol. 41. – P. 743-764.

[2] F. C. Barker. The Low-energy 9Be(γ, n) 8Be Cross Section // Aust. J. Phys. – 2000. – Vol. 53. – P.247-257.

[3] V. Efros and J. Bang. The first excited states of 9Be and 9B // Eur. Phys. J. A. – 1999. – Vol. 4. – P. 33-39.

[4] V. D. Efros, P. von Neumann-Cosel, and A.Richter. Properties of the first excited state of 9Be derived from (γ,n) and (e,e′) reactions // Phys. Rev. C. – 2014. – Vol. 89. – P. 027301.

[5] K. Arai, P. Descouvemont, D. Baye, and W. N. Catford. Resonance structure of 9Be and 9B in a microscopic cluster model // Phys. Rev. C. – 2003. – Vol.68. – P. 014310.

[6] E. Garrido, D. Fedorov, and A. Jensen. Above threshold s-wave resonances illustrated by the 1/2+ states in 9Be and 9B // Phys. Lett. B. – 2010. – Vol. 684. – P.132-136.

[7] R.Álvarez-Rodr uez, A.S. Jensen, E. Garrido, and D. V. Fedorov. Structure and three-body decay of 9Be resonances // Phys. Rev. C. – 2010. – Vol. 82. – P. 034001.

[8] J. Aguilar and J. M. Combes. A class of analytic perturbations for one-body Schrödinger Hamiltonians // Commun. Math. Phys. – 1971 – Vol. 22. – P. 269-279.

[9] E. Balslev and J. M. Combes. Spectral properties of many-body Schrödinger operators with dilatation-analytic interactions // Commun. Math. Phys. – 1971. – Vol. 22. – P. 280-294.

[10] Y. K. Ho. The method of complex coordinate rotation and its applications to atomic collision processes // Phys. Rep. – 1983. – Vol. 99. – P. 1-68.

[11] N. Moiseyev. Quantum theory of resonances: calculating energies, widths and cross-sections by complex scaling // Phys. Rep. – 1998. – Vol. 302. – P.211-293.

[12] M. Odsuren, Y. Kikuchi, T. Myo, M. Aikawa, and K. Kat . Virtual-state character of the 9Be 1/2+ state in the 9Be(γ,n) 8Be reaction // Phys. Rev. C. – 2015. – Vol.92. – P. 014322.

[13] Y. Kikuchi, M. Odsuren, T. Myo, and K. Kat. Photodisintegration cross section of 9Be up to 16 MeV in the α + α + n three-body model // Phys. Rev. C. – 2016. – Vol. 93. – P. 054605.

[14] C. W. Arnoldet al. Cross-section measurement of 9Be(γ,n)8Be and implications for α+α+n→9Be in the r process // Phys. Rev. C. – 2012. – Vol. 85. – P. 044605.

[15] H. Utsunomiyaet al. Photodisintegration of 9Be through the 1/2+ state and cluster dipole resonance // Phys. Rev. C. – 2015. – Vol. 92. – P.064323.

[16] H. Utsunomiya et al. Photodisintegration of 9Be with laser-induced Compton backscattered γ rays // Phys. Rev. C. – 2000. – Vol. 63. – P. 018801.

[17] H. A. Bethe. Eementary Nuclear Theory. – John Wiley and Sons, Inc.: New York, 1947, – 148 p.

[18] S. T. Ma. Interpretation of the Virtual Level of the Deuteron // Rev. Mod. Phys. – 1953. – Vol. 25. – P.853-860.

[19] I.J. Thompson, M.V. Zhukov. Effects of 10Li virtual states on the structure of 11Li // Phys. Rev. C. – 1994. – Vol. 49. – P. 1904-1907.

[20] F.C. Barker, G.T. Hickey. Ground-state configurations of 10Li and 11Li // J. Phys. G. – 1977. – Vol. 3. – P. L23.

[21] H. Masui, S. Aoyama, T. Myo, K. Kat, and K.Ikedad. Study of virtual states in 5He and 10Li with the Jost function method // Nucl. Phys. A. – 2000. – Vol. 673. – P. 207-218.

[22] S. E. Wooseley, R. D. Hoffman. The alpha-process and the r-process. // Astrophys. J. – 1992. – Vol. 395. – P. 202-239.

[23] T. Sasaqui, K. T. Kajino, G. Mathews, K. Otsuki, and T. Nakamura. Sensitivity of r-Process Nucleosynthesis to Light-Element Nuclear Reactions // Astrophys. J. – 2005. – Vol. 634. – P. 1173-1189.

[24] S. Aoyama, T. Myo, K. Kat , and K. Ikeda. The Complex Scaling Method for Many-Body Resonances and Its Applications to Three-Body Resonances // Prog. Theor. Phys. – 2006. – Vol. 116. – P. 1-35.

[25] T. Myo, Y. Kikuchi, H. Masui, and K. Kat . Recent development of complex scaling method for many-body resonances and continua in light nuclei // Prog. Part. Nucl. Phys. – 2014. – Vol. 79. – P. 1-56.

[26] S. Saito. Interaction between Clusters and Pauli Principle // Prog. Theor. Phys. – 1969. – Vol. 41. – P.705-722.

[27] H. Kanada, T. Kaneko, S. Nagata, and M.Nomoto. Microscopic Study of Nucleon-4He Scattering and Effective Nuclear Potentials // Prog. Theor. Phys. 1979. – Vol. 61. – 1327-1341.

[28] V. I. Kukulin, V. M. Krasnopol'sky, V. T. Voronchev, and P. B. Sazonov. Detailed study of the cluster structure of light nuclei in a three-body model: (II). The spectrum of low-lying states of nuclei with A = 6 // Nucl. Phys. A. – 1986. – Vol. 453. – P. 365-388.

[29] E. Hiyama, Y. Kino, and M. Kamimura. Gaussian expansion method for few-body systems // Prog. Part. Nucl. Phys. – 2003. – Vol. 51. – P. 223-307.

[30] T. Myo and K. Kat. Sum Rule Values with Respect to Unbound States in the Complex Scaling Method // Prog. Theor. Phys. 1997. – Vol. 98. – P.1275-1287.

[31] T. Myo, K. Kat , H. Toki, and K. Ikeda. Roles of tensor and pairing correlations on halo formation in 11Li // Phys.Rev.C. – 2007. – Vol. 76. – P. 024305.

[32] D. Tilleyet al. Energy levels of light nuclei A=8,9,10 // Nucl. Phys. A. – 2004. – Vol. 745. – P.155-362.

[33] W. Nörtershäuseret al. Nuclear Charge Radii of 7,9,10Be and the One-Neutron Halo Nucleus 11Be // Phys. Rev. Lett. – 2009. – Vol. 102. – P. 062503.

[34] I. I. Tanihataet al. Measurement of interaction cross sections using isotope beams of Be and B and isospin dependence of the nuclear radii // Phys. Lett. B. – 1988. – Vol. 206. – P. 592-596

UDC 539

R & D status of pulse shape analysis for short-lived decay of superheavy elements in GARIS-II

Yamaki S.[1*], Morimoto K.[1], Kaji D.[1], Wakabayashi Ya.[1], Takeyama M.[3], Tanaka K.[1,4], Tanaka T.[1], Baba H.[1], Yamaguchi T.[2], Suzuki T.[2], Morita K.[1]

[1]*Nishina Center for Accelerator Based Science, RIKEN, Saitama 351-0198, Japan*
[2]*Department of Physics, Saitama University, Saitama 338-8570, Japan*
[3]*Graduate School of Science and Engineering, Yamagata University, Yamagata, 990-8560, Japan*
[4]*Faculty of Science and Technology, Tokyo University of Science, Chiba 278-8510, Japan*
[5]*Department of Physics, Kyusyu University, Fukuoka 812-8581, Japan*
[*]*e-mail: sayaka.yamaki@riken.jp*

To search undiscovered superheavy elements, a series of commissioning experiments for the new gas-filled separator GARIS-II at RIKEN was recently carried out. A new data acquisition method was tested to study the short-lived α decay. Both the α decay and evaporation residues were detected by the silicon detectors, and the preamplified waveforms were then directly registered by a flash ADC and analyzed by means of a pulse shape analysis. This paper describes the identification of two sequential pulses (pileup events) from short-lived α decays and the determination of their energy and time difference by the template fitting method. The performance of the present system was evaluated by using a simulated data set and was successfully employed for online experimental data such as $^{220}\mathrm{Ac} \rightarrow {}^{216}\mathrm{Fr}$.

Key words: Superheavy elements, Pulse-shape analysis, α decays, short half-life
PACS numbers: 25.70.Ji, 23.60.+e, 29.85.Fj

1 Introduction

A project for synthesizing the 113th element by the cold-fusion reaction $^{209}\mathrm{Bi}(^{70}\mathrm{Zn}, \mathrm{n})^{278}113$ started at RIKEN in 2003. Three decay chains originating from $^{278}113$ were observed in 2004, 2005, and 2012 [1-3] . This project came to an end with the observation of the third decay chain. Our focus is now on the search for undiscovered heavier new elements such as Z = 119 and beyond. A series of commissioning experiments for the new gas-filled separator GARIS-II [4] designed for hot fusion reaction has almost been completed.

2 Data acquisition and analysis systems for the short lived decay

The half-lives of undiscovered isotopes are calculated by many theoretical approaches. As for $^{298}120$, typically if the Q_α value is around 13 MeV, the half-life will be on the order of microseconds [5, 6]. However, the measurement of the decay properties of such short-lived decays is difficult with the existing data acquisition system. The preampilfied waveforms have a long tail; therefore, in the case of a short-lived decay, two sequential pulses pile up. These piled-up pulses are shaped together in the shaping amplifier; thus, the information of an individual decay, such as the decay energy and time, will be lost. We overcome this problem by using a hybrid system utilizing analog and digital data acquisition systems; the former is the original system, whereas the latter is specialized for pileup events, where the time difference between two sequential events (ΔT) is less than 10 μ s. The waveforms from the preamplifiers of the silicon detectors are directly registered with flash ADCs to avoid the summing phenomenon. The readout system of GARIS-II is explained in [7].

Subsection 2.1 describes a method for analyzing the preamplifier waveforms to extract the decay information, and subsection 2.2 presents a performance evaluation of this system.

2.1 Pulse shape analysis

The left panel of Figure 1 shows preamplified piled-up pulses. Case (i) shows that both the first and second α particles are stopped in the double-sided silicon strip detector (DSSD). Case (ii) shows that the first α particle is stopped in the DSSD, and the second α particle escapes from DSSD; therefore, only part of the α energy is deposited in the DSSD, and vise-versa for case (iii). When the evaporation

residues are implanted and the subsequently decaying α particles are detected, the waveforms are also similar to case (ii). The decay properties are determined through a two-stage pulse shape analysis (PSA). The first stage is event identification to determine whether the detected pulses result from single events or pileup events, and the second stage is template fitting.

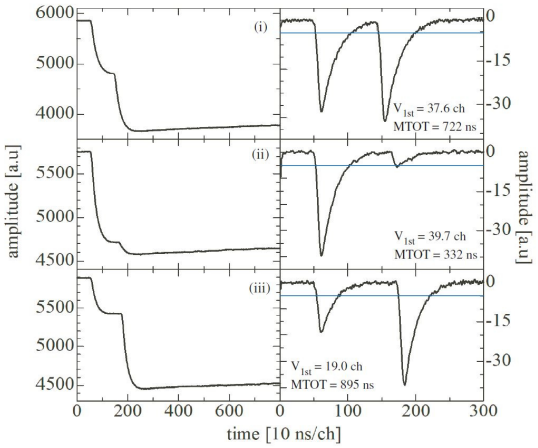

Figure 1 – Left: Original waveforms of pileup events. The sampling period is 8 μs (10 ns/ch).
Right: the solid lines indicate the derivatives of the waveforms shown on the left.
The blue line shows the threshold ($v_{th.}$) for calculating the mean of the time over threshold (MTOT).
The values of the first-pulse amplitude (V_{1st}) and MTOT are shown for each case

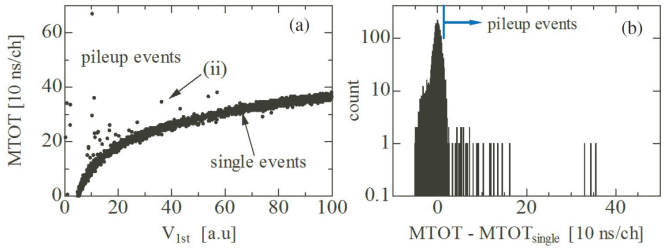

Figure 2 – (a) Relation between the MTOT and V_{1st}.
Single events are distributed around the logarithmic line. Pileup events are found above the line.
The data point for case (ii) in Figure 1 is indicated by an arrow. (b) Histogram of the distribution of $MTOT - MTOT_{single}$.
The threshold for discriminating single and pileup events is set at 14.2 ns

The graphs on the right side of Figure 1 show the derivatives of the waveforms shown in the graphs on the left side. The identification of single or pileup events is performed by calculating the mean of the time over threshold (MTOT) [8] of these waveforms. The MTOT is defined as

$$MTOT = \frac{\sum_{t=0}^{t_m} t w_t}{\sum_{t=0}^{t_m} w_t} - T, \; w_t = \begin{cases} 1 \; (v_t \le v_{th.}) \\ 0 \; (v_t > v_{th.}) \end{cases}, \qquad (1)$$

where t is the time (10 ns/ch), t_m is the sampling period, v_t is the amplitude, $v_{th.}$ is the amplitude threshold, and T is the minimum t when w_t =1. For pileup events, the MTOT depends on the ΔT and energy ratio (E_{1st} / E_{2nd}) between two pulses. The MTOT for each case is presented in Figure 1. In general, the MTOT is small when the ΔT is short or when the pulse height of second pulse is smaller than that of first pulse, as shown in case (ii).

The MTOT is compared with the pulse height of the first pulse (V_{1st}). The values of V_{1st} are also shown in Figure 1. Figure 2(a) shows the relation between the MTOT and V_{1st}. Single pulses are distributed along the logarithmic line

$$MTOT_{single} = a \cdot \log(V_{1st} - b), \qquad (2)$$

where a and b are derived for each stripped channel of the DSSD. Figure 2(b) shows a histogram of the difference of the MTOT from the logarithmic line, i.e., MTOT – $MTOT_{single}$. The Gaussian distribution denotes single events, and the tail on the right side denotes pileup events. The threshold for discriminating single and pileup events is set at 14.2 ns ($\sim 2\sigma$ of the single-event peak).

Both the single and pileup waveforms are fitted with the template function. The fitting formula is

$$f(t) = A[0] \cdot template(t - A[1]) + baseline, \qquad (3)$$

where the free parameters $A[0]$ and $A[1]$ are the pulse height and time offset, respectively. The left panel of Figure 3 shows a typical example of the template function, which is created by averaging many waveforms. The right panel of Figure 3 shows the reduced χ^2 distribution for the fitting of single pulses. The number of events for creating a template was varied among the values of 2, 5, 10, and 200, and the energy range was 5-6 MeV. Under the present conditions, only five events are sufficient for the creation of an accurate template function.

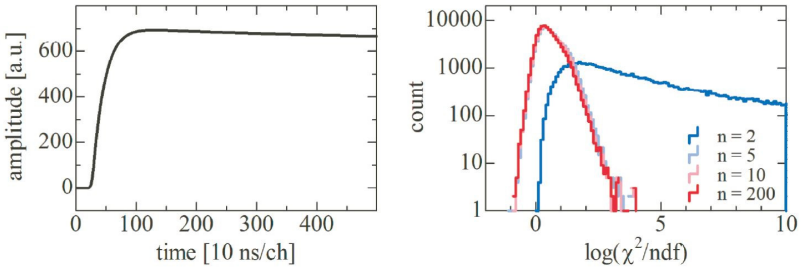

Figure 3 – The left panel shows the template function created by averaging many waveforms. The right panel shows the reduced χ^2 distribution for the fitting of single pulses.

Each pulse of a pileup event is fitted separately. Considering $E_{templ.}$ as the calibrated energy of the template, the energy of the fitted pulse is deduced by $A[0] \cdot E_{templ.}$. In addition, the decay time of the second event is determined as $A_{2hd}[1] - A_{1st}[1]$.

2.2Performance evaluation

To evaluate the performance of the PSA, a simulation study was performed. Pileup events were artificially created by summing two single pulses obtained in an online experiment. Pulses with energies of 1-20 MeV were selected. The ΔT were fixed at 50, 100, 200, 300, 400, 500, 600, and 700 ns.

Figure 4 shows the efficiency of pileup separation by the MTOT method. Here, the efficiency is defined as the ratio of the number of identified pileup events relative to the total number of events. The efficiency is almost 100% down to a ΔT of 300 ns for E_{1st} / E_{2nd} ranging from 0.06 to 16. Figure 5 shows the energy and time-difference accuracy of the template fitting. Events that have the correct energy ± 380 keV and correct ΔT ± 30 ns were considered to be successfully fitted. The results are again satisfactory unless the ΔT is small. Note that for both the efficiency and accuracy of the PSA, the performance deteriorates when the E_{1st} / E_{2nd} is large.

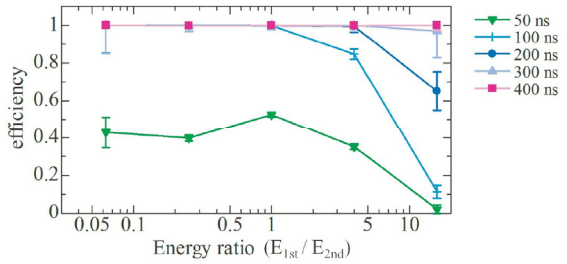

Figure 4 – The efficiency of pileup-event separation by the MTOT method. This is the efficiency for identifying every event as a pileup event and not as a single event

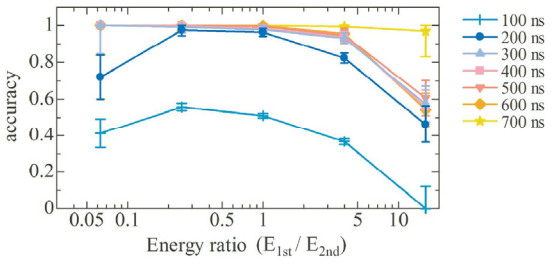

Figure 5 – The accuracy of the template-fitted waveforms. As criteria for successful fitting, an energy width of ± 380 keV and a ΔT width of ± 30 ns with respect to the true energy and ΔT, respectively, were used

The PSA was applied to online experimental data. Figure 6 shows some examples of ^{220}Ac $\rightarrow$^{216}Fr pileup events. The top graphs show the derivative waveforms, the middle graphs show the fittings of the first pulses (^{220}Ac), and the bottom graphs show the fittings of the second pulses (^{216}Fr). The values of the extracted α decay energies and decay times are also indicated in the figure. These pileup events were assigned by confirming the decay chain of ^{224}Pa $\rightarrow$^{220}Ac + ^{216}Fr $\rightarrow$ ^{212}At with the analog system. For these four events, the decay energies of the pileup events from ^{220}Ac and ^{216}Fr measured by the analog system are 16.8, 16.7, 16.7, and 16.8 ± 0.1 MeV from the left panel to right panel. The known values of the α decay energies for ^{220}Ac and ^{216}Fr are 7.86, 7.71, and 7.79 MeV ($I_\alpha \geq 10$) and 9.01 MeV, respectively, and the half-life for ^{216}Fr is 0.7 μs [9]. The cases shown in the three left-most panels are in good agreement with reference values. As the energy resolution depends on the ΔT of pileup events, the best resolution for $\Delta T < 200$ ns was 0.21 MeV (FWHM). In the right-most panel, the waveform could not be properly differentiated because of the slow rise time and noise. This situation also leads to the misidentification of the pulse type, i.e., single or pileup. Even if identification is successful, the energy and decay time are also likely to deviate from the correct values, as in this example. For better efficiency and accuracy, further improvements in the measurement conditions, such as a noise reduction or the tuning of the rise time of the preamplifier, are required.

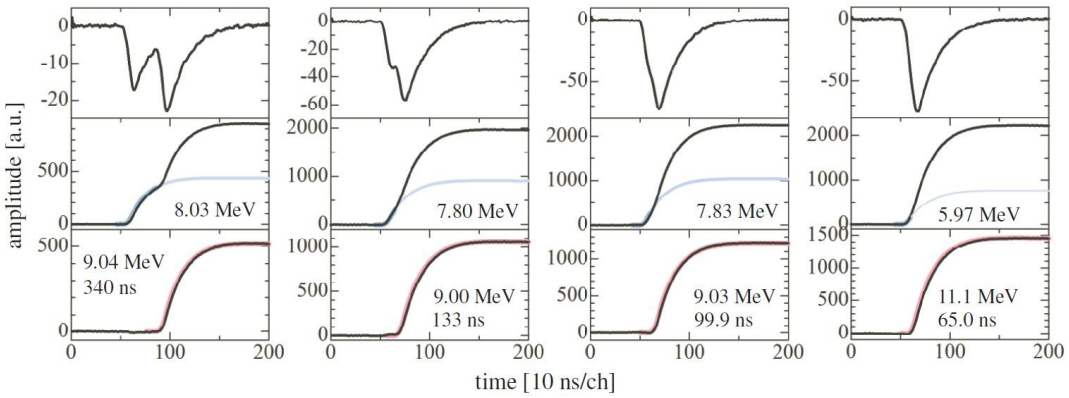

Figure 6 – Waveforms for the decay chain of ^{220}Ac $\rightarrow$^{216}Fr.
The top graphs show the derivative waveforms, the middle graphs show the fittings of the first pulse (^{220}Ac), and the bottom graphs show the fittings of the second pulse (^{216}Fr)

3 Summary

The PSA method enables the identification of pileup events and the individual deduction of the energy and ΔT of two sequential pulses. The efficiency of finding pileup events is almost 100% down to the ΔT of 300 ns in the E_{1st} / E_{2nd} range of 0.06-16. The identification efficiency and energy as well as the ΔT accuracy depend on the E_{1st} / E_{2nd} and attain the best values at ~ 1 . The derived energies for the short-lived α correlations in an online experiment show good agreement with the reference values. The present PSA aids in the accurate assignment of short-lived decay chains for future new-element searches.

Acknowledgements

The authors gratefully acknowledge everyone on the staffs of the RIBF and CNS for their contributions to the stable operation of the accelerator during this experiment. This work was supported by the RIKEN Junior Research Associate Program.

References

[1] K. Morita et al.. Experiment on the Synthesis of Element 113 in the ReactionBi(Zn.n) 113 // J. Phys. Soc. Jpn. – 2004. – Vol. 73. – P. 2593.

[2] K. Morita et al.. Observation of Second Decay Chain from113 // J. Phys. Soc. Jpn. – 2007. – Vol. 76. – P.045001.

[3] K. Morita et al.. New Result in the Production and Decay of an Isotope.113. of the 113th Element // J.Phys. Soc. Jpn. – 2012. – Vol. 81. – P. 103201.

[4] D. Kaji et al.. Gas–Filled Recoil Ion Separator GARIS–II // Nucl. Instr. Meth. B. – 2013. – Vol.. 317. – P.311.

[5] Yu. Ts. Oganessian et al.. Attempt to Produce Element 120 in the Reaction // Phys. Rev. C. – 2009. – Vol. 79. – P. 024603.

[6] A. Sobiczewski. Predictions for a Superheavy Element 120 // Acta. Phys. Pol. B. – 2011. – Vol. 42. No 8. – P. 1871.

[7] S. Yamaki et al. Pulse Shape Analysis Using Flash–ADC for Short–Lived Decay of Superheavy Elements // JPS Conf. Proc. – 2015. – Vol. 6. – P. 030105.

[8] S. Yamaki et al. Pulse Shape Analysis for Short–Lived Decay of Superheavy Elements // RIKEN Accel. Prog. Rep. – 2014. – Vol. 48. – P. 215.

[9] R. K. Sheline et al. Shell Model Level Structure of ^{216}Fr // Phys. Rev. C. – 1997. – Vol. 55. – P. 1162.

UDC 52.531

Theoretical and observational constrainhts on the mass-radius relations of neutron stars

Boshkayev K.[1*], Rueda J.A.[2], Muccino M.[2]

[1]*Al-Farabi Kazakh National University, IETP, Department of Physics and Technology, 71 al-Farabi av., 050040 Almaty, Kazakhstan*
[2]*International Center for Relativistic Astrophysics Network, Piazza della Repubblica 10, Pescara, I-65122, Italy*
[*]*e-mail: kuantay@mail.ru*

We investigate theoretical and observational constraints on the mass-radius relations for neutron stars. For that purpose we consider the model of neutron stars taking into considerations strong, weak, electromagnetic and gravitational interactions in the equation of state and integrate the structure equations within the Hartle-Thorne formalism for rotating configurations. On the basis of the theoretical restrictions imposed by general relativity, mass-shedding and axisymmetric secular instabilities we calculate the upper and lower bounds for the parameters of neutron stars. Our theoretical calculations have been compared and contrasted with the observational constraints and as a result we show that the observational constraints favor stiff equations of state.

Key words: neutron stars, equations of state, mass-radius relation, theoretical constraints, observational constraints.
PACS number(s): 97.60.Jd, 97.10.Nf, 97.10.Pg, 97.10.Kc, 26.60.Dd, 26.60.Gj, 26.60.Kp, 04.40.Dg

1 Introduction

Neutron stars are very compact and dense objects having average mass 1-2 $M_{\odot}$ (solar mass) and the average radius is around 10-15 km. The density in their center can exceed the nuclear density several times. They are an ideal laboratory which represents extreme conditions with high gravity, electromagnetic fields, density and pressure to test our theoretical models in nuclear and elementary particle physics [1]. Probably, neutron stars are one of the fewest objects, where all fundamental interactions: strong, weak, electromagnetic and gravitational, take place [1, 2, 3].

In this work, we consider the equilibrium structure of rotating neutron stars within the model proposed and recently extended by Belvedere et al. (2012, 2014) [4, 5] including the effects of rotation in terms of the Hartle-Thorne formalism [6, 7]. By fulfilling all the stability criteria and the latest observational and theoretical constraints on neutron star mass-radius relations, we computed the mass, radius, rotation frequency, angular momentum, quadrupole moment and other parameters of neutron stars.

Our paper is organized as follows: in Section 2, we consider the external Hartle-Thorne solution and the neutron star models; in Section 3, we discuss about the theoretical constraints on the mass-radius relations of neutron stars; in Section 4, we consider observational constraints. Finally, in Section 5, we summarize our main results, discuss their significance, and draw our conclusions.

2 The Hartle-Thorne metric and equation of state

In the physics of compact objects the Hartle-Thorne solutions both internal and external are applied to study the main characteristics and calculate the basic parameters of rotating configurations starting from white dwarfs to quark stars [2, 8]. It allows one, for a given equation of state (EoS), to construct the mass-central density, the mass-radius relations and other relations in a simple way. Although it is an approximate solution of the Einstein field equations with accuracy up to the second order terms in the angular velocity of the star, it can be safely used to investigate the physical structure and properties of the relativistic objects in the strong field regime with intermediate rotation rate [9, 10].

The Hartle-Thorne metric [7, 9] describing the exterior field of a slowly rotating slightly deformed object is given by

$$ds^2 = \left(1-\frac{2M}{r}\right)\left[1+2k_1P_2(\cos\theta)+2\left(1-\frac{2M}{r}\right)^{-1}\frac{J^2}{r^4}(2\cos^2\theta-1)\right]dt^2$$
$$-\left(1-\frac{2M}{r}\right)^{-1}\left[1-2\left(k_1-\frac{6J^2}{r^4}\right)P_2(\cos\theta)-2\left(1-\frac{2M}{r}\right)^{-1}\frac{J^2}{r^4}\right]dr^2$$
$$-r^2[1-2k_2P_2(\cos\theta)](d\theta^2+\sin^2\theta d\phi^2)+\frac{4J}{r}\sin^2\theta dt d\phi, \quad (1)$$

where

$$k_1 = \frac{J^2}{Mr^3}\left(1+\frac{M}{r}\right)+\frac{5}{8}\frac{Q-J^2/M}{M^3}Q_2^2(x),$$
$$k_2 = k_1+\frac{J^2}{r^4}+\frac{5}{4}\frac{Q-J^2/M}{M^2r}\left(1-\frac{2M}{r}\right)^{-1/2}Q_2^1(x),$$

and

$$Q_2^1(x) = (x^2-1)^{1/2}\left[\frac{3x}{2}\ln\frac{x+1}{x-1}-\frac{3x^2-2}{x^2-1}\right],$$
$$Q_2^2(x) = (x^2-1)\left[\frac{3}{2}\ln\frac{x+1}{x-1}-\frac{3x^3-5x}{(x^2-1)^2}\right], \quad (2)$$

are the associated Legendre functions of the second kind, with $x=r/M-1$, and $P_2(\cos\theta)=(1/2)(3\cos^2\theta-1)$ is the Legendre polynomial. The constants *M, J* and *Q* are the total mass, angular momentum and quadrupole moment of a rotating object, respectively.

The exterior Hartle-Thorne metric describes the gravitational field of any slowly and rigidly rotating, stationary and axially symmetric body. As one can see from Eq. 1 the exterior solution is given with accuracy up to the second order terms in the body's angular momentum, and first order in its quadrupole moment. Unlike other solutions of the Einstein field equations this solution possesses its internal counterpart. That is essential for the construction of the equilibrium configurations of rotating objects and calculate physical parameters inside and outside the sources of the gravitational fields.

There exist a number of models for neutron stars and correspondingly, the same number of equations of state. Depending on the nuclear compositions, theoretical assumptions and experimental data in nuclear physics the equations of state could be classified as soft, moderate and stiff. Different equations of state yield different mass-radius relations [11 - 15]. Hence there arises a natural question what EoS is more realistic? The only thing we know here is that the equation of state for neutron star must be constructed accounting for all fundamental interactions and the mass-radius relation must be in agreement with observational data. For this reason throughout this work we use the recent model of neutron stars formulated by Belvedere et al (2012) [4].

By employing both interior and the exterior Hartle-Thorne solutions with the equations of state given in Ref. [4] we obtained the mass-radius relations for static and rotating configurations in both local and global charge neutrality cases. As one can see in Fig. 1 rotating neutron stars will possess larger mass and larger radius with respect to the static case.

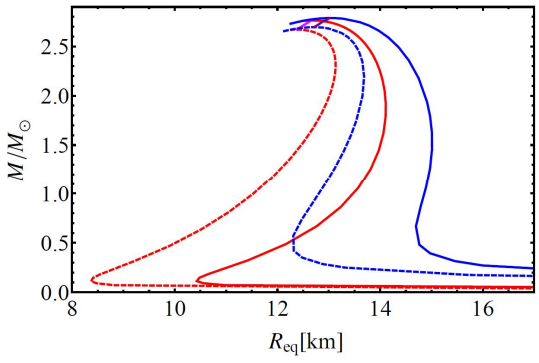

Figure 1 – Theoretical mass-radius relations presented in Belvedere et al. [5]. The red and blue curves represent the configuration with global and local charge neutralities, respectively. Here dashed and solid curves are static and Keplerian sequences, respectively. The magenta and the purple lines represent the secular axisymmetric stability boundaries for the globally neutral and the locally neutral cases, respectively

We also constructed the dependence of the quadrupole moment on the angular momentum in Fig. 2. Here we considered only global charge neutrality case, since for the local charge neutrality we have similar behavior. All possible values of Q and J for uniformly rotating neutron stars will be inside the loop. For vanishing angular velocity both Q and J will vanish simultaneously. By embedding in this diagram constant mass and constant frequency sequences one can infer either Q or J or both from observations.

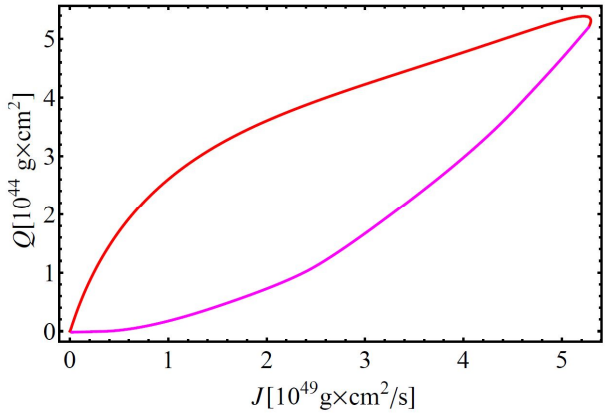

Figure 2 – The dependence of the quadrupole moment on the angular momentum of the rotating neutron star in the global charge neutrality cases. The red solid curve is the Keplerian sequences and the magenta curve is the secular axisymmetric stability boundary

While computing all these parameters we fulfilled stability criteria for rotating neutron star. Namely, the general relativistic instability related to the maximum mass, the mass-shedding limit (Keplerian limit) and the axisymmetric-secular instabilities have been taken into due account.

3 Theoretical constraints

In this section we discuss about theoretical constraints for neutron stars. First we consider the maximum mass. The maximum possible mass of neutron star was calculated by Rhoades and Ruffini (1974) [16]. They assumed that general relativity is the correct theory of gravity and the Tolman-Oppenheimer-Volkoff equation determines the equilibrium structure, the equation of state is known below a fiducial value of the nuclear density, and that causality is not violated in the neutron star interior, namely that the speed of sound is subluminal at any density in the interior. As a result they obtained maximum 3.2 $M_\odot$ for unknown equation of state. Since then a lot attempts have been made to calculate maximum mass for different realistic equations of state [16, 17, 18, 19, 20, 21, 22, 23, 24, 25, 26, 27]. As expected, for realistic neutron stars the maximum mass is always less than 3.2 $M_\odot$.

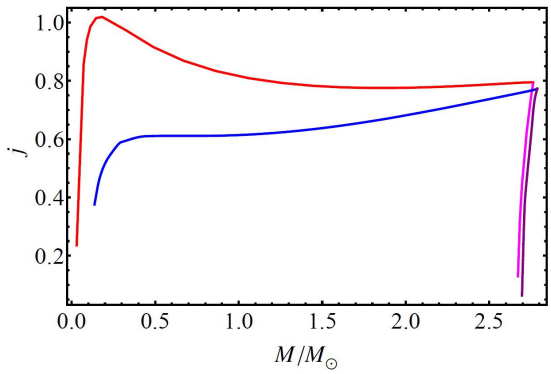

Figure 3 – Dimensionless angular momentum versus total mass. Red and blue solid curves are the Keplerian sequences, and magenta and purple curves are axisymmetric secular instability boundaries of both global and local neutrality cases, respectively

For rotating neutron star the dimensionless angular momentum j (spin parameter) can give an additional constraint. Relatively recently Lo & Lin [28] found that the maximum value of the dimensionless angular momentum j_{max} of a neutron star uniformly rotating at the Keplerian sequence has an upper bound of about 0.7, which is essentially independent on the mass of neutron star as long as the mass is larger than about $1M_\odot$. However, the same parameter of a quark star does not have such a universal upper bound and could be larger than unity.

The dimensionless angular momentum has been also calculated by Cipolletta et al. (2015) [29] for local charge neutrality cases with different equations of state and it has been also shown to be $j \approx 0.7$ independent of the equation of state.

Furthermore, Qi et al. [30] extended the analyses of Lo & Lin [28] and Cipolletta et al. [29] considering different kinds of uniformly rotating compact stars, including the traditional neutron stars, hyperonic neutron stars and hybrid stars. It was shown that the crust structure was a key factor to determine the properties of the spin parameter of the compact stars. When the crust EoSs are considered, $j_{max} \sim 0.7$ for $M > 0.5M_\odot$ is satisfied for three kinds of compact stars, no matter what the composition of the interior of the compact stars was.

When the crust EoSs are not included, the j_{max} of the compact stars can be larger than 0.7 but less

than about 1 for $M > 0.5M_{\odot}$. Consequently, according to Qi et al. [30] the crust structure provides the physical origin to the stability of j_{max} but not the interior of the compact stars. The strange quark stars with a bare quark-matter surface are the unique one to have $j_{max} > 1$. Thus, one can identify the strange quark stars based on the measured $j > 1.0$, while measured $j \in (0.7,1.0)$ could not be treated as a strong evidence of the existence of a strange quark star any more.

We also calculated the spin parameter using the model of neutron stars given by Belvedere et al. (2012). In Fig. 3 the spin parameter is shown as a function of the total mass. Clearly, the value of j is different from those of Lo & Lin [28] since we used different approach and different EoS. Despite this, the behavior of j is more similar to those ones of Qi et al. [30] as we have crusts in both local and global neutrality cases. However, for the global charge neutrality the thickness of the crust is thiner than for the local charge neutrality and that is the reason for the spin parameter to be different in these cases.

Table 1 – Maximum mass and corresponding radius, maximum frequency and minimum period of globally and locally neutral neutron stars.

Physicalparameters	Globalneutrality	Localneutrality
$M_{max}^{J=0} / M_{\odot}$	2.67	2.70
$R_{max}^{J=0}$ (km)	12.38	12.71
$M_{max}^{J\neq 0} / M_{\odot}$	2.76	2.79
$R_{max}^{J\neq 0}$ (km)	12.66	13.06
f_{max} (kHz)	1.97	1.89
P_{min} (ms)	0.51	0.53

In Table 1 we show upper bounds for static and rotating neutron stars within the model proposed by Belvedere et al (2012). Here we have stiff equation of state and correspondingly the maximum mass is larger than 2.6 $M_{\odot}$ and smaller than 3.2 $M_{\odot}$.

4 Observational constraints

According to observations, the most recent and stringent constraints to the mass-radius relation of neutron stars are provided from data for pulsars by the values of the largest mass, the largest radius, the highest rotational frequency, and the maximum surface gravity [31].

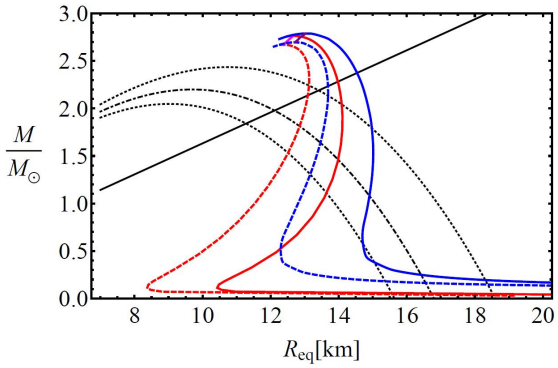

Figure 4 – Observational constraints on the mass-radius relation given by Trümper [31] and the theoretical mass-radius relation presented in Fig 1. The solid black curve is the observed upper limit of the surface gravity, the dotted-dashed black curve corresponds to the lower limit to the observed radius, and the dotted curves are the 90% confidence level contours of constant R_{∞}

Up to now the largest neutron star mass measured with a high precision is the mass of the 39.12 millisecond pulsar PSR J0348+0432, $M = 2.01 \pm 0.04 M_{\odot}$ [32]. The largest radius is given by the lower limit to the radius of RX J1856-3754, as seen by an observer at infinity $R_{\infty} = R[1 - 2GM/(c^2 R)]^{-1/2} > 16.8$ km [33]; it gives the constraint $2GM/c^2 > R - R^3/(R_{\infty}^{min})^2$, where $R_{\infty}^{min} = 16.8$ km. The maximum surface gravity is obtained by assuming a neutron star of $M = 1.4M_{\odot}$ to fit the Chandra data of the low-mass X-ray binary X7, it turns out that the radius of the star satisfies $R = 14.5^{+1.8}_{-1.6}$ km, at 90 % confidence level, corresponding to $R_{\infty} = [15.64, 18.86]$ km, respectively [34]. The maximum rotation rate of a neutron star has been found to be $\nu_{max} = 1045(M/M_{\odot})^{1/2}(10\text{km}/R)^{3/2}$ Hz [12]. The fastest observed pulsar is PSR J1748-2246ad with a rotation frequency of 716 Hz [35], which results in the constraint $M \geq 0.47(R/10\text{km})^3 M_{\odot}$.

From a technical or practical standpoint, in order to include the above observational constraints in the mass-radius diagram it is convenient to rewrite them for a given range of the radius (for instance, 6 km ≤ R ≤ 22 km) as follows:

1. The maximum mass:

$$\frac{M}{M_{\odot}} = 2.01. \qquad (3)$$

2. The maximum surface gravity:

$$\frac{M}{M_\odot} < 2.4\times10^5 \frac{c^2}{G}\frac{R}{M_\odot}. \quad (4)$$

3. The lower limit for the radius surface gravity:

$$\frac{M}{M_\odot} = \frac{10^5}{2}\frac{c^2}{G}\frac{R}{M_\odot}\left(1-\frac{R^2}{(R_\infty^{min})^2}\right). \quad (5)$$

4. The maximum rotation rate:

$$\frac{M}{M_\odot} > \frac{0.47}{10^3}R^3. \quad (6)$$

Note, that the last formula is valid only for the static mass-radius relations, since R is the static radius. In order to include this constraint in the rotating mass-radius relation one should construct a constant frequency sequence for the fastest spinning pulsar with 716 Hz. For the sake of generality, we can just require that equilibrium models are bound by the Keplerian sequence (see Refs. [5, 29] for details). In all expressions above (3-6) the mass is normalized with respect to the solar mass $M_\odot$ and the radius is expressed in km.

In Fig. 4 we superposed the observational constraints introduced by Trümper [31] with the theoretical mass-radius relations presented here and in Belvedere et al. [4, 5] for static and uniformly rotating neutron stars. Any realistic mass-radius relation should pass through the area delimited by the solid black, the dotted-dashed black, the dotted curves and the Keplerian sequences. From here one can clearly see that the above observational constraints show a preference on stiff EoS that provide largest maximum masses for neutron stars. From the above constraints one can infer that the radius of a canonical neutron star of mass $M = 1.4M_\odot$ is strongly constrained to $R \geq 12$ km, disfavoring at the same time strange quark matter stars. It is evident from Fig. 4 that mass-radius relations for both the static and the rotating case presented here, are consistent with all the observational constraints.

5 Conclusion

In this work we have considered the local and global neutrality cases in the model of neutron stars formulated by Belvedere et al. (2012). We also constructed the mass-radius diagram for rotating neutron stars on the basis of the work of Belvedere et al. (2014) within the Hartle-Thorne formalism. In addition, we calculated the maximum rotating mass, corresponding radius, minimum rotation period, dimensionless angular momentum, quadrupole moment and other crucial parameters of rotating neutron stars.

Furthermore, we considered theoretical constraints in the literature imposed on the mass-radius relations. Namely, we discussed about the maximum possible mass and maximum masses depending of the model of neutron stars, minimum periods, maximum dimensionless angular momentum, the relation between angular momentum and quadrupole moment etc. All these parameters are model dependent. Equations of state based on different models give different maximum and minimum values for all parameters.

In order to favor or disfavor some models we considered observational constraints on the mass-radius relations of neutron stars related to the maximum observed mass, maximum surface gravity, largest mass, maximum rotation frequency. All these constraints are important not only in the physics of neutron stars, but also in nuclear physics to test theoretical hypothesis and assumptions made in the construction of the equations of state. As a result all observations favor stiff equations of state as indicated by Yakovlev (2016) [36].

The results of this work can be applied to the investigation of the X-ray phenomena occurring in the accretion disks around neutron stars such as quasi periodic oscillations [37]. Combining both the quasi periodic oscillations data from low X-ray binary systems and physics of compact objects one can extract information not only on the properties of the accretion disks, but also infer the parameters of neutron stars and constrain the equations of state [38, 39, 40, 41, 42, 43, 44].

Finally, the correct determination of neutron star critical mass, including its crust, plays also a very important role in understanding the progenitors of long gamma-ray burst (GRB), proposed to originate in binary systems composed of an evolved star exploding as a Ib/c supernova and triggering a hypercritical accretion process onto a companion neutron star [46], and short GRBs, originating from binary neutron star mergers. In both cases two outcomes are possible depending on whether or not the accretion process or the merger can push the neutron star or the merged core, respectively, beyond the critical mass [47, 45].

Acknowledgements

This work was supported by program No F.0679 of grant No 0073 and the grant for the university best teachers-2015 of the Ministry of Education and Science of the Republic of Kazakhstan. K.B. acknowledges ICRANet for hospitality.

References

[1] S.L. Shapiro. S.A. Teukolsky. Black holes. white dwarfs. and neutron stars: The physics of compact objects // Wiley–VCH. – 1983. – P. 672.

[2] P. Haensel. A.Y. Potekhin. D.G. Yakovlev. Neutron Stars 1: Equation of State and Structure // New York: Springer. – 2007. – P. 620.

[3] A.Y. Potekhin. – Usp. Fiz. Nauk180. 1279–1304 (2010) [in Russian]. The physics of neutron stars // English translation: Physics–Uspekhi. – 2010. – Vol. 53. – P. 1235.

[4] R. Belvedere. D. Pugliese. J.A. Rueda. R. Ruffini. S.–S. XueNeutron star equilibrium configurations within a fully relativistic theory with strong, weak, electromagnetic, and gravitational interactions // Nuclear Physics A. – 2012. – Vol. 883. – P. 1–24.

[5] R. Belvedere. K. Boshkayev. J.A. Rueda. R. Ruffini.Uniformly rotating neutron stars in the global and local charge neutrality cases // – Nuclear Physics A. – 2014. – Vol. 921. – P. 33.

[6] J.B. Hartle.Slowly Rotating Relativistic Stars. I. Equations of Structure // Astrophysical Journal. – 1967. – Vol. 150. – P. 1005.

[7] J.B. Hartle. K.S. Thorne. Slowly Rotating Relativistic Stars. II. Models for Neutron Stars and Supermassive Stars // Astrophysical Journal. – 1968. – Vol. 153. – P. 807.

[8] K. Boshkayev. J A. Rueda. R. Ruffini. I. Siutsou. On General Relativistic Uniformly Rotating White Dwarfs // The Astrophysical Journal. – 2013. – Vol. 762. – P. 117.

[9] K. Boshkayev. R. Ruffini. H. Quevedo. Gravitational field of compact objects in general relativity // Phys. Rev. D. – 2012. – Vol. 86. – P. 064043.

[10] E. Berti. F. White. A. Maniopoulou. M. Bruni. Rotating neutron stars: an invariant comparison of approximate and numerical space–time models // Monthly Notices of the Royal Astronomical Society. – 2005. – Vol. 358. – P. 923–938.

[11] J.M. Lattimer. M. Prakash.Neutron Star Structure and the Equation of State // The Astrophysical Journal. – 2001. – Vol. 550. – P. 426–442.

[12] J.M. Lattimer. M. Prakash. The Physics of Neutron Stars // Science. – 2004. – Vol. 304. – P. 536.

[13] J.M.Lattimer. M. Prakash. Neutron star observations: Prognosis for equation of state constraints // Physics Reports – 2007. – Vol. 442. – P. 109.

[14] J.M. Lattimer. M. Prakash What a Two Solar Mass Neutron Star Really Means // International Journal of Modern Physics B. – 2010. arXiv:1012.3208v1

[15] J.M. Lattimer. M. Prakash.The equation of state of hot, dense matter and neutron stars // Physics Reports – 2016. – Vol. 621. – P. 127.

[16] C.E. Rhoades. R. Ruffini. P International Journal of Modern Physics B // Phys. Rev. Lett. – 1974. – Vol. 32. – P. 324.

[17] H.A. Bethe. G.E Brown. Observational constraints on the maximum neutron star mass // The Astrophysical Journal. – 1995. – Vol. 445 – P. 129.

[18] V. Kalogera. G. Baym.The Maximum Mass of a Neutron Star // The Astrophysical Journal. – 1996. – Vol.470. – P. 61.

[19] H. Heiselberg. M. Hjorth–Jensen.Phase Transitions in Neutron Stars and MaximumMasses // The Astrophysical Journal. – 1999. – Vol.525. – P. L45.

[20] H.–J. Schulze. A. Polls. A. Ramos. I. Vidana. Maximum mass of neutron stars // Physical Review C. – 2006. – Vol. 73. – P. 058801.

[21] S. Gandolfi. J. Carlson. S. Reddy.Maximum mass and radius of neutron stars, and the nuclear symmetry energy // Physical Review C. – 2012. – Vol.85. – P. 032801.

[22] N. Chamel. P. Haensel. J.L. Zdunik. A.F. Fatina. Onthemaximummass ofneutron // International Journal of Modern Physics E. – 2013. – Vol. 22. – P. 1330018.

[23] A. Bauswein.T. W. Baumgarte. and H.–T. Janka. Prompt Merger Collapse and the Maximum Mass of Neutron Stars// Physical Review Letters. – 2013. – Vol.111. – P. 131101.

[24] N.B. Zhang. B. Qi. S. Y. Wang. S.L. Ge. Keplerian frequency of uniformly rotating neutron stars in relativistic mean field theory // International Journal of Modern Physics E. – 2013. – Vol. 22.– P. 1350085.

[25] G. Martinon. A. Maselli. L. Gualtieri. V.Ferrari. Rotating protoneutron stars: Spin evolution, maximum mass, and I-Love-Q relations // Physical Review D. – 2014. – Vol. 90.– P. 064026.

[26] C. Breu. L. Rezzolla.Maximum mass, moment of inertia and compactness of relativistic stars // MNRAS – 2016. – Vol. 459. – P. 646.

[27] K.A. Maslov. E.E. Kolomeitsev. D.N. Voskresensky. Relativistic mean-field models with scaled hadron masses and couplings: Hyperons and maximum neutron star mass // Nuclear Physics A. – 2016. – Vol. 950. – P. 64.

[28] Ka-Wai Lo. Lap-Ming Lin. The spin parameter of uniformly rotating compact stars // The Astrophysical Journal. – 2011. – Vol. 728. – P. 12.

[29] F. Cipolletta. C. Cherubini. S. Filippi. J.A.Rueda. R. Ruffini. Fast rotating neutron stars with realistic nuclear matter equation of state // Physical Review D. – 2015. – Vol. 92. – P. 023007.

[30] B. Qi. N.B. Zhang. B.Y. Sun. S.Y. Wang. J.H.Gao. A key factor to the spin parameter of uniformly rotating compact stars: crust structure // Research in Astronomy and Astrophysics. – 2014. – Vol. 16. – P. 008.

[31] J.E. Trümper. Observations of neutron stars and the equation of state of matter at high densities // Prog. Part. Nucl. Phys. – 2011.– Vol. 66. – P. 674.

[32] J. Antoniadis et. al.A Massive Pulsar in a Compact Relativistic Binary // High Energy Astrophysical Phenomena. – 2013. – Vol. 340. – P. 448.

[33] J. Trümper. V. Burwitz. F. Harberl. V.E.Zavlin. The puzzles of RX J1856.5-3754: neutron star or quark star? // Nucl. Phys. B Proc. Suppl. – 2004. – Vol. 132. – P. 560.

[34] C.O. Heinke. G.B. Rybicki. R. Narayan. J.E. Grindlay. A Hydrogen Atmosphere Spectral Model Applied to the Neutron Star X7 in the Globular Cluster 47 Tucanae// Astroph. J. – 2006. – Vol. 644. – P. 1090.

[35] J.W.T. Hessels. S.M. Ransom. I.H. Stairs. P.C.C. Freire. V.M. Kaspi. F. Camilo.A radio pulsar spinning at 716 Hz // Science. – 2006. – Vol. 311. – P.1901.

[36] D.G. Yakovlev. General relativity and neutron stars // International Journal of Modern Physics A. – 2016. – Vol. 31. – P. 1641017.

[37] L.A. Pachon. J.A. Rueda. C.A. Valenzuela – Toledo. On the relativistic precession and oscillation frequencies of test particles around rapidly rotating compact stars // The Astrophysical Journal. – 2012. – Vol. 756. – P. 82.

[38] K. Boshkayev. D. Bini. J. Rueda. A. Geralico. M. Muccino. I. Siutsou.What can we extract fromquasiperiodic oscillations? // Gravitation and Cosmology. – 2014. – Vol. 20. – P. 233.

[39] K. Boshkayev. J. Rueda. M. Muccino. Extracting multipole moments of neutron stars from quasi-periodic oscillations in low mass X-ray binaries // Astronomy Reports. – 2015. – Vol. 59. – P. 441.

[40] G. Pappas. Unified description of astrophysical properties of neutron stars independent of the equation of state // Monthly Notices of the Royal Astronomical Society. – 2015. – Vol. 454.– P. 4066–4084.

[41] Z. Stuchlik. M. Urbanec. A. Kotrlova. G.Torok. K. Goluchova. Equations of state in the Hartle-Thorne model of neutron stars selecting acceptable variants of the resonant switch model of twin HF QPOs in the atoll source 4U 1636-53 // Acta Astronomica. – 2015. – Vol. 65. – P. 169.

[42] Z. Stuchlik. M. Kolos.Models of quasi-periodic oscillations related to mass and spin of the GRO J1655-40 black hole // Astronomy & Astrophysics. – 2016. – Vol. 586. – P. A130.

[43] K. Boshkayev. J. Rueda. M. Muccino. // – eprint arXiv. –1604.02398.

[44] S. Chen. M. Wang. J. Jing. // – eprint arXiv. –1604.07106.

[45] R. Ruffini. M. Muccino. M. Kovacevic. F.G.Oliveira. J.A. Rueda. C.L. Bianco. M. Enderli. A.V.Penacchioni. G.B. Pisani.Y. Wang. E. Zaninoni. GRB 140619b: a short grb from a binary neutron star merger leading to black hole formation // The Astrophysical Journal. – 2015. – Vol. 808. – P. 190.

[46] C.L. Fryer. J. A. Rueda. R. Ruffini. Hypercritical accretion, induced gravitational collapse, and binary-driven hypernovae // The Astrophysical JournalLetters. – 2014. – Vol. 793. – P. 36.

[47] R. Ruffini. Y. Wang. M. Enderli. M. Muccino. M. Kovacevic. C.L. Bianco. A.V. Penacchioni. G.P.Pisani. J.A. Rueda. GRB 130427a and sn 2013cq: a multi-wavelength analysis of an induced gravitational collapse event // The Astrophysical Journal – 2015. – Vol. 798. – P. 10.

UDC 539.1

Microscopic description of ^8Li and ^8B nuclei within three-cluster model

Vasilevsky V.S.[1*], Takibayev N.Zh.[2], Duisenbay A.D.[2]

[1]*Bogolyubov Institute for Theoretical Physics, 14-B, Metrolohichna str., Kiev, 03680, Ukraine*

[2]*Department of Physics and Technology, al-Farabi Kazakh National University, 71 al-Farabi av., 050040 Almaty, Kazakhstan*

e-mail: vsvasilevsky@gmail.com

We make theoretical analysis of bound and resonance states of ^8Li and ^8B nuclei. The analysis is carried out within a three-cluster microscopic model which account for polarizability of interacting clusters. Main attention is paid to the nature of resonances states embedded in two-cluster continuum. We also study effects of the cluster polarization on the spectrum of bound and resonance states, and on the elastic and inelastic $n + {}^7Li$ and $p + {}^7Be$ scattering.

Key words: Cluster model, polarization, resonance state.
PACS number(s): 24.10.-i, 21.60.Gx

1 Introduction

Analysis of the astrophysical data on the abundance of light atomic nuclei in the Universe stimulated new and more detail experimental and theoretical investigations of reactions induced by interaction of light nuclei. For the astrophysical applications one has to know the cross section of a reaction at the low energy region, which amounts several kiloelectron volts in the entrance channel of the reaction. This region of energy can be easily achieved at experimental facilities for the reactions induced by interaction of neutrons with light nuclei. However, it is not the case for interaction of light nuclei, containing one or more protons. Coulomb interaction between nuclei makes very difficult to measure the cross section. In this case theoretical methods are invaluable tool to determine or to evaluate the cross section of importance.

As many of light nuclei are weakly bound, they could easy change their size or shape while interacting with neutrons, protons or other light nuclei. This phenomenon is called the polarization. A microscopic three-cluster model was formulated in Ref. [1] to take into account polarizability of the interacting clusters. We refer to it as "cluster polarization". It was shown in Refs [1 – 4] that cluster polarization plays an important role in formation of bound and resonance states in seven nucleon systems. It was also shown that cluster polarization has large impact on different types of reactions in ^7Li and ^7Be nuclei. Within the present paper, the effects of cluster polarization will be studied in light mirror nuclei ^8Li and ^8B, and interaction of neutron with ^7Li and proton with ^7Be. Both ^7Li and ^7Be nuclei have well established two-cluster structure: $^4He + {}^3H$ and $^4He + {}^3He$, respectively. This fact is taken into account in the present model. We are also going to consider bound and resonance states of the mirror nuclei ^8Li and ^8B within three-cluster microscopic model. We study resonance states created by two-cluster and three-cluster configurations.

Properties of mirror nuclei ^8Li and ^8B have been intensively investigated in microscopic and semimicroscopic models. Besides different experimental methods were used to determine structure of ^8Li and ^8B and nuclear reactions in these nuclei. In particular, new resonance states of ^8B have been recently discovered in [5, 6] in elastic $^7Be + p$ scattering.

The novelty of our approach is that it allows us to consider cluster polarizations. It means that within the proposed model, size and shape of clusters are not fixed but depend on distance between interacting clusters. In the present case we consider how size of ^7Li (^7Be) is changed when neutron (proton) moves toward ^7Li(^7Be).

2 Method and model space

We shall consider ^8Li as a three-cluster configuration $^8Li = \alpha + t + n$ and nucleus ^8B we shall represent as the configuration $^8B = \alpha + {}^7He + p$. These configurations are dynamically distinguished from other three-cluster configurations as they have minimal threshold energy compared to other three-cluster configurations in ^8Li and ^8B. By using

such three-cluster configurations we can take into account the following set of two-cluster channels: $^7Li + n$, $^5He + ^3He$, $^4He + ^4He$ in ^8Li and $^7Be + p$, $^5Li + ^3He$, $^4Li + ^4He$ in ^8B. Moreover, with such three-cluster configurations, we can consider nuclei ^7Li, ^5He, ^4H, ^7Be, ^5Li, ^4Li as two-cluster systems: $^7Li = \alpha + t$, $^5He = \alpha + n$, $^4He = t + n$, $^7Be = \alpha + ^3He$, $^5Li = \alpha + p$, $^4Li = ^3He + p$ and provide more advanced description of internal structure of these nuclei.

To describe selected three-cluster configurations we employ Algebraic Model with Gaussian and Oscillator Basis (AMGOB) [1 – 4]. We start with construction of wave functions for two-cluster subsystems and for compound three-cluster system. Two-cluster wave function $\Psi^{(\alpha)}_{J_\alpha}$, describing interaction of clusters with indexes β and γ, can be written as

$$\Psi^{(\alpha)}_{E_\alpha J_\alpha} = \widehat{\mathcal{A}_{\beta\gamma}} \left\{ \left[\Phi_\beta\left(A_\beta, s_\beta\right) \Phi_\gamma\left(A_\gamma, s_\gamma\right) \right]_{S_\alpha} g^{(E)}_{\lambda_\alpha J_\alpha}\left(x_\alpha\right) Y_{\lambda_\alpha}\left(\hat{\mathbf{x}}_\alpha\right) \right\}_{J_\alpha} \tag{1}$$

Indexes α, β and γ form cyclic permutations of 1, 2 and 3.

Wave function of discrete and continuous spectrum states of three-cluster system is

$$\Psi_{E,J} = \sum_{\alpha=1}^{3} \widehat{\mathcal{A}} \left\{ \left[\Phi_1\left(A_1, s_1\right) \Phi_2\left(A_2, s_2\right) \Phi_3\left(A_3, s_3\right) \right]_S \times f^{(E,J)}_{\lambda_\alpha l_\alpha, L}\left(x_\alpha, y_\alpha\right) \left\{ Y_{\lambda_\alpha}\left(\hat{\mathbf{x}}_\alpha\right) Y_{l_\alpha}\left(\hat{\mathbf{y}}_\alpha\right) \right\}_L \right\}_J \tag{2}$$

where $\Phi_\alpha(A_\alpha, s_\alpha)$ is a many-particle shell-model wave function describing the internal motion of cluster α (α = 1, 2, 3), consisted of A_α nucleons ($1 \le A_\alpha \le 4$), and s_α denotes spin of the cluster.

Similarly to the case of three particles, we use three Faddeev amplitudes $f^{(E,J)}_{\lambda_\alpha l_\alpha, L}\left(x_\alpha, y_\alpha\right)$ and three sets of the Jacobi coordinates $\mathbf{x}_\alpha$ and $\mathbf{y}_\alpha$. The Jacobi coordinates determine relative position of the center of mass of three clusters. In our notations, $\mathbf{x}_\alpha$ is the Jacobi vector, proportional to the distance between β and γ clusters, while $\mathbf{y}_\alpha$ is a Jacobi vector connecting the α cluster to the center of mass of the β and γ clusters. Vectors $\hat{x}_\alpha$ and $\hat{y}_\alpha$ denotes unit vectors $\hat{x}_\alpha = x_\alpha / |x_\alpha|$ and $\hat{y}_\alpha = y_\alpha / |y_\alpha|$. Antisymmetrization operators $\widehat{A}_{\beta\gamma}$ and $\widehat{A}$ make antisymmetric wave functions of two- and three-cluster systems, respectively. Note that shell-model wave functions $\Phi_\alpha\left(A_\alpha, s_\beta\right)$ are antisymmetric, thus operator $\widehat{A}_{\beta\gamma}$ and $\widehat{\mathcal{A}}$ permute nucleons from different clusters.

Note that the shell-model wave function $\Phi_\alpha(A_\alpha, s_\beta)$ explicitly depends on oscillator length b. In different realizations of the many-cluster model this parameter is used as a variational or adjustable parameter. As a rule oscillator length is adjusted to minimize bound state energy of clusters or to reproduce their size (i.e. mass or proton root-mean-square (rms) radius). Within all our models we use common oscillator length for all clusters involved in calculations.

The Faddeev amplitudes $f^{(E,J)}_{\lambda_\alpha l_\alpha, L}\left(x_\alpha, y_\alpha\right)$ in eq. (2) is marked by two partial orbital momenta λ_α and l_α. They are associated with the Jacobi vectors $\mathbf{x}_\alpha$ and $\mathbf{y}_\alpha$, respectively. In what follows we assumethat λ_α is the orbital momentum of two-cluster subsystem and l_α is the orbital momentum connected with rotation of a third cluster around center of mass of two-cluster subsystem.

To solve correctly the three-cluster problems, we need to solve two-cluster Schrödinger equation for three different two-cluster partitions α (α = 1, 2, 3). Energy of two-cluster bound states determine the threshold energy of two-body channels and wave functions determine an asymptotic form of three-body functions in the part of coordinate space which Faddeev and Merkuriev denoted as Ω_α (see pages 134-135 of book [7]), i.e. in the region where distance $\mathbf{x}_\alpha$ between selected pairs of clusters is much smaller that distance between other pairs of clusters ($x_\alpha \ll x_\beta$, $x_\alpha \ll x_\gamma$). Having solved the Schrödinger equationsfor all two-cluster subsystems, we can proceed with solving the Schrödinger equation for three-cluster system (see eq. (31) and (33) in Ref. [1]). It is well know [8] that the Schrödinger equations for two- and three-cluster systems can be reduced to two- and three-body equations, respectively, with nonlocal and energy-dependent potentials. The later needs special attention and has to taken into account. The most simple way of overcoming this problem is to use a square-integrable basis.

The essence of the model, employed in the present investigations, is to use a discretization scheme with the help of square-integrable basis. It allows us to reduce the Schrödinger equation for many-channel system to the set of algebraic equations, which can be easily solved numerically. In present model we use of the Gaussian basis to describe bound and pseudo-bound states of two-cluster subsystems, and we employ the Oscillator basis to study interaction of the third cluster with two-cluster subsystem. The explicit definition of the Gauss and oscillator basis functions, deducing of set of linear equations for wave function and boundary conditions for wave function are presented in Refs. [1, 2].

3 Results

We use two nucleon-nucleon potentials: the Minnesota potential (central components are taken from [9, 10]) and the Modified Hasegawa-Nagata potential (MHNP) [11, 12].Oscillator length b, which is common for all clusters, is adopted to minimize the threshold energy of the three-cluster channel. In this way we optimize description of the internal structure of all clusters. For ^8Li (^8B) and the MP it equals b =1.451 fm and for MHNPit equals b = 1.362 fm. In present calculations, we use the Majorana parameter m of the MHNP [11, 12] and parameter u of the MP [9] as adjustable parameters. These parameters are slightly changed to reproduce the bound state energy of ^8B.This is done in order to be consistent with the experimental situation in ^8Li and ^8B nuclei. In Table 1 we show spectrum of the ^8Li and ^8B bound states, which is obtained with "optimal" input parameters. Experimental data are from Ref. [13]. Energy of bound states in ^8Li and ^8B is reckoned from the two-cluster threshold $^7Li + n$ and $^8Be + n$, respectively. One can see that the MHNP provides more correct description of the bound state spectrum in ^8Li. Meanwhile, the optimal input parameters of the MP leads to too very close position of the ground 2^+ state and the first excited 1^+ state.

Table 1 – Optimal input parameters and spectrum of bound states in ^8Li and ^8B. Energy of the bound states is determined from the $^7Li + n$ and $^8Be + p$ thresholds in ^8Li and ^8B, respectively

Nucleus	^8Li			^8B		
Potential	MP	MHNP	Exp.	MP	MHNP	Exp.
b, fm	1.3451	1.3620		1.3451	1.3620	
m (u)	0.9600	0.4157		0.9600	0.4157	
J^π	E, MeV	E, MeV	E, MeV	E, MeV	E, MeV	E, MeV
2^+	-1.958	-1.908	-2.032	-0.1368	-0.1393	-0.1375
1^+	-1.607	-0.977	-1.051			

To achieve convergence of energy of the ^8Li and ^8B bound states as a function of number of the Gaussian and oscillator functions, we investigated in detail how energy of bound and resonance states depends on number of basis functions. We found that 4 Gaussian functions and 50 oscillator functions provide an acceptable precision of microscopic calculations of energy and other parameters of the bounds states, such as, for instance, the root-mean-square proton, neutron and mass radii. It is also established that, 4 Gaussian functions and 130 oscillator functions guarantee a necessary precision of the scattering matrix and energy and width of resonance states calculations.

In Table 2 we display the proton, neutron and mass rms radii of the ground state in ^8Li and ^8B nuclei. Experimental data are taken from Ref. [14]. Theoretical results are in a good agreement with the experimental data. One can see that our results confirm the existence of the neutron halo in ^8Li and the proton halo in ^8B, as neutron (proton) rms radius is larger than the proton (neutron) rms radius in ^8Li (^8B).This is confirmed by the last column of the Table, where the difference between proton and neutron rms radii is displayed. Our results are also in a good agreement with the results, obtained in similar microscopic models [15], [16].

Table 2 – Proton (R_p), neutron (R_n) and mass (R_m) rms radii (in fm) of the ground state in ^8Li and ^8B. Energy of the ground state is in MeV

	NNP	E	R_p	R_n	R_m	$\lvert R_p - R_n \rvert$
^8Li	MP	-2.001	2.174	2.516	2.394	0.342
	MHNP	-1.908	2.174	2.548	2.415	0.374
	Exp.		2.266(0.02)	2.446(0.02)	2.376(0.02)	
^8B	MP	-0.137	2.724	2.217	2.546	0.507
	MHNP	-0.139	2.756	2.244	2.576	0.512
	Exp.		2.496(0.03)	2.336(0.03)	2.436(0.03)	

Let us now tern our attention to the resonance states. Resonance states in ^8Li and ^8B, generated by interaction of neutron with ^7Li and proton with ^8Be respectively, are demonstrated in Table 3. Experimental parameters of resonance states are taken from Ref. [13]. As one can see energy and width of resonance states strongly depends on shape of resonance states. For instance, energy of the first 3^+ resonance state in ^8Li obtained with the MHNP potential is 12 times larger than the one calculated with the MP, and width is almost 50 times large than the width calculated with the MP. There is one exception, when parameters of resonance state, calculated with both potentials are very close to each other. This is the 3^+ resonance state in ^8B. In this case energy and width of the resonance state do not differ so dramatically as for other resonance states.

Table 3 – Spectrum of resonance states in ^8Li and ^8B. Energy of resonances is given in MeV (Theory) or in MeV ± keV (Experiment). Theoretical and experimental width of resonance states is indicated in keV

^8Li					^8B				
J^π		MP	MHNP	Exp	J^π		MP	MHNP	Exp
3^+	E	0.049	0.610	0.223 ± 3	3^+	E	2.480	2.560	2.183 ± 20
	Γ	3	166	33 ± 6		Γ	495	572	350 ± 30
1^+	E	1.535	1.002	1.178	1^+	E	0.090	0.615	0.632 ± 2.5
	Γ	826	1433	≈ 1000		Γ	0.4	43.7	35.6 ± 0.6
1^+	E	4.619	2.129	3.368	1^-	E	1.441	1.132	
	Γ	22	913	≈ 650		Γ	989	1828	
3^+	E	2.458	3.625		0^+	E	1.644	1.128	
	Γ	2636	760			Γ	870	299	
4^+	E	4.486	3.190	4.498 ± 20	2^-	E	4.209	3.363	3.363 ± 500
	Γ	64	2	35 ± 15		Γ	632	4143	8000 ± 4000

Comparing theoretical and experimental parameters of resonance states, we come to the conclusion that the MHNP provides more precise description of resonance states in ^8Li and ^8B than the MP. One can see from Table 3, the energy and with of the 1^+ and 2^- resonance states in ^8B and the 1^+ resonance state in ^8Li, calculated with the MHNP, are close to experimental values. However, the MP providesfairly good description of parameters of 4^+ resonance statein ^8Li and 3^+ resonance state in ^8B.

The above mentioned results are obtained with taking into account the cluster polarization. To see explicitly the effects of cluster polarization, the polarizability of clusters is switched off. We demonstrate effects of the cluster polarization only for two bound states and two resonance states, determined with the MHNP. By switching off the cluster polarization in ^8Li, we obtain energy of the bound states $E(2+)$ =-1.25 MeV and $E(1+)$ =-0.54 MeV, which should be compared with

$E(2^+)$=-2.00 MeV and $E(1^+)$=-1.31 MeV. As we see, the cluster polarization decreases significantly energy of the bound states in ^8Li. Let us turn our attention to the resonance states. Note, that most part of resonance states in ^8Li (^8B), displayed in Table 3, are determined in the $^7Li + n$ ($^8Be + p$) elastic scattering. Consider the 1^+ resonance state in ^8B. By neglecting the cluster polarization we obtain parameters of the resonance state: E = 0.94 MeV and Γ = 163 keV. Comparing these parameters with the corresponding results in Table 3, we came to the conclusion that cluster polarization decreases 1.5 times energy and almost 4 times the total width of the 1^+ resonance state. More stronger effects of the cluster polarization is observed in the 3^+ resonance state in ^8Li. Energy of the resonance state is decreased from 2.438 MeV to 0.61 MeV and width is reduced from 1227 keV to 166 keV due to the cluster polarization.

Figures 1, 2 visualize effects of cluster polarization in ^8Li and ^8B. These results are obtained with the MHNP. In Figure 2, the orbital momentum l_1 denotes the orbital momentum of neutron with respect to ^7Li nucleus.

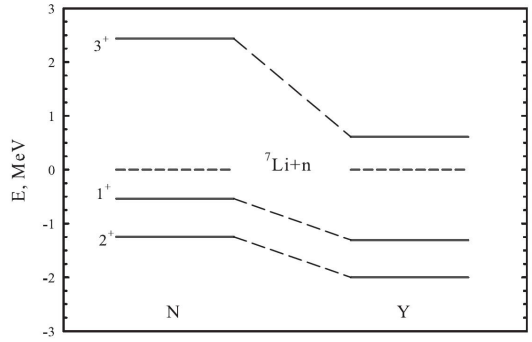

Figure 1 – Spectrum of two bound states and one resonance state in ^8Li obtained withou (N) and with (Y) cluster polarization

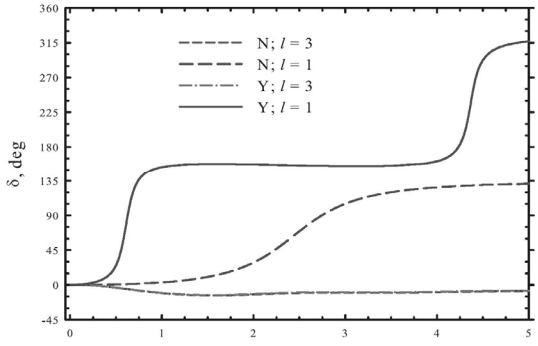

Figure 2 – Phase shifts of $n + ^7Li$ scattering with the total angular momentum $J^\pi = 3^+$.

One can see, that cluster polarization influences significantly on the phase shift of $n + ^7Li$ scattering with the orbital momentum of neutron l_1 = 1. However, effects of cluster polarization on $n + ^7Li$ scattering with l_1 = 3 is very small.

There is other way for visualization of cluster polarization. As was suggested in [1], by using wave function of a bound state of compound system, we can calculate how the average distance between two selected clusters depends on distance to the third cluster. For instance, we can calculate average distance between alpha particle and triton (^3He) when neutron (proton) is moving toward to ^7Li (^7Be).This quantity is displayed in Figure 3 for the ground 2^+ and first excited 1^+ states in ^8Li. When neutron is far away from ^7Li, the average distance between alpha particle and triton is approximately 4.5 fm. When neutron approach to ^7Li, theaverage distance is reduced slightly, and then it significantly stretched when the distance $R(n - ^7Li)$ is at range between 1.5 and 9 fm. Seems, at this range nucleus ^7Li changes it orientation with respect to neutron which results in such tremendous size of the system $\alpha + t$. And finally, when neutron is very close to the center of mass of ^7Li it compressed to minimal size of 1.6 fm. Thus, this figure demonstrates that ^7Li as a two-cluster system is strongly affected byincident neutron. Some what different picture is observed for the ground state of ^8B. Effects of incident proton on distance between alpha particle and ^3He is demonstrated in Figure 4. The incident proton gradually decreases size of ^7Be, which is due to a combination of nuclear forces and Coulomb interaction. The "phase transition", observed in bound states of ^8Li in a wide range of distance $R(n - ^7Li)$, now takes place in a very small range of $R(p - ^7Li)$ distance. However, an amplitude ofthe "phase transition" in ^8B is much more than in ^8Li. It should be notes that without polarization, all curves in Figuresand are transformed into plain lines, i.e. radius of two-cluster subsystem is independent on position of third cluster when polarization is neglected.

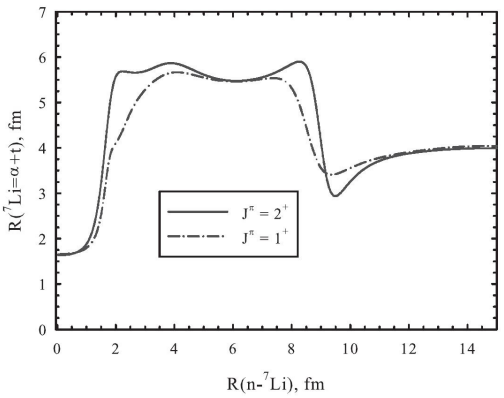

Figure 3 – Average distance between α particle and triton as a function of distance between neutron and ^{7}Li. Calculation is made with the MHNP

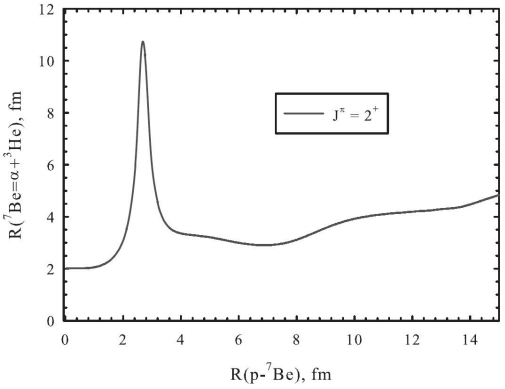

Figure 4 – Dependence of average distance between alpha particle and ^{3}He on distance to proton. Results are obtained with the MHNP

We have applied a three-cluster microscopic model for studying structure of bound states and reactions in ^{8}Li and ^{8}B. The model took into account polarizability of interacting clusters. It was demonstrated that the cluster polarization has large impact on properties of bound and resonance states and on the elastic scattering of neutron on ^{7}Li and proton on ^{7}Be. The present model provides fairly good description of the bound and resonance states in mirror nuclei ^{8}Li and ^{8}B.

Acknowledgment

This work is partially supported by the Ministry of Education and Sciences of Republic of Kazakhstan, The Research Grant IPS 3106/GF4.

References

[1] V. S. Vasilevsky. F. Arickx. J. Broeckhove. and T. P. Kovalenko.A microscopic three-cluster model with nuclear polarization applied to the resonances of ^{8}Be and the reaction $^{6}Li(p,^{3}He)^{4}He$ // Nucl. Phys. A.– 2009.– Vol. 824. – P. 37–57.

[2] A. V. Nesterov. V. S. Vasilevsky. and T. P. Kovalenko.Effect of cluster polarization on the spectrum of the ^{7}Li nucleus and on the reaction $^{6}Li(n,^{3}H)^{4}He$ // Phys. Atom. Nucl.– 2009. – Vol. 72. – P. 1450–1464.

[3] A. V. Nesterov. V. S. Vasilevsky. and T. P. Kovalenko.Microscopic model of the radiative capture reactions with cluster polarizability. Application to ^{8}Be and ^{7}Li // Ukr. J. Phys. – 2011.– Vol. 56. – P. 645–653.

[4] V. S. Vasilevsky. A. V. Nesterov. and T. P. Kovalenko.Three–cluster model of radiative capture reactions in seven-nucleon systems. Effects of cluster polarization // Phys. Atom. Nucl. – 2012. – P. 75. 818–831.

[5] J. P. Mitchell. G. V. Rogachev. at el. Low-lying states in ^{8}B // Phys. Rev. C.– 2010. – Vol.82. – P. 011601.

[6] J. P. Mitchell. G. V. Rogachev. at el.Structure of ^{8}B from elastic and inelastic ^{7}Be+p scattering // Phys. Rev. C. – 2013. – Vol. 87. – P. 054617.

[7] L. D. Faddeev and S. P. Merkuriev. Quantum Scattering Theory for Several Particle Systems // Dordrecht. Boston. London: Kluwer Academic Publishers. – 1993.

[8] K. Wildermuth and Y. Tang.A unified theory of the nucleus. Braunschweig: Vieweg Verlag. – 1977.

[9] D. R. Thompson. M. LeMere. and Y. C. Tang. Systematic investigation of scattering problems with the resonating-group method // Nucl. Phys. A. – 1977. – Vol. 286. – P. 53–66.

[10] I. Reichstein and Y. C. Tang. Study of $N+\alpha$ system with the resonating-group method // Nucl. Phys. A.– 1970. – Vol. 158. – P. 529–545.

[11] A. Hasegawa and S. Nagata. Ground state of ^{8}Li // Prog. Theor. Phys.– 1971.– Vol. 45. – P. 1786–1807.

[12] F. Tanabe. A. Tohsaki. and R. Tamagaki. αα scattering at intermediate energies // Prog. Theor. Phys. – 1975. – Vol. 53. – P. 677–691.

[13] D. R. Tilley. J. H. Kelley. at el. Energy levels of light nuclei A=8. 9. 10 // Nucl. Phys. A. – 2004. – Vol. 745. – P. 155–362.

[14] M. M. Obuti. T. Kobayashi. at el. Interaction cross section and interaction radius of the ^{8}B nucleus // Nucl. Phys. A. – 1996. –Vol. 609. – P74–90.

[15] A. Csótó. Proton skin of ^{8}B in a microscopic model // Phys. Lett. B. – 1993. – Vol. 315. – P. 24–28.

[16] D. Baye. P. Descouvemont. and N. K. Timofeyuk. Matter densities of ^{8}B and ^{8}Li in a microscopic cluster model and the proton-halo problem of ^{8}B // Nucl. Phys. A. – 1994. – Vol 577. – P. 624–640.

UDC 539

Formation and decay of resonance state in ^9Be and ^9B nuclei. Microscopic three-cluster model investigations

Vasilevsky V.S.[1*], Kato K.[2], Takibayev N.Zh.[3]

[1]*Bogolyubov Institute for Theoretical Physics, 14-B, Metrolohichna str., Kiev, Ukraine*
[2]*Nuclear Reaction Data Centre, Faculty of Science, Hokkaido University, Sapporo, Japan*
[3]*Department of Physics and Technology, al-Farabi Kazakh National University, 71 al-Farabi av., Almaty, Kazakhstan*
[*]*e-mail: vsvasilevsky@gmail.com*

We study nature of the low-lying resonance states in mirror nuclei ^9Be and ^9B. Investigations are performed within a three-cluster model. The model make uses of the hyperspherical harmonics, which provide convenient description of three-cluster continuum. Much attention is paid to the controversial $1/2^+$ resonance states in both nuclei. We study effects of Coulomb interaction on energy and width of three-cluster resonances in the mirror nuclei ^9Be and ^9B. We look for the Hoyle-analogue states which allows for alternative way of ^9Be and ^9B synthesis in a triple collision of clusters.

Key words: Microscopic model, triple collision, resonance state.
PACS number(s): 24.10.-i, 21.60.Gx

1 Introduction

Resonance state is one of the challenging problems for theoretical and nuclear physics. There are common features of resonance states, observed in a few- or many-channel systems.However, there are some specific features connected with the way of excitation or generation of resonance statesand also in different way of resonance state decay in nuclear systems. Special attention is attracted by resonance states formed by three interacting clusters, i.e. resonance states embedded in three-cluster continuum. Such resonance states are repeatedly observed in nuclei with well-determined three-cluster structure. These nuclei have dominant three-cluster configuration, it means that bound states and many resonance states are lying bellow and above, respectively, threshold of three-cluster continuum. In other words, bound states and large part of resonance states in three-cluster nuclei are generated by an interaction of three clusters. Asexamples of such nuclei, we can mention ^5H, ^6He and ^6Be, ^9Be and ^9B and many others.

In present paper, a microscopic three-cluster model is applied to study nature of resonance states in ^9Be and ^9B. Dominant three-cluster configurations $\alpha + \alpha + n$ and $\alpha + \alpha + p$, respectively, are selected to describe the low excitation energy region in these nuclei. Microscopic model, which was formulated in [1], make uses of total basis of oscillator functions to describe intercluster motion. The model is called as AM HHB which stands for the Algebraic three-cluster Model with the Hyperspherical Harmonics Basis.The first application of this model to study resonance structure of ^9Be and ^9B was made in Ref. [2]. Results presented in [2] were obtained with the Minnesota potential.In present paper we make use of the modified Hasegawa-Nagata potential, and we pay much more attention to the $1/2^+$ resonance states, the Coulomb effects on resonance states in mirror nuclei. Besides, we look for the Hoyle analogue states in ^9Be and ^9B.

2 Model formulation

In this section we shortly outline main ideas of the model. We start with a wave function of nucleus consisting of three clusters, as this a key element of model formulation. To describe three-cluster system one has to construct a three-cluster function

$$\Psi_{JM_J} = \left\{\left[\left[\Phi_1\left(A_1,s_1\right)\Phi_2\left(A_2,s_2\right)\right]\Phi_3\left(A_3,s_3\right)\right]_S f_L^{(J)}\left(\mathbf{x},\mathbf{y}\right)\right\}_{JM_J} \quad (1)$$

and by solving many body Schrödinger equation one has to determine intercluster wave function $f_L^{(J)}(\mathbf{x},\mathbf{y})$ and spectrum of bound state(s) or *S*-matrix for states of continuous spectrum. Jacobi vectors **x** and **y** determine relative position of clusters. Wave functions $\Phi_\alpha(A_\alpha,s_\alpha)$ (α=1, 2, 3), describing internal motion of cluster consisted of A_α nucleons and with the spin s_α, are assumed to be fixed, they posses some very important features, such as, for instance, they are antisymmetric andtranslation-invariant ones. Adiabaticity, connected with a fixed form of the wave functions $\Phi_\alpha(A_\alpha,s_\alpha)$, is the main assumption of the method which is well-known as the resonating group method [3]. Wave function is projector operator which reduces many-particle problem to three-body problem with nonlocal and energy-dependent potential (see detail in Ref. [3]). For amplitudes

$$f_L^{(J)}(\mathbf{x},\mathbf{y}) = f_{\lambda,l;L}^{(J)}(x_3,y_3)\left\{Y_\lambda(\hat{x})Y_l(\hat{y})\right\}_{LM_L} \quad (2)$$

one can deduce an infinite set of the two-dimension integro-differential equations. This set of equations can be more simplified, if we introduce hyperspherical coordinates $\Omega=\{\theta,\hat{x},\hat{y}\}$

$$x=\rho\cos\theta, \quad y=\rho\sin\theta, \quad (3)$$

and construct full set of orthonormalized hyperspherical harmonics (see definition of the harmonics, for instance, in [4], [1])

$$\mathcal{Y}_{K,l_1,l_2,LM}(\Omega) = \chi_{K,l_1,l_2}(\theta)\left\{Y_\lambda(\hat{x})Y_l(\hat{y})\right\}_{LM_L} \quad (4)$$

then wave function (1) represented as

$$\Psi_{JM_J} = \sum_{K,l_1,l_2,L}\left\{\left[\left[\Phi_1(A_1,s_1)\Phi_2(A_2,s_2)\right]\Phi_3(A_3,s_3)\right]_S \times \psi_{K,l_1,l_2;L}(\rho)\mathcal{Y}_{K,l_1,l_2;L}(\Omega)\right\}_{JM_J}, \quad (5)$$

where hyperradial components $\psi_{K,l_1,l_2;L}(\rho)$ of wave function obey an infinite set of integro-differential equations. Last step toward the simplification of numerical solution of such system of equations is to expand the hyperradial amplitudes $\left\{\psi_{K,l_1,l_2;L}(\rho)\right\}$ over basis of hyperradial part of oscillator functions in six-dimension space

$$\psi_{K,l_1,l_2;L}(\rho) = \sum_{n_\rho} C_{n_\rho K,l_1,l_2;L}(b)R_{n_\rho,K}(\rho,b), \quad (6)$$

where $R_{n_\rho,K}(\rho,b)$ is an oscillator function

$$R_{n_\rho,K}(\rho,b) = (-1)^{n_\rho}\mathcal{N}_{n_\rho,K}r^K\exp\left\{-\frac{1}{2}r^2\right\}L_{n_\rho}^{K+3}(r^2), \quad (7)$$

$$r=\rho/b, \quad \mathcal{N}_{n_\rho,K}=b^{-3}\sqrt{\frac{2\Gamma(n_\rho+1)}{\Gamma(n_\rho+K+3)}},$$

and b is oscillator length.

Expansion over oscillator basis reduces the set of integro-differential equations to the system of linear algebraic equations for expansion coefficients

$$\sum_{\tilde{n}_\rho,\tilde{c}}\left\{\left\langle n_\rho,c\middle|\hat{H}\middle|\tilde{n}_\rho,\tilde{c}\right\rangle - E\left\langle n_\rho,c\middle|\tilde{n}_\rho,\tilde{c}\right\rangle\right\}C_{\tilde{n}_\rho,\tilde{c}} = 0, \quad (8)$$

where multipole index *c* denotes channel of the hyperspherical basis $c=\{K,l_1,l_2;L\}$. This system is relevant for bound states and for continuous spectrum states. To obtain spectrum of bound states, one can use diagonalization procedure for the reduced set of the equations. However, to find wave functions and elements of the scattering *S*-matrix, one has to implement in (8) proper boundary conditions for expansion coefficients. These conditions were thoroughly discussed in Ref. [1].

3 Spectrum of resonance states in ^9Be and ^9B

To perform numerical calculations, we need to fix few parameters and select nucleon-nucleon potential. We start with selection of nucleon-nucleon potential. We exploit the Modified Hasegawa-Nagata potential (MHNP) [5, 6] to model nucleon-nucleon interaction. This is a semi-realstic potential and it was intensively used in numerous many-cluster systems, as it provides good description of the internal structure of clusters and interaction

between clusters as well After NN potential was selected, we need to fix three input parameters: oscillator length b, number of channels or number of hyperspherical harmonics and number of hyper radial excitations. We restrict ourselves with a finite set of the hyperspherical harmonics, which is determined by maximal value of the hyperspherical momentum K_{min}. To describe the positive parity states we use allhyperspherical harmonics withthe hypermomentum $K \leq K_{min} = 14$, the negative parity states are described by the hyperspherical harmonics with $K \leq K_{min} = 13$.These amounts of the hyperspherical harmonics account for many different scenarios of three-cluster system decay. We also restrict ourselves with number of the hyperradial excitation $n_\rho \leq 100$. This allows us to rich an asymptotic region, where all clusters are well separated and cluster-cluster interaction, induced by nucleon-nucleon potential, is negligible small.

Table 1 – Spectrum of bound and resonance states of ^9Be calculated with the MHNP

	Exp.		AM HHB, MHNP	
J^π	E (MeV ± keV)	Γ (MeV ± keV)	E (MeV)	Γ (MeV)
$3/2^-$	-1.5735		-1.5743	
$1/2^+$	0.111 ±7	0.217 ± 10	0.338	0.168
$5/2^-$	0.8559 ±1.3	0.00077 ±0.15	0.897	$2.363 \cdot 10^{-5}$
$1/2^-$	1.21 ±120	1.080 ± 110	2.866	1.597
$5/2^+$	1.476 ±9	0.282 ± 11	2.086	0.112
$3/2^+$	3.131 ±25	0.743 ± 55	4.062	1.224
$3/2^-_2$	4.02 ±100	1.33 ± 360	2.704	2.534
$7/2^-$	4.81 ±60	1.21 ± 230	4.766	0.404
$9/2^+$	5.19 ±60	1.33 ± 90	4.913	1.272
$5/2^-_2$			5.365	4.384
$7/2^+$			5.791	3.479

In present paper, the oscillator length b is selected to minimize the bound state energy of alpha particle, which is obtained with b = 1.317 fm. This allows us to describe correctly the internal structure of the alpha particle. If we take original form of the modified Hasegawa-Nagata potential, we obtain the overbound ground state in ^9Be and the bound state $3/2^-$ state in ^9B. The latter contradicts to experiments. The similar situation was observed for the Minnesota potential.To avoid this unphysical situation, we changed slightly parameters of the MHNP in order to reproduce bound state energy of ^9Be. Thus, by modifying the Majorana parameter, we obtain correct value of the binding energy of ^9Be. This is achieved with m = 0.4389, which can be compared to the original value m = 0.4057. With this value of the Majorana parameter, the spectrum of resonance states in ^9Be and ^9B is calculated.

Now we turn our attention to the spectrum of ^9Be and ^9B nuclei. Results of calculations with the MHNP is presented in Tables 1 and 2 where we compare our results with the experimental data [7]. Our calculations are in fairly good agreement with available experimental data. Energy and width of some resonance states are rather close to experimental data. For instance, parameters of $5/2^-$ and $9/2^+$ resonance states in ^9Be, and parameters $5/2^-$, $1/2^-$ and $5/2^+$ resonance states in ^9B.

That means that we found correct interaction between clusters in ^9B and ^9Be. In this paper as in the previous one [2], we use the same parameters of nucleon-nucleon interactions for all other J^π states. Comparing results of presvious and present calculations, we conclude that the modified Hasegawa-Nagata potential generates more correct cluster-cluster interaction for large set of the J^π states, thanthe Minnesota potential.We also conclude that spectrum of resonance states in ^9B and ^9Be strongly depends on peculiarities of nucleon-nucleon interaction.

Table 2 – Experimental and theoretical spectrum of resonance states of ^9B

	Exp.		AM HHB, MHNP	
J^π	E (MeV ± keV)	Γ (MeV ± keV)	E (MeV)	Γ (MeV)
$3/2^-$	0.277	0.00054 ±0.21	0.379	$1.076 \cdot 10^{-6}$
$1/2^+$	(1.9)	$\simeq 0.7$	0.636	0.477
$5/2^-$	2.638 ±5	0.081 ± 5	2.805	0.018
$1/2^-$	3.11	3.130 ± 200	3.398	3.428
$5/2^+$	3.065 ±30	0.550 ± 40	3.670	0.415
$3/2^+$			4.367	3.876
$3/2^-_2$			3.420	3.361
$7/2^-$	7.25 ±60	2.0 ± 200	6.779	0.896
$9/2^+$			6.503	2.012
$5/2^-_2$			5.697	5.146
$7/2^+$			7.100	4.462

Now we concentrate our attention on the $1/2^+$ resonance states in ^9B and ^9Be. In Figures 1 and 2 we display phase shifts of $3 \Rightarrow 3$ scattering for the $1/2^+$ state in ^9B and ^9Be, respectively. These results are obtained with $K_{max} = 14$ and with the MHNP. With such value of K_{max}, 32 channels are involved in calculations and only three of them produces phase shifts which are not very small at energy region $0 \le E \le 5$ MeV. The phase shift connected with the channel $c = \{K = 0, l_1 = l_2 = L = 0\}$ of ^9Be shows resonance behavior at energies $E = 0.338$ MeV and $E = 1.432$ MeV.Second resonance state is also reflected in the second channel $c = \{K = 2, l_1 = l_2 = L = 0\}$ as a shadow resonance.

Phase shifts for $1/2^+$ state in ^9B also exhibit resonance states at two energies $E = 0.636$ MeV and $E = 2.875$ MeV. As in case of ^9Be, $1/2^+$ resonance states in ^9B are connected with only one channel $c = \{K = l_1 = l_2 = L = 0\}$. Due to Coulomb interaction, resonance states in ^9B are shifted to higher energy range with respect to position of these resonance states in ^9Be.

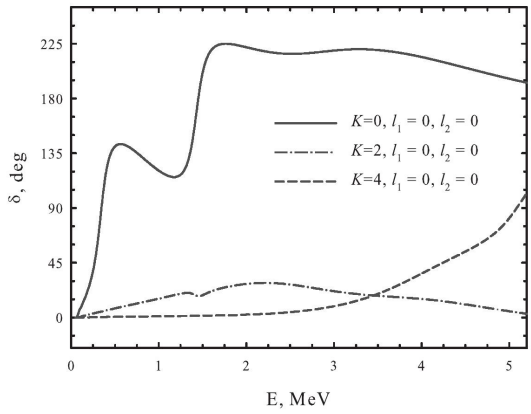

Figure 1 – Phase shifits for $3 \Rightarrow 3$ scattering in $1/2^+$ state in ^9Be

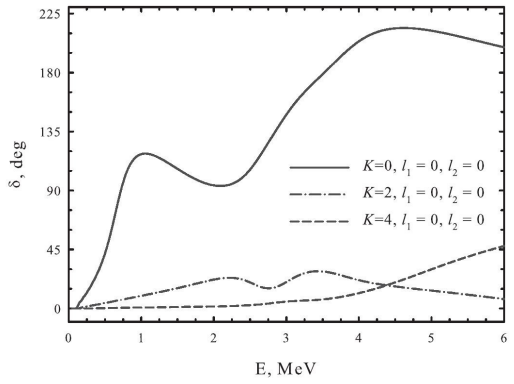

Figure 2 – Phase shifts for $1/2^+$ state in ^9B

To understand nature of $1/2^+$ and other resonance states in ^9B and ^9Be, we analyze wave functions. As was mentioned above wave function of three-cluster system is many-component and huge objects which is difficult to analyze. The simplest way for analyzing wave function of a resonance state is to study weights of oscillator shells. The weights are determined as follows

$$W_{sh} = W_{sh}\left(N_{sh}\right) = \sum_{n_\rho, c \in N_{sh}} \left| C_{n_\rho, c} \right|^2$$

It is important to note that oscillator wave functions with small values of N_{sh} describe very compact configurations of three-cluster system, when distance between interacting clusters is very small. Oscillator functions with large values of N_{sh} account for configuration of three-cluster system with large distance between all clusters and/or when one cluster is far away from two other clusters. In Fig. 3 we show the weight W_{sh} of different oscillator shell N_{sh} (N_{sh} = 0, 1, 2, ...) in wave function of resonance states. One can see that wave function of the $1/2^+$ resonance in ^9Be is similar to wave function of the resonance state in ^9B and both of them are represented by the oscillator shells with large values of N_{sh}. Figure 3 display behavior of wave function which is typical for low-energy wave functions. In asymptotic region these functions has an oscillatory behavior. Like in two-body case with sort-range interaction, the smaller energy, the larger is distance to the first node of wave function. In oscillator space we have approximately the same picture as in coordinate space. This is because there is simple relation between wave function in coordinate space and expansion coefficients in oscillator representation (see detail, for instance, in [1]).

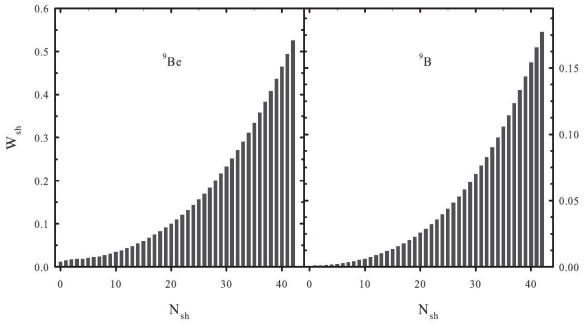

Figure 3 – Weights of different oscillator shells in wave functions of $1/2^+$ resonance states in ^9Be and ^9B.

By analyzing the total and partial widths, we determine the dominant decay channels of three-cluster resonance state. This analysis help us to shed some light on the nature of a resonance channel in many-channel system. It can be performed for two different trees of the Jacobi vectors, which were denoted as $n + {}^9Be$ and $^4He + {}^5He$ in Ref. [2]. The $1/2^+$ resonance state in ^9Be and ^9B has only dominant channel. In the first tree, the resonance prefer to decay into the channel, where the relative orbital momentum of two alpha particles and the orbital momentum of valence neutron (with respect to the center of mass of two alpha particles) equal zero. Partial width connected with that channel almost coincides with the total width. The same situation is observed in the second tree. There is also only one dominant channel with zero values of partial orbital momenta. The first orbital momentum represents relative motion of neutron around first alpha particle and the second one represents relative motion of second alpha particle with respect to the center of mass of the subsystem $\alpha + n$. These properties of the $1/2^+$ resonance states in ^9Be and ^9B are based on two important factors. First factor is the dominant role of the channel with the hypermomentum $K = 0$ in wave function of the resonance state. The second factor is connected with the essential properties of the hyperspherical harmonics with $K = 0$. With this value of hypermomentum, we have got only one hyperspherical harmonic which is independent on choice of the Jacobi vector tree.

Let us now consider the Hoyle analogue states in ^9Be. We recall that the Hoyle state is a very narrow resonance state in ^{12}C. It lies not far from the three-cluster threshold ($E = 0.38$ MeV) and has very small width $\Gamma = 8.5$ eV. This resonance state is created by collision of three alpha particles with total angular momentum and parity $J^\pi = 0^+$. As we see, the main features of the Hoyle resonance state that it is very long-lived resonance state (according to nuclear scale). If we look at Table 1, we find that ^9Be has two resonance states ($1/2^+$ and $5/2^-$) which lie close to the three-cluster threshold $\alpha + \alpha + n$. The $1/2^+$ resonance state is created by two values of the total orbital momentum L=0 and L=1. However, the resonance state is not narrow one, as ratio Γ / E is large $\Gamma / E \approx 0.5$. Meanwhile, the $5/2^-$ resonance state is indeed narrow resonance state because width is small Γ = 23,6eV and besides ratio Γ / E is also very small: it equals $\Gamma / E \approx 2.63 \cdot 10^{-5}$ in our model and experimental ratio is $\Gamma / E \approx 9{,}0 \cdot 10^{-4}$. One can compare this ratio with the experimental ratio for the Hoyle state $\Gamma / E \approx 2{,}24 \cdot 10^{-7}$.

We believe that this resonance state is of the Hoyle-analogue state. This state has quite large half-life time, it could emit quadrupole gamma quanta and transit to the ground state of ^9Be. This is one of possible ways for synthesis of ^9Be. We assume, that in stars with large densities of alpha-particles and neutrons this is very plausible way of creating ^9Be nuclei.

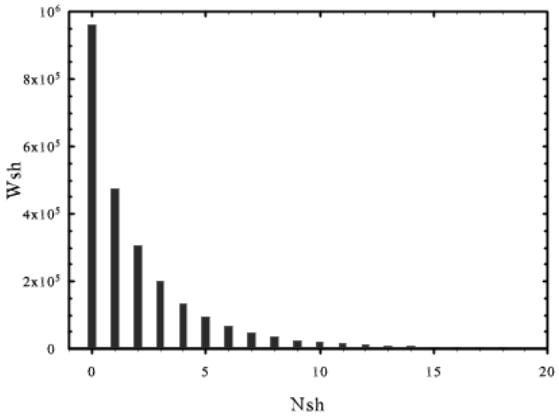

Figure 4 – Weights of different oscillator shells in wave function of the $5/2^-$ resonance state in ^9Be

In Figure 4 we demonstrate weight W_{sh} of different shells in wave function of the $5/2^-$ resonance state. It can be concluded from the Figure that the $5/2^-$ resonance state is very compact object, as it mainly represented by the oscillator shells with small number of N_{sh}. Besides, wave function of the resonance state has a very large amplitude in internal region ($W_{sh} \leq 10^6$). Such behavior of wave function of the $5/2^-$ resonance state in ^9Be is very similar to behavior of wave function of the Hoyle state in ^{12}C.

Three-cluster microscopic model was applied to study resonance states in mirror nuclei ^9Be and ^9B. The model make use of the hyperspherical harmonics to numerate channels of three cluster continuum and simplify of solving of the Schrödinger equation for many-particle and many-channel system. The modified Hasegawa-Nagata potential modelled nucleon-nucleon interaction. It was shown that the model with such NN interaction provides good description of parameters of resonance states. It was shown that $1/2^+$ states in ^9Be and ^9B are resonance states. Very narrow $5/2^-$ resonance state in ^9Be can be considered as the Hoyle-analogue state, we assume that this state is key resonance state for synthesis of ^9Be in a triple collision of alpha particles and neutron.

Acknowledgment

This work is partially supported by the Ministry of Education and Sciences of Republic of Kazakhstan, The Research Grant IPS 3106/GF4.

References

[1] V. Vasilevsky. A. V. Nesterov. F. Arickx. and J. Broeckhove.Algebraic model for scattering in three-s-cluster systems. I. Theoretical background // – Phys. Rev.C. – 2001 – Vol. 63.–P. 034606.

[2] A. V. Nesterov. V. S. Vasilevsky. and T. P. Kovalenko.Nature of Resonance States in the ^9Be and ^9B Mirror Nuclei // Phys. Atom. Nucl.– 2014. – P. 77. –555–568.

[3] K. Wildermuth and Y. Tang.A unified theory of the nucleus // Braunschweig: Vieweg Verlag, 1977.

[4] R. Jibuti and N. Krupennikova. Method of Hyperspherical Functions in quantum mechanics of few body systems. (In Russian). // Tbilisi: Micniereba, 1984.

[5] A. Hasegawa and S. Nagata. Ground state of ^{6}Li // – Prog. Theor. Phys. – 1971. – Vol. 45. – P. – 1786–1807.

[6] F. Tanabe. A. Tohsaki. and R. Tamagaki. $\alpha\alpha$ scattering at intermediate energies. // Prog. Theor. Phys. – 1975. – Vol. 53. – P. 677–691.

[7] D. R. Tilley. J. H. Kelley. J. L. Godwin. D. J. Millener. J. E. Purcell. C. G. Sheu. and H. R. Weller. Energy levels of light nuclei A =8. 9. 10 // Nucl. Phys. A. – 2004. – Vol. 745. – P. 155–362.

UDC 539.17; 539.1.01; 524.354.6

Forced reverse reactions in neutron star matter

Takibayev N.Zh.

Department of Physics and Technology, al-Faraby KazNU, Almaty, Kazakhstan,
Institute of Experimental and Theoretical Physics, Almaty, Kazakhstan,
e-mail: takibayev@gmail.com

Nuclear reactions in neutron star envelopes are considered in the frame of complex interactions stimulated by huge pressures in the overdense crystalline structures in the envelopes. It leads to the inclusion of forced reverse reactions that transform the nuclei to neutron-rich states and the appearance of free neutrons. The free neutrons in the structures cause resonance interactions with nuclei that fixed in nodes of crystal. The neutron re-scattering on subsystem of few nucleus at the energy near the energy of resonance level of the nucleus creates the few-body resonances, which depend on the distances between the nuclei.

Key words: neutron star, nonlinear interactions, neutron resonances with few-nuclei, electron capture reactions.
PACS number(s): 28.20.Pr, 26.60.Gj, 21.45.-v

1 Introduction

The main reactions and processes that take place in the neutron star envelopes can be described in the frame of modern physical theory and methods [1-6]. In the outer and inner crusts of the envelopes, which surrounding the liquid mantel in deep of neutron star, represent itself the dense crystalline structure. This crystalline structure created by the bare nuclei situated in the lattice nodes is sunk into degenerated fermi-liquid of electrons. This construction is an electrically neutral; the nuclei in nodes of the crystal still have the well-known properties. The distances between the nuclei in the structure are much smaller than the atomic size, but are still much larger than nuclear radius.

However, the behavior of the matter in the region from 10^7 g·cm^{-3} up to 10^{14} g·cm^{-3} is governed not only by the two-body interactions, but also by the few-body forces and some sorts of quasi-particles that act in the crystalline structure [5-8].

Here, we do not consider the effect of external fields, focusing our attention on the impact of close neighbors in the crystalline structure. We take into account the properties of matter at different depths of the structure layers created by the powerful gravitational pressure.

The two-body interactions are undoubtedly important and essential at usual pressures and temperatures, and the applicable even more broadly, but for extremely high densities of matter, the few-body dynamics becomes very important, especially in the ordered structure of matter that appears in the neutron star envelopes.

In next sections, we investigate how the crystalline structure can affect the neutron resonances and create specific additional characteristics. We would also try to consider several intriguing questions.

2 The electron capture reactions

General characteristics of the overdense matter in the envelopes of neutron stars can be estimated employing an assumption that at ultrahigh pressures the structure of matter is simplified by acquiring the most favorable face-centered cubic structure [5].

The nuclear reactions in the neutron star envelopes start from the reactions of electron capture by nuclei. These reactions depend on specific properties of the nuclides. Therefore, the each stable nucleus of original neutron star substance has its own chain of electron capture reactions. Remarkable that most part of even-even nuclei give the two-step electron capture reactions because of after the first (i.e. mother) reaction follows the second (or daughter) reaction which is already open. The resulting daughter nuclei, which decay via the weak link in the terrestrial conditions, would remain stable in the overdense matter in the neutron star envelopes. They cannot emit the captured electrons owing to opposition of the degenerated Fermi electron liquid (see Fig.1).

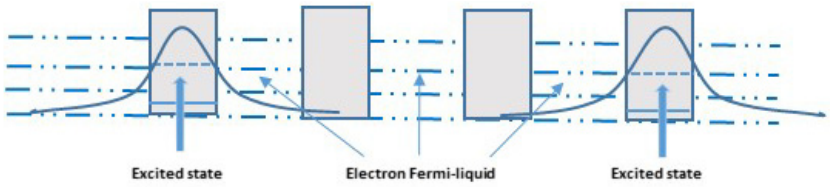

Figure 1– Nuclei in degenerated electron Fermi-liquid

It is remarkable that in many reactions that have the two-step characters the daughter nuclei, which appear in the second reactions, would arise both in the ground and in the excited states. The ban owing to quantum numbers between excited levels of nuclei demonstrates the interesting patterns.

The excited nuclei arise mostly in reactions with the iron group nuclei. The chains of reactions generated by Fermi electrons with the iron group nuclei are given in the Table 1.

Here, the following notations are used: Cr - is the name of a nuclide (chromium in this case), A is the number of nucleons in the nucleus, Z is the number of protons, e^- is an electron and ν_e - electron neutrino; $E_{e;th}$ is the threshold of the electron energy in reactions of the electron capture by a nucleus. The kinetic energy of an electron equals $E_e = E_F - m_e c^2$ and $E_e \geq E_{e;th}$. The estimates of the threshold energies for the electron capture reactions were performed employing the data available in the nuclear databases [9-12].

Table 1 – The chains of reactions generated by Fermi electrons with even-even nuclei of the iron group. The energies are given in MeV.

Main reaction	$E_{e;th}$	Daughter reactions	$E_{e;th}$
${}^{52}_{24}Cr^{0+} + e^- \rightarrow {}^{52}_{23}V + \nu_e$	3.97	${}^{52}_{23}V + e^- \rightarrow {}^{52}_{22}Ti + \nu_e$	1.977
${}^{54}_{26}Fe^{0+} + e^- \rightarrow {}^{54}_{25}Mn^{3+} + \nu_e$	0.697	${}^{54}_{25}Mn + e^- \rightarrow {}^{54}_{24}Cr^{0+} + \nu_e$	-1.377
${}^{54}_{24}Cr + e^- \rightarrow {}^{54}_{23}V + \nu_e$	7.042	${}^{54}_{23}V + e^- \rightarrow {}^{54}_{22}Ti + \nu_e$	4.301
${}^{56}_{26}Fe^{0+} + e^- \rightarrow {}^{56}_{25}Mn^{3+} + \nu_e$	3.695	${}^{56}_{25}Mn^{3+} + e^- \rightarrow {}^{56}_{24}Cr^{0+} + \nu_e$	1.629
${}^{56}_{24}Cr + e^- \rightarrow {}^{56}_{23}V^{3+} + \nu_e$	9.201	${}^{56}_{23}V + e^- \rightarrow {}^{56}_{22}Ti + \nu_e$	7.14
${}^{58}_{26}Fe^{0+} + e^- \rightarrow {}^{58}_{25}Mn^{3+} + \nu_e$	6.323	${}^{58}_{25}Mn^{3+} + e^- \rightarrow {}^{58}_{24}Cr^{0+} + \nu_e$	4.0
${}^{58}_{28}Ni + e^- \rightarrow {}^{58}_{27}Co + \nu_e$	0.381	${}^{58}_{27}Co + e^- \rightarrow {}^{58}_{26}Fe + \nu_e$	-2.307
${}^{64}_{30}Zn^{0+} + e^- \rightarrow {}^{64}_{29}Cu^{1+} + \nu_e$	0.579	${}^{64}_{29}Cu^{1+} + e^- \rightarrow {}^{64}_{28}Ni^{0+} + \nu_e$	-1.675

Note that the first reactions of electron capture (the first column in Table 1) have the positive threshold energies (the second column) higher than the threshold for the next (daughter) reactions (the third column). It means that the Fermi-electron energies are sufficient in these reactions to overcome the threshold energy (the fourth column).

As an example, we consider the isotope of ^{56}Fe,

$$
\begin{aligned}
&{}_{25}Mn^{3+} + e^- \rightarrow {}_{24}Cr^{0+} + \nu_e;\ E_{ext} = 2.066\ \text{MeV};\\
&{}_{25}Mn^{3+} + e^- \rightarrow {}_{24}Cr^{*2+} + \nu_e;\ E^* = 1.059\ \text{MeV};\\
&{}_{25}Mn^{3+} + e^- \rightarrow {}_{24}Cr^{**2+} + \nu_e;\ E^{**} = 0.234\ \text{MeV}.
\end{aligned}
\qquad (1)
$$

Here in (1), the two last reactions generate ${}^{56}_{24}Cr$ nuclei that appear in the excited states. It is very important that these excited nuclei cannot emit gammas because the distances between the nuclei are much less than the wavelengths of the gamma radiation. Note that nuclei are fixed in the nodes of the lattice.

For the nuclei with odd mass numbers, the threshold energies of the daughter reactions are higher than the threshold energies of the mother

reactions. So that the daughter nuclei in the excited states cannot appear in the electron capture reactions.

3 Nonlinear interactions

3.1 High harmonic generation.

The nuclear reactions and processes that occur in neutron star envelopes were considered in the frame of their mutual influences. Most part of these are stimulated by overdense matter transforming it to exotic states, which cannot appear in ordinary terrestrial conditions or in laboratory experiments.

At large amplitudes of the electromagnetic waves, the total dipole moment depends non-linearly on the amplitude of the incident wave. At higher densities, it leads to the birth of the secondary higher harmonic waves, i.e. the waves of doubled frequency, tripled, and even higher multiplicities.

The phenomena of light frequency multiplications are observed in the processes of which has the abundance in nature 91.754 %, concerning other iron isotopes. The first electron capture reaction starts for this isotope at the kinetic energy of the Fermi-electron E_e = 3.695 MeV. It requires the matter density be $\rho > \rho_{th} \approx 7.155\ 10^9$ g/cm^3. The daughterly reactions (Table 1, coulomb 3) can undergo the following three possible ways (here A = 56):

laser photonic interactions in special devices [13-15].

At that, two or more electromagnetic waves are absorbed and one photon is emitted at a frequency equal to the amount of absorbed waves. It means the nonlinear medium absorbs two waves ω_1, ω_2 with frequency $\omega_3 = \omega_1 + \omega_2$.

High harmonic generation has interesting properties that result in terrestrial experiments as generation of light with frequencies much greater than the original ones (typically 100 to 1,000 times greater). This phenomenon depends on the driving field and generates the harmonics with similar temporal and spatial coherence properties [13, 16, 17]. High harmonics are often generated with pulse durations shorter than those of the driving laser. This is due to the non-linearity of the generation process and the phase matching.

Considering the overdense matter in the envelopes of neutron stars, one should note that the process of high-multiplicity gamma emission stimulated by nuclei depends on the density of these nuclei in the respective layers of the envelopes. Taking into account the diffusion rate of the impurity nuclei in the crystal structure, their grouping and localization, we can talk about their high local density. Accordingly, this should lead to a high probability of a collective emission of gamma rays of high multiplicity with energies of almost an order of magnitude greater than the excitation energy of an individual nucleus.

In our case, we can consider the excited nuclei instead of the pump photons and their virtual emissions as photons, which also play the role of inducing waves. In the overdense crystalline structure, the excited nuclei interact non-linearly between each other and emit together the gamma rays of high multiplicity. The emission of gamma becomes induced in the case of any photons ≥ 1, which are already emitted in this mode.

The excited nuclei can be considered in overdense crystal as the sources of compressed photons. The combined radiations from such sources would create the modes of high multiplicity, i.e. high-energy gammas.

3.2 Tunneling Effects.

Obviously, it is very challenging to consider the complete manifold of the interactions between the stable and excited nuclei in an overdense crystalline structure. However, particular significance in the super-dense crystalline structures acquires tunneling effects because, unlike the dense gas environments, here the tunneling phenomenon has its own ordered pattern. Imagine, for example, the quasi-particle motion inside the nucleus as the motion in the potential well. Let the energy of the quasiparticle excitation energy be equal to E^*, and the height of the well be E_F.

The nuclei are immersed in a degenerate electron Fermi liquid, which prohibits the output of gamma rays that have energies below the Fermi energy of the electrons. Let us also consider two neighboring wells, i.e. two adjacent excited nuclei. The overlap coefficient of the wave functions can be defined in this simplified model employing a simple formula

$$D(d^*) = D_0 /[1+ (k^2 + \kappa^2)^2/4\ k^2 \cdot \kappa^2\ sh(\kappa \cdot d^*)] \quad (2)$$

where

$$k = [2m^* \cdot E^*]^{1/2} /\hbar\ ;\ \kappa = [2m^* \cdot (E_F - E^*)]^{1/2} /\hbar \quad (3)$$

Here, $D_0 \approx 1$ is the normalized overlap integral of the two identical wave functions of the nuclear excited states taken at $d^* = 0$; m^* is the effective mass of the quasi-particle. In reality $d^* \geq d$, where d is the lattice constant.

Then one can write $d/d^* = (\rho^*/\rho)^{1/3}$.

Summing (2) over all the neighboring excited nuclei, one can obtain the dependence of the overlap integral of the excited nuclei density $\Omega(\rho^*)$ in the lattice as:

$$\Omega(\rho^*) = \Sigma_p D(p \cdot d_{av}) \quad (4)$$

where d_{av} is the average distance between the single excited nuclei p = 1,2,3 … The overlap integrals with highly excited states are to be also included in the sum $\Omega(\rho^*)$ by introducing the wave numbers

$$k_n = [2m^* \cdot E_n^*]^{1/2}/\hbar \ ,$$
$$\kappa_n = [2m^* \cdot (E_F - E_n^*)]^{1/2}/\hbar \quad (5)$$

where E_n^* is the energy of the related states. Equating the sum (4) to unity, one can get the critical value for the density of the excited states of the nuclei in the lattice:

$$\rho^*/\rho = d^3 (k_n \cdot \kappa_n)^{3/2} \quad (6)$$

This shows that at low d and κ_n, the critical values can occur even with low concentrations of excited nuclei.

4 Neutron Resonances of Few-Body Type in the Crystalline Structures

We consider the model of neutron scattering on two fixed centers where the two-body scattering amplitudes have the resonant Breit-Wigner form:

$$t_i = |\nu_i\rangle \frac{\Gamma_i/2}{E - E_{R_i} + i\Gamma_i/2} \langle \nu_i| \quad (7)$$

The energy and width of the resonance are determined with real and imaginary parts of the resonance wave number:

$$E_{R_i} = (p_R^2 - p_I^2)/2m; \quad \Gamma_i = -2p_R p_I / m$$

We can assume that the form-factor ν_i is almost a constant value in a sufficiently wide range around the resonance point $E \approx E_{R_i}$. Note that the two-body scattering amplitude has the pole in the second sheet of complex plane of energy. Moreover, the resonant pole in the two-body system can give the series of poles for the three-body amplitude.

The neutron resonance in the ordered structure becomes the relatively stable state via the resonant re-scattering in the subsystems of two (or more) heavy nuclei. The resonant re-scattering appears and exists in a crystal at specific distances between nuclei and energies of neutron. Both these values depend on the inner property of the nuclei. These values can also be defined in an analytical form [18,19].

If the conditions are suitable for collective emission of high harmonic gammas, it means that nonlinear interactions between nuclei in the overdense crystal can stimulate these processes in deep layers of the neutron star envelopes.

It is very important to take into account the solutions of more complex objects, particularly the four-body systems that consist of three heavy nuclei and one neutron. The solutions of these four-body systems can give us the tendency of resonance influences in the cells of corresponding layers of the crusts. As in the previous case, the problem of neutron scattering on this subsystem can be solved in an analytical form. To simplify this, we can consider that all three nuclei are identical.

The resonant points can appear at larger distances between the nuclei than in the case of the three-body system above (see Fig. 1 and Fig. 2). The resonance picture in the neutron star envelopes can be more complicated and wealthy than in the frame of the two-body point of view.

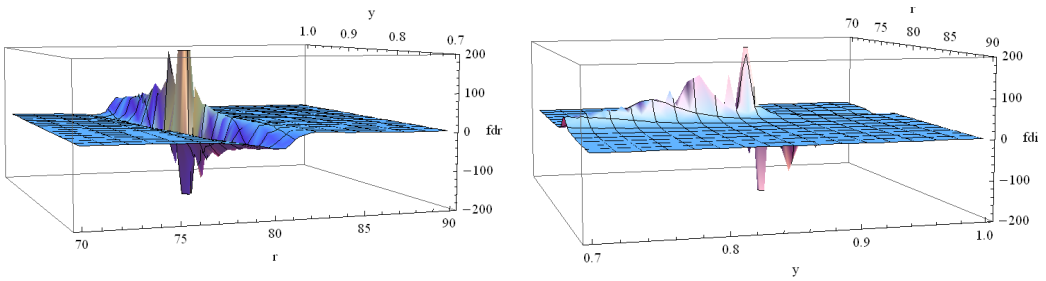

Figure 2 – Real and imaginary part of K in the case of (n + ^{55}Mn + ^{55}Mn) system

There are some difficulties in determination of the characteristics for neutron scattering on unstable neutron-excess nuclei. Firstly, it is the absence of data on neutron resonances for such nuclei. Secondly, it is the determination of nonlinear interactions and their manifestations that play important role at the lower layers of the neutron star envelopes. Therefore, in order to underline the role of the neutron resonances and related processes, we considered several simple examples of the neutron resonances with the iron group nuclei involved. These nuclei may not be preserved at considered depths, because they would be transformed in the electron capture reactions. Our aim is to show how the new processes can emerge in the deep layers of the neutron stars envelopes and how they can manifest themselves in the analysis of data, obtained by the external observer. Therefore, in order to underline the role of the neutron resonances and related processes, we considered several simple examples of the neutron resonances with the iron group nuclei involved. These nuclei may not be preserved at considered depths, because they would be transformed in the electron capture reactions. Our aim is to show how the new processes can emerge in the deep layers of the neutron stars envelopes and how they can manifest themselves in the analysis of data, obtained by the external observer.

Note that every neutron-nucleus resonance creates own structural resonance levels in the three-body system. Figure 2 and 3 demonstrate the behavior of the neutron amplitude for the re-scattering in the subsystem of two nuclei.

Our choice to consider the crystal structures with isotopes of the iron element is motivated by the fact that these elements are essential in the composition of the neutron star matter and, of course, for the neutron star envelopes. The calculations were carried out for the scattering channel, where every subsystem n + ^{55}Mn has the similar quantum numbers: the total moment J = 3 and the angular moment l = 0. The resonance levels were taken into account: E_{R0} = - 1.615 keV, and E_R = k_R^2 =1.098 keV with Γ = 18 eV [12]. Note that every neutron-nucleus resonance creates own structural resonance levels in the three-body system (see Fig 2 and 3).

One can see that the resonant distances between the nuclei become larger and the dispositions of the resonances are more complicated.

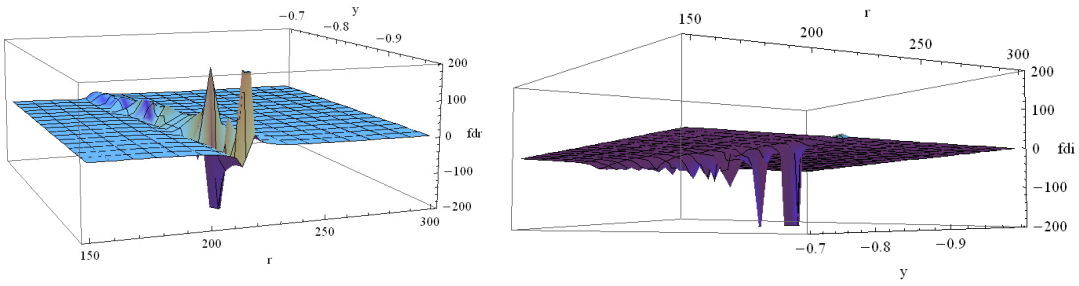

Figure 3 – Real and imaginary part of K in the case of (n + ^{57}Fe + ^{57}Fe)

The calculations demonstrate that the structural neutron resonances mostly appear in a wide energy area around the resonance energy of the neutron-nucleus resonance, and along the narrow trajectory in the space coordinate. Moreover, the two-body resonances with narrower widths produce the larger number of structural neutron resonances, some of them are more powerful and have very narrow peaks.

We also estimated the nuclear jitter effect in the crystal lattice. Fluctuations were considered to be small so far, but they may be considered with selecting an appropriate wave function describing the heavy nucleus state in the lattice node.

5 Conclusion

We consider the forced reverse reactions, which are acting in neutron star envelopes and stimulated by huge pressure that leads to the transformation of matter, closes some reactions of beta decay and neutron-rich of matter.

However, the remarkable distinctions have been also discovered. For example, the cardinal distinctions appear in the reactions and processes between nuclei of Fe group and the group of light elements.

The chemical composition of primordial matter of a neutron star determines the evolution of the

neutron star matter and peculiarities of nuclear reactions and processes. The neutron resonances of few-body type that arise in crystalline structure have the selected character and take place only in suitable layers that lead to local oscillations of density. The nonlinear interactions can result to reactions with gammas, which knockout alpha particles from the nuclei. Then the inner crust layers will be enriched with free neutrons and alpha particles also.

The detailed theoretical descriptions of such resonances were based on the few-body model and supported by sample calculations of the new three-body and four-body neutron resonances. The study of the these resonances is focused at scattering of neutrons on a subsystem of two or three isotopes with the distances between these isotopes is considered as a key parameter. It was shown that each nucleus has its own resonance states at corresponding unique energies and lattice parameters. The new neutron resonances are calculated in the energy range close to the conventional neutron-nucleus resonances. In overdense matter like we deal with in neutron stars, the influence of the new resonances would increase and become very important.

The research carried out in the framework of IPS 3106 / GF4 (2015-2017): "The study of nuclear reactions and processes in the stellar matter".

References

[1] Shapiro. Stuart L. and Saul A. Teukolsky. Black Holes. White Dwarfs. and Neutron Stars // New York: John Wiley and Sons. – 1983.

[2] Zeldovitch. Yakov. and Igor Novikov. Relativistic Astrophysics. V1: Stars and Relativity // New York: Dover Publications. – 1996.

[3] Haensel. Pawel. Potekhin. Alexander Y. and Dmitrii G. Yakovlev. Neutron Stars // New York: Springer. – 2007.

[4] Chamel. Nicolas. and Pawel Haensel. Physics of Neutron Star Crusts // Living Reviews in Relativity. – 2008. – Vol. 11. – P. 10.

[5] Kirzhnits. David A. On the internal structure of neutron stars // Journal of Experimental and Theoretical Physics. –1960. – Vol. 38. – P. 503–509.

[6] Volodin. Vladimir. and David A. Kirzhnits. Influence of crystal lattice on the nuclear properties of superdense matter // Journal of Experimental and Theoretical Physics Letter. – 1971. – Vol.13:450. – P. 52.

[7] Takibayev. N. Neutron Resonance States in Overdense Crystals // Few–Body Systems. – 2013. – Vol. 54:447. – P. 450.

[8] Takibayev. N. Kato. Kiyoshi. and D. Nasirova. Excited Nuclei in Neutron Star Crusts // Advanced Studies in Theoretical Physics. – 2013. – Vol. 7. – P. 151.

[9] Nucleus Ground State Parameters//Moscow State University. http://cdfe.sinp.msu.ru/

[10] Nuclear Wallet Cards. USA National Nuclear Data Center – NNDC. URL:http://www.nndc.bnl.gov/wallet/wccurrent.html.

[11] Ajzenberg–Selone. Fay. Energy levels of light nuclei A = 5–10 // Nuclear Physics A. – 1988. – Vol. 490:1. – P. 169.

[12] Mughabghab. Said F. Atlas of Neutron Resonances// London. New York: Elsevier. –2006.

[13] Ganeev. Rashid A. Higher harmonic generation for intense laser radiation in plasma created by a prepulse acting on the surface of a solid target // Physics–Uspekhi (Advances in Physical Sciences). – 2009. – Vol. 179:65. – P. 90.

[14] Seres. Enikoe. Seres. Jozsef. and Spielmann. Christian. X–ray absorption spectroscopy in keV range with laser generated high harmonic radiation// Applied Physics Letters. – 2006. – Vol. 89:181919. – P. 181927.

[15] Midorikawa. Katsumi. High–Order Harmonic Generation and Attosecond Science // Japanese Journal of Applied Physics. – 2011. – Vol. 50. – doi:10.1143/JJAP.50.090001.

[16] L'Huilljer. Anne. Schafer. Kenneth J.. and Kenneth C. Kulander. Theoretical aspects of intense field harmonic generation // Journal of Physics B: Atomic. Molecular and Optical Physics. – 1991. – Vol. 24. – P. 3315–3341. doi:10.1088/0953–4075/24/15/004.

[17] Schafer. Kenneth J.. and Kenneth C.. Kulander. High Harmonic Generation from Ultrafast Pump Lasers // Physical Review Letters. – 1997. – Vol. 78. – P. 638. doi:10.1103/physrevlett.78.638.

[18] Takibayev. N. Class of Model Problems in Three–Body Quantum Mechanics That Admit Exact Solutions // Physics of Atomic Nuclei. – 2008. – Vol. 71. – P. 460.

[19] Takibayev. N. Exact Analytical Solutions in Three–Body Problems and Model of Neutrino Generator // EPJ Web of Conferences. – 2010. – Vol. 3. – P. 05028. doi:10.1051/epjconf/20100305028.

UDC 53.02

Multipole structure of compact objects

Quevedo H.

Instituto de Ciencias Nucleares, Universidad Nacional Autónoma de México, AP 70543, México, DF 04510, Mexico
Dipartimento di Fisica and ICRA, Università di Roma "La Sapienza", I-00185 Roma, Italy
e-mail: quevedo@nucleares.unam.mx

We analyze the applications of general relativity in relativistic astrophysics in order to solve the problem of describing the geometric and physical properties of the interior and exterior gravitational and electromagnetic fields of compact objects. We focus on the interpretation of exact solutions of Einstein's equations in terms of their multipole moments structure. In view of the lack of physical interior solutions, we propose an alternative approach in which higher multipoles should be taken into account.

Key words: Exact solutions of Einstein equations, compact objects, multipole moments
PACS numbers: 04.20.Jb, 95.30.Sf

1 Introduction

Einstein's equations [1]

$$R_{\mu\nu} - \frac{1}{2} R g_{\mu\nu} = \kappa T_{\mu\nu} , \qquad (1)$$

relate the geometric structure of spacetime, which is given by the Einstein tensor $G_{\mu\nu} = R_{\mu\nu} - \frac{1}{2} R g_{\mu\nu}$, with the matter content of spacetime, which is given by the energy-momentum tensor $T_{\mu\nu}$. Moreover, the equivalence principle allows us to establish a relationship between the geometric structure of spacetime and the gravitational field. This implies that the curvature of spacetime, interpreted as four-dimensional differential Riemannian manifold, can be considered as a measure of the gravitational interaction. For instance, if the spacetime is flat, $R_{\mu\nu\lambda\tau} = 0$, the Einstein tensor vanishes, leading to the condition that the matter content of the spacetime vanishes too. The opposite is not true. If $T_{\mu\nu} = 0$, the Ricci tensor $R_{\mu\nu}$ and the curvature scalar R vanish as well, but the curvature tensor $R_{\mu\nu\lambda\tau}$ can be different from zero.

Einstein's general relativity is thus a theory of the gravitational interaction. As such, it should be able to describe all physical situations in which the gravitational field is involved. Consider, for instance, the case of astrophysical compact objects, i.e., objects that are small for their mass. In general, the class of astrophysical compact objects is often considered to contain collectively planet-like objects, white dwarfs, neutron stars, other exotic dense stars, and black holes. The problem of describing the gravitational field of compact objects can be split into two related problems, namely, the exterior and the interior field, each of them represented by a particular metric $g^{i}_{\mu\nu}$ and $g^{e}_{\mu\nu}$, respectively. The surface of the compact object represents the hypersurface at which the interior and the exterior fields must coincide. The exterior field corresponds to a vacuum spacetime $T_{\mu\nu} = 0$, for which Einstein's equations reduce to

$$R_{\mu\nu} = 0 , \qquad (2)$$

whereas for the interior field it is necessary to choose a particular energy-momentum tensor that would take into account all the physical properties of the internal structure of the compact object. A particularly simple choice is the perfect-fluid energy-momentum tensor [2]

$$T_{\mu\nu} = (\rho + p) u_{\mu} u_{\nu} - p g_{\mu\nu} , \qquad (3)$$

where ρ and p are the density and the pressure of the fluid, respectively, and u^{μ} is the 4-velocity. The case of fluids with anisotropic pressures is also used in the literature.

Most compact objects, however, are characterized by the presence of internal and external electromagnetic fields. This implies that in general we should consider the Einstein-Maxwell theory. In this case, the exterior field should be described by an

exterior metric which satisfies the electrovacuum equations

$$R_{\mu\nu} = \kappa\left(F_{\lambda\mu}F^{\lambda}_{\nu} - \frac{1}{4} g_{\mu\nu} F_{\lambda\tau}F^{\lambda\tau} \right), \quad F^{\mu\nu}_{\ \ ;\mu} = 0 , \qquad (4)$$

where $F_{\mu\nu}$ is the Faraday electromagnetic tensor. On the surface of the compact object, the exterior metric must be matched with the interior metric which satisfies the general equations

$$R_{\mu\nu} - \frac{1}{2} R g_{\mu\nu} = \kappa[(\rho + p)u_{\mu}u_{\nu} - p g_{\mu\nu}] + \\ + \kappa\left(F_{\lambda\mu}F^{\lambda}_{\nu} - \frac{1}{4} g_{\mu\nu} F_{\lambda\tau}F^{\lambda\tau} \right) , \qquad (5)$$

$$F^{\mu\nu}_{\ \ ;\mu} = 0 . \qquad (6)$$

In this work, we present a brief review of the main exact solutions of Einstein-Maxwell equations which can be used to describe the exterior and interior field of astrophysical compact objects. We interpret the solutions in terms of their multipole solutions. To this end, we use the Geroch-Hansen [5, 6] procedure which provides a relativistic and coordinate-invariant definition of multipole moments. According to this definition, any stationary, vacuum, asymptotically flat solution of Eistein's equations can be uniquely characterized by two sets of multipoles M_n and J_n ($n = 0.1, ...$), the first of which represents the field generated by the mass distribution whereas the second one is due to the rotation of the distribution. In the case of electrovacuum fields, two more sets E_n and H_n must be included, representing the electric and magnetic multipoles of the electromagnetic field, respectively. The concrete calculations necessary to find the explicit expressions of the multipole moments for particular solutions are not easy to be carried out. Some auxiliary procedures can be used which are based on particular representations of the solutions. Here, we will use the Ernst representation and the concrete formulas derived in [7, 8].

This paper is organized as follows. First, in Sec. 2, we present the general line element that can be used to investigate the structure of the exterior and interior field equations. In Sec. 3, we present the Kerr metric with its multipole structure and its generalizations which include the electric charge and higher multipole moments. In Sec. 4, we mention the main problems associated with the search for perfect-fluid interior solutions of Einstein and Einstein-Maxwell equations. We propose an alternative approach that implies the inclusion of the quadrupole as an additional degree of freedom. This could contribute to solve the general set of Einstein-Maxwell equations. Section 5 contains the conclusions. We use throughout the paper geometric units with $G = c = 1$.

2 Line element

It is very difficult to find physically relevant solutions of Einstein's equations. To simplify the resulting system of differential equations, one usually assumes that certain conditions are satisfied which follow from the physical properties of the system under consideration. In the case of compact objects, two assumptions are made, namely, stationarity and axial symmetry. The first condition means that the field does not depend explicitly on the time coordinate, say **t**. This is in accordance with our experience since the shape and rotation of isolated compact objects have not been observed to change over long periods of time. The second condition is also based on observations. Indeed, all compact objects observed in Nature are characterized by a particular rotation with respect to an axis located inside the object. The rotation axis determines a privileged direction with respect to which compact objects are usually symmetric. It is therefore physically meaningful to assume that the gravitational field and, consequently, the spacetime metric are stationary and axially symmetric. Under these conditions, one can show that the line element reduces to the Weyl-Papapetrou-Lewis form [2]

$$ds^2 = f(dt - \omega d\varphi)^2 - \\ - f^{-1}\left[e^{2\gamma}(d\rho^2 + dz^2) + \mu^2 d\varphi^2 \right] , \qquad (7)$$

where f, ω, μ, and γ are functions which depend on the spatial coordinates ρ and z only. Notice that the metric does not depend on the coordinates t and φ as a consequence of the stationarity and axial symmetry assumptions, respectively.

The corresponding field equations are, in general, a highly non-linear and complicated system of second-order partial differential equations. Several representations for the field equations are known in the literature [2, 3]. The particular form of the line element (7) is convenient for the analysis of the field equations structure. For instance, in the limiting case of static vacuum field ($\omega = 0$), the function f turns out

to satisfy a second-order linear differential equation, whereas all the non-linearities of Einstein's equations are contained in the metric function γ. In the case of electrovacuum spacetimes, the function μ turns out to satisfy a harmonic differential equation so that it can be chosen as $\mu = \rho$ to simplify the form of the remaining field equations. In the general case of interior perfect-fluid metrics with electromagnetic field, the functions f, ω and μ satisfy a system of three coupled, non-linear, second-order, partial differential equations and the function γ is determined by a set of two first-order differential equations which can be integrated by quadratures.

As we will see below, for the representation of particular exact solutions, however, the cylindrical-like coordinates of the line element (7) are not very convenient. In fact, the physical significance of particular solutions can be understood more easily by using spherical-like coordinates. Also, the motion of test particles in the gravitational field of compact objects have been analyzed mostly in spherical-like coordinates [4].

An additional condition must be imposed in order for a particular solution to describe the exterior field of compact objects, namely, asymptotic flatness. This is a physical condition, implying that far away from the gravitational and electromagnetic source the fields must vanish, which is equivalent to saying that the metric reduces to the flat Minkowski metric. All the solutions presented in this work satisfy this physical condition.

3 Exterior electrovacuum solutions

The first vacuum solution of Einstein's equation was obtained by Schwarzschild in 1916. In spherical-like coordinates, it can be expressed as

$$ds^2 = \left(1-\frac{2m}{r}\right)dt^2 - \frac{dr^2}{1-\frac{2m}{r}} - r^2(d\theta^2+\sin^2\theta d\varphi^2) \quad . \tag{8}$$

It represents the exterior field of a static spherically symmetric mass distribution. In this case, only one multipole moment is different from zero, namely, the monopole $M_0 = m$. This is due to the spherical symmetry and the lack of rotation and electromagnetic field. The complexity of the field equations for the general stationary case is so high that it took almost fifty years to take into account the rotation of the source in the Kerr metric [9]

$$ds^2 = \frac{(\Delta - a^2\sin^2\theta)}{\Sigma}dt^2 - \frac{2a\sin^2\theta(r^2+a^2-\Delta)}{\Sigma}dtd\varphi - \left[\frac{(r^2+a^2)^2-\Delta a^2\sin^2\theta}{\Sigma}\right]\sin^2\theta d\varphi^2 - \frac{\Sigma}{\Delta}dr^2 - \Sigma d\theta^2 \quad ,(9)$$

where

$$\Delta = r^2 - 2mr + a^2 \ , \quad \Sigma = r^2 + a^2\cos^2\theta \ . \tag{10}$$

The parameter α stands for the angular momentum per unit mass, J/m, as measured by a distant observer. This can also be seen at the level of the multipole moments which in this case can be expressed as[1]

$$\begin{aligned} M_{2k} &= (-1)^k ma^{2k} \ , \\ M_{2k+1} &= 0 \ , \quad J_{2k} = 0 \ , \\ J_{2k+1} &= (-1)^k ma^{2k+1} \ . \end{aligned} \tag{11}$$

Notice that the odd mass multipoles and the even angular-momentum multipoles vanish identically as a result of the additional symmetry of the Kerr solution with respect to the equatorial plane $\theta = \pi/2$.

The charged generalization of the Kerr metric is obtained by considering the electromagnetic vector potential as the 1-form

$$A = -\frac{Qr}{\Sigma}\left(dt - a\sin^2\theta d\varphi\right), \tag{12}$$

which depends on the charge Q and the specific angular momentum α. It then follows that the magnetic field is generated by the rotation of the charge distribution. To find the corresponding metric, it is necessary to solve the complete set of Einstein-Maxwell equations (4) simultaneously. The final expression for the solution turns out to be identical to (9) and the only difference is at the level of the function Δ, namely,

$$\Delta = r^2 - 2mr + a^2 + Q^2 \ . \tag{13}$$

The corresponding electromagnetic multipoles E_n and H_n turn out to proportional to M_n and J_n,

[1] Notice that the original Geroch-Hansen definition of multipole moments leads to expressions with the opposite sign in front of M_n so that, for instance, the total mass is negative, $M_0^{GH} = -m$. However, a conventional normalization of the multipoles can be performed so that a positive sign for the total mass is obtained. Weuseherethisconvention.

respectively, as a result of the non-linear gravitational interaction between the mass and the charge distribution.

According to the black hole uniqueness theorems [10], the charged Kerr solution is the most general electrovacuum solution that describes the gravitational and electromagnetic field of a black hole. This means that for a black hole all multipole moments must be given in terms of the mass (M_0= *m)*, the angular momentum (J_1= *J)*, and the electric charge ($E_0 = Q$). All the remaining higher multipoles must depend explicitly on only these three parameters. In the case of other astrophysical compact objects, like white dwarfs or neutron stars, the uniqueness theorems are not valid. This means that higher multipoles, like the mass quadrupole or the electric dipole, could play an important role in the description of the gravitational field.

To begin with, let us consider a static mass with a quadrupole deformation. There are several solutions in the literature that can be used to describe a mass with a quadrupole [11 – 16]. The common feature of most solutions is that they are given in terms of quite complicated analytical expressions. To our knowledge, the simplest solution for a mass with a quadrupole is the q – metric [16]

$$ds^2 = \left(1-\frac{2m}{r}\right)^{1+q} dt^2 - \left(1-\frac{2m}{r}\right)^{-q} \times \left[\left(1+\frac{m^2\sin^2\theta}{r^2-2mr}\right)^{-q(2+q)}\left(\frac{dr^2}{1-\frac{2m}{r}}+r^2 d\theta^2\right)+r^2\sin^2\theta d\varphi^2\right] \qquad (14)$$

which was originally found by Zipoy [17] and Voorhees [18] in prolate spheroidal coordinates. If the quadrupole parameter vanishes (q = 0), we recover the spherically symmetric Schwarzschild solution.

Static solutions with higher multipoles are also known. For instance, the most general Weyl solution in cylindrical-like coordinates (7) takes the form

$$\ln f = 2\sum_{n=0}^{\infty} \frac{a_n}{(\rho^2+z^2)^{\frac{n+1}{2}}} P_n(\cos\theta), \qquad \cos\theta = \frac{z}{\sqrt{\rho^2+z^2}}, \qquad (15)$$

where α_n (n = 0.1, ...) are arbitrary constants, and $P_n(\cos\theta)$ represents the Legendre polynomials of degree n. The expression for the metric function γ can be calculated by quadratures. Then,

$$\gamma = -\sum_{n,m=0}^{\infty} \frac{a_n a_m (n+1)(m+1)}{(n+m+2)(\rho^2+z^2)^{\frac{n+m+2}{2}}}\left(P_n P_m - P_{n+1}P_{m+1}\right). \qquad (16)$$

Although, in principle, the Weyl solution should contain all asymptotically flat static metrics, it is not very convenient for the investigation of the physical significance of the metrics. For instance, the Schwarzschild solution can be obtained by selecting the values of the parameters $a_n = a_n^S$ in such a way that the infinite sum

$$\sum_{n=0}^{\infty} \frac{a_n^S}{(\rho^2+z^2)^{\frac{n+1}{2}}} P_n(\cos\theta) = \frac{1}{2}\ln\left(1-\frac{2m}{r}\right) \qquad (17)$$

converges to the Schwarzschild value. An alternative representation which is more suitable for the physical analysis of the metrics is given in terms of prolate spheroidal coordinates

$$ds^2 = f dt^2 - \frac{m^2}{f}\left[e^{2\gamma}(x^2-y^2)\left(\frac{dx^2}{x^2-1}+\frac{dy^2}{1-y^2}\right)+(x^2-1)(1-y^2)d\varphi^2\right], \qquad (18)$$

where m is a constant. The general asymptotically flat vacuum solution can be written as [12, 19]

$$\ln f = 2\sum_{n=0}^{\infty}(-1)^{n+1} q_n P_n(y) Q_n(x), \quad q_n = const \qquad (19)$$

where $P_n(y)$ are the Legendre polynomials, and $Q_n(x)$ are the Legendre functions of second kind. The metric function γ is quite cumbersome and cannot be written in a compact form. The physical significance of the parameters q_n can be obtained by calculating the corresponding Geroch multipole moments. In this case, we have that

$$M_n = N_n + R_n\,, \quad N_n = (-1)^n \frac{n! m^{n+1}}{(2n+1)!!} q_n\,, \qquad (20)$$

where N_n represent the Newtonian multipole moments and R_n are relativistic corrections which must be calculated explicitly for each value of n. For instance, $R_0 = R_1 = R_2 = 0$, $R_3 = -\frac{2}{5} m^2 N_1$, $R_4 = -\frac{2}{7} m^2 N_2 - \frac{6}{7} m N_1^2$, etc. We conclude that the parameters q_n are the Newtonian multipoles, modulo a constant multiplicative factor, and determine also the relativistic corrections.

The Schwarzschild metric is a particular case of the general solution (19) with $q_0 = 1$ and $q_k = 0$ (k > 0), and can be written as

$$f = \frac{x-1}{x+1}\,, \quad \gamma = \frac{1}{2} \ln \frac{x^2-1}{x^2-y^2}\,. \qquad (21)$$

It reduces to the standard form in spherical-like coordinates after applying the coordinate transformation $x = r/m - 1$ and $y = \cos\theta$. Moreover, the q – metric corresponds to

$$f = \left(\frac{x-1}{x+1} \right)^{1+q}\,, \quad \gamma = \frac{1}{2}(1+q)^2 \ln \frac{x^2-1}{x^2-y^2}\,, \qquad (22)$$

for which the leading mass multipoles are

$$M_0 = (1+q)m\,, \quad M_2 = -\frac{m^3}{3} q(1+q)(2+q)\,. \qquad (23)$$

This shows that the parameter q determines the quadrupole, but it also affects the total mass of the object.

As for the stationary generalizations of the above static solutions, many of them have been obtained by using different solution generating techniques. For instance, the first generalization of the Kerr metric with an arbitrary mass quadrupole moment was obtained in [20]. Other stationary generalizations with quadrupole and higher moments were obtained in [21 – 25]. The general form of all these metrics does not allow to express them in a simple manner. All the metric that generalizes the stationary Kerr metric are expected to be equivalent at the level of the quadrupole moment, up to a redefinition of the parameters that determine the mass quadrupole.

This short review of electrovacuum solutions shows that the situation is not complicated when we limit ourselves to the case of a rotating charged mass. This is due to the uniqueness theorems according to which the charged Kerr metric can be used to described any black hole in general relativity. Once we pretend to take into account the effects of a mass quadrupole, the situation becomes more and more complicated due to the increasing number of exact solutions. As mentioned above, one expects that all these solutions are equivalent at the level of the quadrupole moment due to the deformation and the rotation of the source. We believe that other physical conditions should be imposed in order to establish the difference between all available exact solutions. Further work in this direction is necessary in order to determine the physical relevance of all the solutions available in the literature.

4 Interior solutions

In the previous section, it was shown that in principle it is possible to describe the exterior field of compact objects by using exact electrovacuum solutions of Einstein-Maxwell equations. Each exterior solution, however, should be matched at the surface of the compact object with a physically meaningful interior solution. Consider, for instance, the simplest exterior solution with a mass monopole, i.e., the exterior Schwarzschild solution. If we suppose a perfect-fluid model for the interior counterpart with constant energy density ($\rho = \rho_0 = const$) and no charge distribution ($F_{\mu\nu} = 0$), the resulting field equations can be integrated analytically, leading to the interior metric

$$ds^2 = \left[\frac{3}{2} f(R) - \frac{1}{2} f(r) \right]^2 dt^2 - \frac{dr^2}{f^2(r)} - r^2 (d\theta^2 + \sin^2\theta d\varphi^2) \qquad (24)$$

with

$$f(r) = \sqrt{1 - \frac{2mr^2}{R^3}}\,. \qquad (25)$$

Moreover, the pressure of the perfect fluid turns out to be a function of the radial coordinate r only

$$p = \rho_0 \frac{f(r) - f(R)}{3f(R) - f(r)}. \quad (26)$$

This solution satisfies the matching conditions at the surface of a sphere of radius R. From this point of view, it is a good candidate for describing the interior of a spherically symmetric mass distribution. From a physical point of view, however, this solution is not acceptable. Indeed, the assumption of constant inner density implies that the fluid is incompressible which leads to an infinite speed of sound. There are many other static perfect-fluid solutions (see [2] for a list of the most relevant solutions). Nevertheless, none of them has a meaningful physical significance. The generalizations that include charge distributions present similar problems.

In the case of rotating fields, the situation is similar. Einstein's field equations have no known and physically acceptable interior solution that could be matched to the exterior Kerr metric. In particular, there are no interior solutions that could represent objects like the Earth or other rigidly rotating astrophysical objects. This is a major problem in general relativity.

There exist some exact interior solutions of Einstein's equations with a perfect-fluid source equipped with an electromagnetic field [26] that satisfy all the energy conditions and are well-behaved in the entire spacetime. They are interpreted as describing the gravitational and electromagnetic fields of disk-halos. However, this kind of solutions cannot be matched with any known exterior solution.

One century after the discovery of the exterior Schwarzschild solution, we see that even the simplest case of an interior field with only mass monopole moment does not have a definite solution in general relativity. In view of this situation, it seems convenient to try new and different approaches. We propose the following idea. The charged Kerr metric describes the exterior field of black holes. Once a particle crosses the horizon of a black hole, according to classical general relativity, it undoubtedly must end at the singularity. This means that the interior of black hole is a singularity where the classical theory breaks down. Consequently, it is not possible to describe the interior field of a black hole by using only classical general relativity; instead, it should be a problem of quantum gravity. In fact, we know that a crucial test of any quantum gravity model must be the avoidance of the classical singularities. Consequently, the interior counterpart of the charged Kerr metric cannot be found by using Einstein's equations only.

Consider now classical compact objects, not including black holes. In the static vacuum case, we usually assume that they are described by the spherically symmetric Schwarzschild metric, the same which is used for black holes. This assumption should be changed. Indeed, it is hard to imagine in Nature a completely spherically symmetric compact object. Therefore, it is necessary to take into account the natural deviations from spherical symmetry. The simplest way to reach this end is to consider the contribution of an axially symmetric quadrupole moment. As we mentioned in the previous section, there are several exterior metrics which represent the gravitational field of mass with quadrupole. The search for the corresponding interior counterparts with quadrupole moment will certainly contribute to understand the difference between the exterior metrics. It could be, for instance, that each exterior metric corresponds to an interior metric with a particular physical structure. Also, if it turns out that an explicit exterior metric does not allow the existence of a reasonable interior counterpart, it should not be considered as physically relevant.

We already started a program in which the main goal is to find interior solutions with quadrupole. The starting point is the exterior q – metric presented in the previous section. To search for the corresponding interior metric, it is very important to choose a convenient line element because the structure of the field equations depends on its explicit form. In [27], we proposed the following line element

$$ds^2 = e^{2\psi}dt^2 - e^{-2\psi}[e^{2\gamma}\left(\frac{dr^2}{h} + d\theta^2\right) + \mu^2 d\varphi^2], \quad (27)$$

where $\psi = \psi(r,\theta)$, $\gamma = \gamma(r,\theta)$, $\mu = \mu(r,\theta)$, and $h = h(r)$. For a perfect-fluid source, the main field equations can be written as

$$\frac{\mu_{,rr}}{\mu} + \frac{\mu_{,\theta\theta}}{h\mu} + \frac{h_{,r}\mu_{,r}}{2h\mu} = \frac{16\pi}{h} p e^{2\gamma - 2\psi}, \quad (28)$$

$$\psi_{,rr} + \frac{\psi_{,\theta\theta}}{h} + \left(\frac{h_{,r}}{2h} + \frac{\mu_{,r}}{\mu}\right)\psi_{,r} + \frac{\mu_{,\theta}\psi_{,\theta}}{h\mu} = \frac{4\pi}{h}(3p + \rho)e^{2\gamma - 2\psi} \quad (29)$$

Moreover, the metric function γ is determined by two first-order differential equations that can be integrated once the remaining metric functions are known explicitly. This is an advantage of the above line element. An additional advantage is that the conservation of the energy-momentum tensor leads to two simple expressions

$$p_{,r} = -(\rho + p)\psi_{,r}\,, \quad p_{,\theta} = -(\rho + p)\psi_{,\theta}\,, \qquad (30)$$

which resemble the Tolman-Openheimer-Volkov relation of the spherically symmetric case [2]. This is particularly important when trying to perform the integration of the main field equations. It is still very difficult to solve the above system of differential equations. We therefore propose to use solution generation techniques. The first step in this direction was taken in [27] where a transformation was derived by means of which it is possible to generate interior solutions with quadrupole moment, starting from spherically symmetric interior solutions. The investigation of the resulting axially symmetric solutions with quadrupole is currently under investigation.

5 Conclusions

In this work, we presented a brief review of the problem of describing the gravitational and electromagnetic field of astrophysical compact objects by using the multipole structure of exact solutions of the Einstein-Maxwell equations. In the case of the exterior field, we presented the properties of the main solutions and its multipole moments. Using the black hole uniqueness theorems, we observe that the charged Kerr solution is the only metric which contains the mass monopole, the dipole angular momentum and the charge monopole. Once higher multipoles are taken into account, the uniqueness theorems are no more valid and several solutions are available in the literature. We mention the q – metric as the simplest solution with quadrupole moment. We showed that there exist general static solutions with an infinite number of parameters which determine the Newtonian and the relativistic Geroch-Hansen multipole moments. We mentioned that it is possible to find the corresponding stationary electrovacuum generalizations by using solution generating techniques. In this manner, one can say that the problem of describing the exterior field of astrophysical compact objects can be solved by using multipole moments.

In the case of interior solutions, the situation is completely different. Even the simplest case of perfect-fluid source with only mass monopole cannot be solved completely. A major problem, for instance, is that there is no known physically meaningful interior solution that could be matched with the exterior Kerr metric. We therefore propose an alternative approach. The interior counterpart of the charged Kerr solution cannot be found in classical general relativity because inside the horizon a curvature singularity exists which implies the break down of the classical theory. Quantum gravity should be used to investigate the internal structure of black holes. As for other compact objects, it is necessary to take into account the natural deviations from spherical symmetry by adding higher multipoles. In particular, we propose to use the exterior q – metric to search for an interior solution with quadrupole. Preliminary calculations show that it is possible to find interior solutions by using a particular transformation which allows one to generate interior axially symmetric solutions with quadrupole moment. This task is currently under investigation.

Acknowledgements

This work was supported by DGAPA-UNAM, Grant No. 113514, Conacyt-Mexico, Grant No. 166391, and MES-Kazakhstan, Grants No. 3098/GF4 and No. 3101/GF4.

References

[1] A. Einstein. Die Feldgleichungen der Gravitation. –Sitzungsberichte der Preussischen Akademie der Wissenschaften: Berlin. – 1915. – P. 844-847.

[2] H. Stephani, D. Kramer, M. A. H. Mac Callum, C. Hoenselaers, and E. Herlt. Exact Solutions of Einstein's Field Equations. – Cambridge University Press: Cambridge. UK. – 2003.

[3] H. Quevedo. Multipolar solutions, in Cosmology and Gravitatio // Proceedings of the XIVth Brazilian School of Cosmology and Gravitation, edited M. Novello

and S. E. Perez Bergliaffa. – Cambridge Scientific Publishers, 2011. – P. 83-97.

[4] D. Pugliese, H. Quevedo and R. Ruffini. Equatorial circular orbits of neutral test particles in the Kerr-Newman spacetime. Equatorial circular orbits of neutral test particles in the Kerr-Newman spacetime // Phys. Rev. D – 2013. – Vol. 88. – P. 024042.

[5] R. Geroch. Multipole moments. I. Flat space // J.Math. Phys. – 1970. – Vol. 11. – P. 1955-1960;Multipole moments. II. Curved space // J. Math. Phys. – 1970. – Vol. 11. – P. 2580-2588.

[6] R.O. Hansen. Multipole moments of stationary spacetimes // J. Math. Phys. – 1974. – Vol. 15. – P. 46-52.

[7] H. Quevedo. Multipole Moments in General Relativity -Static and Stationary Solutions // Fort. Phys. – 1990. – Vol. 38. – P. 733-840.

[8] H. Quevedo. Generating Solutions of the Einstein - Maxwell Equations with Prescribed Physical Properties // Phys. Rev. D. – 1992. – Vol. 45. – P. 1174-1177.

[9] R. P. Kerr. Gravitational field of a spinning mass as an example of algebraically special metrics // Phys. Rev. Lett. – 1963. – Vol. 11. – P. 237-238.

[10] M. Heusler. Black Hole Uniqueness Theorems. – Cambridge University Press: Cambridge, UK, 1996. – 264 p.

[11] H. Weyl. Zur Gravitationstheorie // Ann. Physik. – 1917. – Vol. 54. – P. 117-145.

[12] G. Erez and N. Rosen. The gravitational field of a particle possessing a quadrupole moment // Bull. Res. Counc. Israel. – 1959. – Vol.8F. – P. 47-50.

[13] A. Tomimatsu and H. Sato. New series of exact solutions for gravitational fields of spinning masses // Prog. Theor. Phys. – 1973. – Vol. 50. – P. 95-110.

[14] T.I. Gutsunaev, V.S. Manko. On the gravitational field of a mass possessing a multipole moment // Gen. Rel. Grav. – 1985. – Vol. 17. – P. 1025-1027.

[15] H. Quevedo. On the exterior gravitational field of a mass with a multipole moment // Gen. Rel. Grav. – 1987. – Vol. 19. – P. 1013 - 1023.

[16] H. Quevedo. Exterior and interior metrics with quadrupole moment // Gen. Rel. Grav. – 2011. – Vol. 43. – P. 1141-1152.

[17] D. M. Zipoy. Topology of some spheroidal metrics // J. Math. Phys. 1966. – Vol. 7. – P. 1137-1143.

[18] B. Voorhees. Static axially symmetric gravitational fields // Phys. Rev. D. – 1970. – Vol. 2. – P. 2119-2122.

[19] H. Quevedo. General static axisymmetric solution of Einstein's vacuum field equations in prolate spheroidal coordinates // Phys. Rev. D. – 1989. – Vol. 39. – P. 2904-2911.

[20] H. Quevedo and B. Mashhoon. Exterior gravitational field of a rotating deformed mass // Phys. Lett. A. – 1985. – Vol. 109. – P. 13-18.

[21] V.S.Manko and I.D. Novikov. Class // Quantum Grav. – 1992. – Vol. 9. – P. 2477.

[22] J. Castejon-Amenedo and V.S. Manko.On a stationary rotating mass with an arbitrary multipole structure // Class. Quantum Grav. – 1990. – Vol. 7. – P. 779-785.

[23] H. Quevedo and B. Mashhoon. Generalization of Kerr spacetime // Phys. Rev. D. 1991. – Vol. 43. – P. 3902-3906.

[24] V.S. Manko, E. Mielke, J.D. Sanabria. Exact solution for the exterior field of a rotating neutron star // Phys. Rev. D. – 2000. – Vol. 61. – P. 081501.

[25] L. Pachón, J.A. Rueda, J.D. Sanabria.Realistic exact solution for the exterior field of a rotating neutron star // Phys. Rev. D. 2006. – Vol. 73. – P. 104038.

[26] A. Gutiérrez-Piñeres, G. González and H. Quevedo.Conformastatic disk-haloes in Einstein-Maxwell gravity // Phys. Rev. D. – 2013. – Vol. 87. – P. 044010.

[27] H. Quevedo and S. Toktarbay. Generating static perfect-fluid solutions of Einstein's equations // J. Math. Phys. – 2015. – Vol. 56. – P. 052502.

UDC 539

Lightest Kaonic Nuclear Clusters

Kezerashvili R.Ya.[1,2], Tsiklauri Sh.M.[3*], Takibayev N.Zh.[4]

[1]*Physics Department, New York City College of Technology, The City University of New York,Brooklyn, NY 11201,USA*
[2]*The Graduate School and University Center, The City University of New York,New York, NY 10016, USA*
[3]*Borough of Manhattan Community College, The City University of New York,New York, NY 10007, USA*
[4]*Al-Farabi Kazakh National University, 480078, Almaty, Kazakhstan*
[*]*e-mail: rkezerashvili@citytech.cuny.edu*

We present our study of kaonic three-body $\bar{K}NN$, $\bar{K}NN$ and $KK\bar{K}$ and four-body $\bar{K}NNN$, and $\bar{K}\bar{K}NN$ clusters within the framework of a potential model using the method of hyperspherical functions in momentum representation. To perform a numerical calculations for the bound state energy of the light kaonic system, we use a set of different potentials for the nucleon-nucleon and $\bar{K}N$ interactions, as well as for the kaon-kaon interaction. The calculations show that a quasibound state energy is not sensitive to the NN interaction, and it shows very strong dependence on the $\bar{K}N$ potential. We also compare our results with those obtained using different theoretical approaches. The theoretical discrepancies in the binding energy and width for the lightest kaonic system related to the different NN and $\bar{K}N$ interactions are addressed.

Key words: three-kaonic cluster, four-body kaonic cluster, hyperspherical harmonics
PACS: 21.45.-v, 21.85.+d, 13.75.Jz

1 Introduction

Nowadays, the study of exotic nuclear systems involving a $\bar{K}$ is an important topic in hadron physics, because the existence of kaonic nuclear states is related to kaon condensation and to physics of the core of neutron stars that by today's understanding are built up from exotic matter: pion and kaon condensates and quark matter [1, 2]. Kaonic nuclei carry important information concerning the $\bar{K}$ nucleon interaction in the nuclear medium. This information is very important in understanding kaon properties at finite density and in determining of the constraints on kaon condensation in high-density matter. The latter will allow one to adjust the methods developed in condensed matter physics for exciton and excitonic polariton condensates (see, for example, [3, 4]) to study the kaon condensation. The best way to understand the many body kaonic nuclear system is to study the simplest two-, three- and four-body clusters: $\bar{K}N$, $\bar{K}NN$ and $\bar{K}NNN$, as well as double kaonic clusters, when one nucleon in the three- or four-body kaonic cluster is replaced by the K – meson. The light kaonic clusters $\bar{K}NN$ and $\bar{K}NNN$ represent three- and four-body systems and theoretically can be treated within the framework of a few-body physics approaches. In the recent past much efforts have been focused on the calculations of quasibound state energies and widths for three- and four-body kaonic clusters. A variety of methods have been used in configuration and momentum spaces, to obtain eigenvalues for energy and width of quasibound states using diverse sets of $\bar{K}N$ and NN interactions. These include but are not limited by variational method approaches [5-15], the method of Faddeev equations in momentum and configuration spaces [16-28], Faddeev-Yakubovsky equations [26] and the method of hyperspherical harmonics in configuration and momentum spaces [29-28]. However, the predicted values for the binding energy and the width are in considerable disagreement. For example, for the K^-_{pp} cluster the predicted values for the binding energy and the width are 9–95 MeV and 20–110 MeV, respectively.

On the experimental side, several experiments have been performed to search for the kaonic clusters using various nuclear reactions starting from the first measurement reported by the FINUDA collaboration for the K^-_{pp} cluster [31] and including the most recent reports of J-PARC E15 and J-PARC E27 collaborations [32, 33] and HADES collaboration [34]. Recent HADES collaboration partial wave

analysis of the reaction $pp \to pK^+\Lambda$ at 3.5 GeV to search for the K^-_{pp} bound state shows that at a confidence level 95% such a cluster cannot contribute more than 2–12% to the total cross section with a $pK^+\Lambda$ final state [34]. However, there are important reports of K^-_{pp} search experiments done by DISTO collaboration and J-PARC E27 collaboration. They reported some signal at 100 MeV below the K^- and two protons threshold, which may be related to the kaonic cluster K^-_{pp}. J-PARC E27 collaboration has observed a K^-_{pp} – like structure in the $d(\pi^+, K^+)$ reaction at 1.69 GeV/c, while Ref. [35] reports an indication of a deeply bound K^-_{pp} state in the $pp \to p\Lambda K^+$ reaction at 2.85 GeV. The situation is still controversial and the existence, for example, of the K^-_{pp} quasibound state has not been established yet. Thus, the theoretical and experimental study of composite systems of K – mesons and nucleons is still a challenging issue in nuclear physics.

Below we present a study of the lightest kaonic nuclear clusters using the method of hyperspherical functions. We focus on three- and four-body nonrelativistic calculations within the framework of a potential model for the three- and four-body kaonic clusters using the method of hyperspherical harmonics (HH) in momentum representation. Calculations for a binding energy and width of the kaonic three- and four-body system are performed using different NN potentials and kaon-nucleon interactions, as well as kaon-kaon interactions. Such approach allows one to understand the key role of the kaon-nucleon interaction and the importance of nucleon-nucleon interaction in the formation of quasibound states of the kaonic three- and four-body systems.

2 Theoretical formalism

The Hamiltonians of the three and four nonrelativistic particles for the $\bar{K}NN$ and $\bar{K}NNN$ systems, respectively, read as

$$H_3 = \hat{T}_3 + V_{N_1N_2} + V_{\bar{K}N_1} + V_{\bar{K}N_2}, \quad (1)$$

$$H_4 = \hat{T}_4 + \sum_{1\le i<j\le 3} V_{N_iN_j} + \sum_{i=1}^{3} V_{\bar{K}N_i}, \quad (2)$$

where $\hat{T}_3$ and $\hat{T}_4$ are the operators of the kinetic energy for three- and four-particle system, respectively, $V_{N_iN_j}$ is the nucleon-nucleon potential and $V_{\bar{K}N_i}$ is a pairwise effective antikaon interaction with the nucleon. The effective interactions of the $\bar{K}N$, KN, $\bar{K}\bar{K}$ and $K\bar{K}$ two-body subsystems are discussed in detail in Refs. [5, 6, 10, 14, 36 – 39]. Below, we use two effective $\bar{K}N$ interactions that were derived in different ways. The effective $\bar{K}N$ interactions can be derived phenomenologically or constructed using the chiral SU(3) effective field theory, which identifies the Tomozawa-Weinberg terms as the main contribution to the low-energy $\bar{K}N$ interaction [37]. The potential for the description of the $\bar{K}N$ interaction was derived in Refs. [5, 10] phenomenologically, using $\bar{K}N$ scattering and kaonic hydrogen data and reproducing the $\Lambda(1405)$ resonance as a K^-_{pp} bound state at 1405 MeV, and the decay width of $\Lambda(1405)$ is also taken into account in this potential. We refer to this as the Akaishi-Yamazaki (AY) potential. The AY potential is energy independent. The other $\bar{K}N$ interaction given in Ref. [36] was derived based on the chiral unitary approach for the s – wave scattering amplitude with strangeness $S = -1$, and reproduces the total cross sections for the elastic and inelastic K^-p scattering, threshold branching ratios, and the $\pi\Sigma$ mass spectrum associated with the $\Lambda(1405)$. Hereafter we refer to this energy-dependent potential for the parametrization [40] as the HW potential. Both potentials are constructed in the coordinate space, are local, and can be written in the one-range Gaussian form as

$$V_{\bar{K}N}(r) = \sum_{I=0,1} U^I \exp\left[-(r/b)^2\right] P^I_{\bar{K}N}, \quad (3)$$

where r is the distance between the kaon and the nucleon, b is the range parameter and $P^I_{\bar{K}N}$ is the isospin projection operator . The values of the potential depth $U^{I=0}$ and $U^{I=1}$ for eachinteraction are given in Refs. [10] and [36] and the range parameter is chosen to be $b = 0.66$ fm for the AY potential and $b = 0.47$ fm for the HW potential.

To describe the $V_{N_iN_j}$ nucleon-nucleon interaction, we use several different NN potentials: the realistic Argonne V14 (AV14) and V18 (AV18) [41, 42] potentials, the semi-realistic Malfliet and Tjon MT-I-III (MT) [43] potential, the Tamagaki G3RS potential [44], which we hereafter refer to as the T potential, and potential [45], which we refer to as the M potential. Therefore, the use of different NN

potentials and $\bar{K}N$ interactions allows one to perform a validity test for the lightest kaonic clusters against various NN and $\bar{K}N$ interactions.

The binding energies and the wave functions of the three and four nonrelativistic particle can be obtained by solving the Schrödinger equation with the Hamiltonians (1) and (2), respectively. In our approach we use the hyperspherical harmonics method that represents a technique of solution of the Schrödinger equation to find the bound and scattering states for a few body system. The main idea of this method is the expansion of the wave function of the corresponding nuclear system in terms ofhyperspherical harmonics that are the eigenfunctions of the angular part of the Laplace operator in the six-dimensional space (three-body problem) or in the nine-dimensional space (four-body problem). The details of this method can be found in the monographs [46, 47, 48]. In our calculations we use the HH method in momentum representation [49, 48]. One starts from the Schrödinger equation for the three or four particles with the Hamiltonians (1) and (2), respectively, and rewrites this equation in the integral form in the momentum representation using the set of the Jacobi momenta $\mathbf{q}_i$ in $3(N-1)$ – dimensional momentum space. These momenta are the trees of Jacobi coordinates for three- or four-particle system $\mathbf{q}_i = \sqrt{\frac{m_{12\ldots i}m_{i+1}}{m_{12\ldots i+1}}}\left(\frac{1}{m_{12\ldots i}}\sum_{j=1}^{i} m_j\mathbf{q}_j - \mathbf{q}_{i+1}\right)$, $i = 1, 2, \ldots, N-1$, where m_j and $\mathbf{q}_j$ are the particles masses and momentum vectors conjugated to the position vectors $\mathbf{r}_j$ respectively, $m_{12\ldots i} = \sum_{j=1}^{i} m_j$ and N is the number of particles. After that, one introduces the set of the hyperspherical coordinates in the momentum space given by the hyperradius $\varkappa^2 = \sum_{i=1}^{N-1} q_i^2$ and the set of angles $\Omega_\varkappa$, which define the direction of the vector $\varkappa$ in $3(N-1)$ – dimensional momentum space, as well as the symmetrized hyperspherical harmonics in momentum representation $\Phi_\mu^\lambda(\Omega_\varkappa, \sigma, \tau)$ that are written as a sum of products of spin and isospin functions and hyperspherical harmonics [50]. Above, for the sake of simplicity, we denoted by λ the totality of quantum numbers on which the N – body hyperspherical harmonics depend and the integer μ is the global momentum in the $3(N-1)$ – dimensional configuration space, which is the analog of angular momentum in case of $N-2$. The HH are the eigenfunctions of the angular part of the $3(N-1)$ – dimensional Laplace operator in configuration space with eigenvalue $L_N(L_N+1)$, where $L_N = \mu + 3(N-2)/2$ and they are expressible in terms of spherical harmonics and Jacobi polynomials [46, 47, 48]. By expanding the wave function of N bound particles in terms of the symmetrized hyperspherical harmonics in momentum space

$$\Psi(\varkappa, \Omega_\varkappa) = \varkappa^{-\frac{3N-4}{2}} \sum_{\mu,\lambda} u_\mu^\lambda(\varkappa)\Phi_\mu^\lambda(\Omega_\varkappa, \sigma, \tau), \qquad (4)$$

and substituting Eq. (4) into the corresponding integral Schrödinger equation in the momentum representation, one obtains a system of coupled integral equations for the hyperradial functions $u_\mu^\lambda(\varkappa)$ for the system of three or four particles. The detailed description of the formalism for the K^-pp cluster can be found in Ref. [28]. Here we expand the wave function of three bound particles in terms of the symmetrized hyperspherical harmonics $\Phi_\mu^{l_p l_q L}(\Omega_\varkappa, \sigma, \tau)$ in momentum representation: $\Psi(\mathbf{p}, \mathbf{q}) = \sum_{\mu l_p l_q} u_\mu^{l_p l_q L}(\varkappa)\Phi_\mu^{l_p l_q L}(\Omega_\varkappa, \sigma, \tau)$, where μ is the grand angular momentum, L is the total orbital momentum, l_p and l_q are the angular momenta corresponding to the Jacobi momenta p and q that are conjugated to the standard Jacobi coordinates for three particles, $\varkappa$ is the hyperradius in the six dimensional momentum space, and $\Omega_\varkappa$ is the set of fiveangles which define the direction of the vector $\varkappa$. The functions $\Phi_\mu^{l_p l_q L}(\Omega_\varkappa, \sigma, \tau)$ are written as a sum of products of spin and isospin functions and HH, using the Raynal-Révai coefficients [51]. For the system K^-pp the wave function is antisymmetrized with respect to two protons, while for the K^-K^-p system it is symmetrized with respect to two antikaons. For the hyperradial functions $u_\mu^{l_q l_p L}(\varkappa)$ we obtain the coupled integral equations. By solving the coupled integral equations one can find the hyperradial functions $u_\mu^{l_q l_p L}(\varkappa)$ for a given L and the binding energies for the K^-pp and K^-K^-p systems. For the system $\bar{K}NNN$ the wave function is antisymmetrized with respect to three nucleons, while for the K^-K^-pp system it is symmetrized with respect to two antikaons and antisymmetrized with respect to two protons. The hyperradial functions

$u_{\mu}^{\lambda}(\varkappa)$ for four-body systems can be found by solving the coupled integral equations and use them to construct the corresponding wave functions (4). To solve the coupled integral equations for the hyperradial functions $u_{\mu}^{\lambda}(\varkappa)$ for the system of three or four particles obtained from the corresponding Schrödinger equations, we include only the real part of the $\bar{K}N$ $K\bar{K}$ and $\bar{K}\bar{K}$ interactions, quite in the same way as the earlier variational studies [13, 14, 29]. Using the wave function, the width of the bound state can be evaluated in a perturbative way from the imaginary part of the $\bar{K}N$ interaction as $\Gamma = -2\left\langle \Psi \left| \mathrm{Im}\left(V_{\bar{K}N}(r_{12}) + V_{\bar{K}N}(r_{13}) \right) \right| \Psi \right\rangle$ for $K^{-}pp$ and $K^{-}K^{-}p$ clusters. As it is stated in review [52], as well as demonstrated in the recent calculations of the width for the $K^{-}pp$ system [54] using a coupled-channel complex scaling method with Feshbach projection, this is a reasonable approximation. For an approximate evaluation of the width the imaginary part of the complex potential has often been treated perturbatively in the early variational studies [13, 14, 29] and by many authors, see for example [8, 9, 12, 13, 14, 15, 29, 30, 39]. In the same way the width of the bound state for $KK\bar{K}$ system is evaluated from the imaginary part of the $\bar{K}K$ interactions as $\Gamma = -2\left\langle \Psi \left| \mathrm{Im}\left(V_{\bar{K}K}(r_{12}) + V_{\bar{K}K}(r_{23}) \right) \right| \Psi \right\rangle$ and the widths for the $\bar{K}NNN$ clusters are evaluated through the expression $\Gamma = -2\left\langle \Psi \left| \mathrm{Im} v_{\bar{K}N} \right| \Psi \right\rangle$, where $v_{\bar{K}N}$ sums over all pairwise $\bar{K}N$ interactions.

In calculations with the energy dependent HW potential we follow Ref. [14] and use a " corrected" energy dependent complex potential, where the strength for each channel is determined so as to reproduce the $\bar{K}N$ scattering amplitude predicted in Ref. [40] and is parametrized by polynomial in terms of the $\bar{K}N$ energy. Also, to determine the $\bar{K}N$ energy in the $K^{-}pp$ system, the authors of Ref. [14] examined two ansatz, "Type I" and "Type II", which are given as Eqs. (20) and (21) in Ref. [14], respectively. In the current study is employed the "Type II" ansatz.

In the following Section we present results for a single-channel calculation using effective $\bar{K}N$, $\bar{K}\bar{K}$ and $\bar{K}\bar{K}$ interactions.

3 Results of numerical calculations and discussion

3.1 $K^{-}pp$ cluster

Let's start with the results of our calculations of the $K^{-}pp$ cluster recently reported in Ref. [28]. Results of these calculations for the $K^{-}pp$ cluster are presented in Table 1. For the calculations of the binding energy and the width with the method of HH we use as input MT, T, and AV14 potentials for the NN interaction, while for the $\bar{K}N$ interaction we use the energy-dependent effective HW and the phenomenological AY potentials. Such an approach allowed us to examine how the $K^{-}pp$ cluster's structure depends on different choices of the $\bar{K}N$ interactions for the same NN potential, as well as to investigate its dependence on different choices of the NN interaction for the same $\bar{K}N$ interaction, and to understand the sensitivity of the system to the input interactions.The analysis of the calculations presented in Table 1 show that the AY potential as the $\bar{K}N$ interaction input falls into the 46-47 MeV range forthe binding energyof the $K^{-}pp$ cluster, while the chiral HW $\bar{K}N$ potential gives about 17-21 MeV for the binding energy. Thus, the values for the binding energy for the $K^{-}pp$ system obtained for the different NN potentials are in reasonable agreement, and the ground state energy is not very sensitive to the NN interaction. However, there is a very strong dependence on the antikaon-nucleon interaction. When we employ the effective energy-dependent chiral theory based HW potential for the $\bar{K}N$ interaction and different NN interactions, as inputs, we predict a weakly bound $K^{-}pp$ cluster. This is similar to Ref. [14], where the authors employed several versions of energy-dependent effective $\bar{K}N$ interactions derived from chiral SU(3) dynamics together with the realistic AV18 NN potential. Our calculations also confirm results reported in earlier studies [13, 21, 29] employing the same type of $\bar{K}N$ interaction. The energy of the bound state, as well as the width calculated for the AY potential are more than twice as big as those obtained for the energy-dependent chiral $\bar{K}N$ HW potential. Therefore, the highest binding energies are obtained for the phenomenological AY potential. Let's compare our results with those obtained with different variational approaches. Our result for the binding energy is in good agreement with the result from Ref. [10], where the binding energy for the $K^{-}pp$ cluster was calculated

by employing the AY potential as the $\bar{K}N$ interaction and T potential as the NN interaction. However, the decay width seems rather different among two studies: in the present study the width is 74.5 MeV, while that obtained in Ref. [10] is 61 MeV. This should be related to the different behavior of the waves functions obtained using the variational approach and the method of hyperspherical functions. Recently it was reported that "resonance and coupled-channel problem are key ingredients in the theoretical study of the K^-pp" [54]. Those authors employ a coupled-channel Complex Scaling Method combined with the Feshbach method since this approach can simultaneously treat these two ingredients. Interestingly enough, their calculations [54, 53] for the binding energy and width are consistent with our results obtained within the single channel potential model. The comparison of our calculations with results obtained using the HH method in configuration space [29] and differential Faddeev equations [28] also are in reasonable agreement. This is a good indication that the binding energy does not depend significantly on the method of calculation.

3.2 K^-K^-p cluster

Three-body problem with two mesons and one baryon have received considerable attention in the recent literature [38, 39, 55, 56]. The baryonic systems $\bar{K}\bar{K}N$ and $\bar{K}KN$ with two kaons were investigated in Refs. [38, 39, 57]. We study a possible bound state of the K^-K^-p cluster with $S = -2$, $I = 1/2$, $J^+ = 1/2^+$ using the effective s – wave AY and HW potentials assuming that this state is formed due to the strong K^-p attraction.

The strength of the $s-$wave $\bar{K}\bar{K}$ interaction for the isospin $I = 0$ is zero due to Bose statistics, and we consider a weak repulsion for the isospin $I = 1$ that reproduces the scattering lengths $a_{K^+K^+} = -0.14$ fm for the range parameter $b = 0.66$ fm (AY potential) and $b = 0.47$ fm (HW potential). The results of calculations for the binding energies for the K^-p and K^-K^-p, the bound K^-K^-p state without K^-K^- interaction, and the root-mean-square radius of the $\bar{K}$ distribution are presented in Table 2. For the AY potential, the K^-K^-p system is still bound even with a much stronger $\bar{K}\bar{K}$ repulsion, while for the HW potential there is the bound state with the energy 0.01 MeV relative to the K^-p + K^- threshold. Thus, although the $\bar{K}N$ with $I = 1$ is attractive, the attraction is not strong enough to overcome the $\bar{K}\bar{K}$ repulsion. For the width within the method of HH we obtain 58.6 MeV and 41.6 MeV with the AY and HW potentials, respectively. Our results for the binding energy of thesystem obtained by the method of HH are in reasonable agreement with calculations obtained using a variational method [39] and the Faddeev calculations [26].

Table 1 – The binding energy B and width Γ for the K^-pp system calculated in the framework of the method of HH in the momentum representation for different interactions. NN potentials: AV14 [41], MT [43] and T [44]. $\bar{K}N$ interactions: AY [10] and HW [36]. E_{K^-p} is two-body energy in the K^-pp cluster.

	AV14+AY	MT+AY	T+AY	AV14+HW	MT+HW	T+HW
B, Mev	46.2	46.5	46.3	17.2	20.5	20.6
Γ, MeV	66.7	84.3	74.5	44.3	48.1	49.5
E_{K-p}, Mev	29.9			10.9		

Table 2 – The bound state energies of K^-p (E_2) and K^-K^-p (B) systems, and the root-mean-square radius of thedistribution.is the binding energy measured from the two-body threshold

K^-K^-	K^-p	$< r^2 >^{1/2}, fm$	E_2, MeV	B, MeV	$\Delta E, MeV$
AY	AY	1.36	30.0	31.7	1.7
$V_{K^-K^-} = 0$	AY			35.3	5.3
HW	HW	1.96	11.42	11.43	0.01
$V_{K^-K^-} = 0$	HW			12.21	0.79

3.3 $KK\bar{K}$ system

Recently, there has been increased interest in few-body systems constituted by two or more kaons. Particularly noteworthy is the possibility of formation of the quasibound states in a $KK\bar{K}$ system. We study the $KK\bar{K}$ system using a nonrelativistic potential model in the framework of the method of HH in momentum representation and consider the $KK\bar{K}$ system as three interacting kaons. Once the two-body interactions for the $K\bar{K}$ and KK subsystems are determined one can determine the wave function of the $KK\bar{K}$ system by solving the Schrödinger equation for the Hamiltonian $H = \hat{T}_3 + V_{\bar{K}K}(r_{12}) + \quad + V_{KK}(r_{13}) + V_{\bar{K}K}(r_{23})$ where the potential energy is the sum of the effective $K\bar{K}$ and KK interactions that are the functions of the interparticle distances r_{ij}. For the description of the effective kaon-kaon interactions we use the local potentials from Refs. [39] and [38] that can be written in one-range Gaussian form (3). The set of values of the potential depth U_A^I for eachinteraction is given in Refs. [39, 38] and the range parameteris chosen to be the same forandinteractions. We choose two optimized values for the range parameter: b = 0.66 fm (set A) and b = 0.47 fm (set B). The strength of strongly attractive s – wave $K\bar{K}$ interactions was assumed to be the same for the isospin I = 0 and isospin I = 1, while the strength of the s – wave $K\bar{K}$ interaction for the isospin I = 0 is $U_{KK}^{I=0}$ due to Bose statistics and we consider a weak repulsion for the isospin I = 1. In Ref. [39] the $K\bar{K}$ interaction is derived under the assumption thatforms the quasibound states f_0 (980) and a_0 (980) in I = 0 and I = 1 channel, respectively, and it reproduces the masses and widths of these resonances. The strength of the repulsive KK interaction inwas fixed to reproduce a lattice QCD calculation [58] for the scattering length $a_{K^+K^+} = -0.14$ fm, and a weaker repulsion that corresponds to the scattering length $a_{K^+K^+} = -0.10$ fm. Results of calculations for the set of potentials A when the KK interaction reproduces the scattering lengths $a_{K^+K^+} = -0.14$ fm and $a_{K^+K^+} = -0.10$ fm are denoted as A1 and A2, respectively. Correspondingly, the set of potentials Bthat reproduces those different scattering lengths hereafter we refer as B1 and B2.

Table 3 – Results of calculations of different characteristics of the $KK\bar{K}$ system

	Fadeev[59]	A1[59]	A1	A2	B1	B2	Separable AMY [60] potential
Mass, Mev	1420	1467	1469.4	1468.2	1464.1	1463.8	1463.4
$\Gamma/_2$, MeV	25	55	42	41.1	48.4	49.1	–
B, Mev		21	18.6	19.8	23.9	24.2	24.6
$\sqrt{< r^2 >}$, Mev		1.6	1.72	1.65	1.61	1.56	1.52
KK distance, fm		2.8	3.2	2.92	2.72	2.70	2.68
$(KK) - \bar{K}$, fm		1.7	1.78	1.68	1.66	1.62	1.60
$K\bar{K}$ distance, fm		1.6	1.68	1.65	1.64	1.58	1.55
$(K\bar{K}) - \bar{K}$ distance, fm		2.6	2.9	2.86	2.55	2.50	2.47

The solution of a system of coupled integral equations for the hyperradial functions allows us to construct the wave functionΨ for the $KK\bar{K}$ system and to determine the binding energy B. A reasonable convergence for the ground state energy is reached for the grand angular momentum $\mu_{\max} = 10$ and we limit our considerations to this value. The results of our calculations for the binding energy and the width for the $KK\bar{K}$ system along with the results obtained with a coupled-channel approach based on the solution of the Faddeev equations in momentum representation and the variational method [59] are presented in Table 3. The total mass the $KK\bar{K}$ system ranges from 1463.4 to 1469.4 MeV when we consider the sameK meson mass $m_K = 496$ MeV as in Ref. [59]. The width falls within the 41 - 49 MeV range for all sets of theandinteractions. The quasibound state for the $KK\bar{K}$ with spin-parity0$^-$and

total isospin 1/2 is found to be below the three-kaon threshold. The comparison of our results with the results for the binding energy 21 MeV (the mass is 1467 MeV) and the width 110 MeV obtained with the variational method in Ref. [59] shows that while the binding energy found within the HH and variational calculations are close enough, the percent differences of the results for the width is less than 26%. A reason of this difference is related to the different behavior of the wave function of the $KK\bar{K}$ system obtained within the variational method and the method of HH. The wave function within the method of HH is obtained using the criterion of conversion of the binding energy with the accuracy about 0.2 MeV and consideration of the next terms with $\mu > 10$ in the expansions (4) only very slightly changes the binding energy. However, the width that is calculated using the perturbative approach more sensitive to the wave function and does not converge so fast as a binding energy. This leads to the different overlapping of the imaginary part of the $V_{\bar{K}K}(r)$ potential. The difference between the HH and Faddeev calculations [59] is understandable because in Ref. [59] thesystem is studied with a coupled-channel approach based on solving the Faddeev equations considering the $KK\bar{K}$, $K_{\pi\pi}$, and $K_{\pi\eta}$ channels and using as input two-body matrices that generate f_0 (980) and a_0 (980)resonances, while in the present calculations we use a single-channel three-body potential model. In addition our calculation is carried out in non-relativistic approach, whereas the Faddeev calculation is done in semi-relativistic approach using two-body amplitudes that are calculated by solving a relativistically covariant Bethe-Salpeter equation in a coupled-channel approach and using the on-shell factorization method. Such a difference could make large discrepancy in the obtained results.

We also perform calculations for the $KK\bar{K}$ system using s–wave two-body separable potentials with Yamaguchi form factors from Ref. [60] that also used in Faddeev and Faddeev-Yakubovsky calculations [26] for K^-K^-p theand K^-K^-pp kaonic clusters. The corresponding results are presented in the last column of Table 3 and are very close to the results obtained using the effective local kaon-kaon interactions for the set B. Thus, our calculations within three body nonrelativistic potential model predict a quasibound state for the $KK\bar{K}$ system with mass around 1460 MeV that can be associated with the K(1460) resonance. Our results support the conclusion obtained through the variational calculations that $K(1460)$ could be considered as a dynamically generated resonance.

3.4 $\bar{K}NNN$ clusters

Recently Faddeev-Yakubovsky calculations [26] were made for the four-particle K^-ppn and K^-K^-pp kaonic clusters, where the quasibound states were treated as bound states by employing real s–wave two-body separable potential models for the $\bar{K}\bar{K}$ and $\bar{K}$ the nucleon interactions as well as for theinteraction. Fully four-body nonrelativistic realistic calculations of $\bar{K}NNN$ and $\bar{K}\bar{K}NN$ quasibound states within the method of HH in configuration space, using realistic NNpotentials and subthreshold energy dependent chiral $\bar{K}N$ interactions, were presented in Ref. [29]. Giving that below we present the results of our calculations for the $\bar{K}NNN$ and $\bar{K}\bar{K}NN$ quasibound states in the framework of method of HH in momentum representation using AV18 [42] and M [45]potentials and AY and HW $\bar{K}N$ interactions as inputs. To find the binding energies with above mentioned set of potentials, we solve a system of coupled integral equations for the hyperradial functions $u_\mu^\lambda(\chi)$. In the calculations we limit our consideration with the value μ_{max} = 10 getting a reasonable convergence for the binding energy. In Table 4 we present our results for $\bar{K}NNN$ cluster that we compare with those obtained via different methods. The results of our calculations for the energy and the width show dependence on theNN potentials and on the $\bar{K}N$ interactions. However, this dependence is dramatically different: for the same $\bar{K}N$ interaction and different NN potentials the ground state energy and the width change by about 3-15 %, while for the sameNN potential and differentinteraction the energy changes by a factor of more than 3 and the width changes by more than twice.

Table 4 – The binding energyand widthfor thesystem calculated in the framework of the method of HH in the momentum representation for different interactions with results from Refs. [9], [26] and [29]. The parity includes the eigen parity of antikaon.

J^π	T		AV18+AY	M+AY	AV18+HW	M+HW	[29]	[26]	[9]
$K^-pnn\ \frac{1}{2}^{-1}$	0	B, Mev	92.1	97.9	28.6	28.9	29.3	69	110.3
		Γ, Mev	83.4	84.1	30.3	30.8	32.9		21.2
$K^-pnn\ \frac{1}{2}^{-1}$	1	B, Mev	64.6	66.7	17.2	18.7	18.5		
		Γ, Mev	74.2	80.4	27.1	31.4	31.0		
$K^-ppp\ \frac{1}{2}^{-1}$	1	B, Mev	101.9	107.6	25.8	28.1			96.7
		Γ, Mev	87.9	89.8	28.1	31.2			12.5

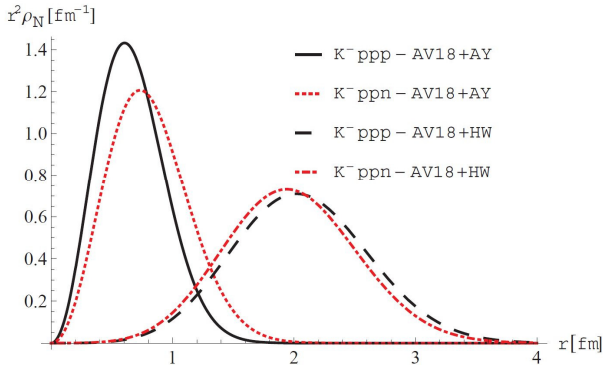

Figure 1 – Nucleon density distributions for and clusters

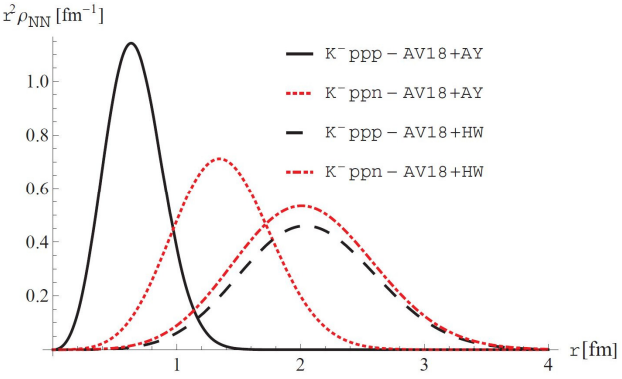

Figure 2 – Dependence of the two-nucleon density distributions in and clusters on the internucleon distance

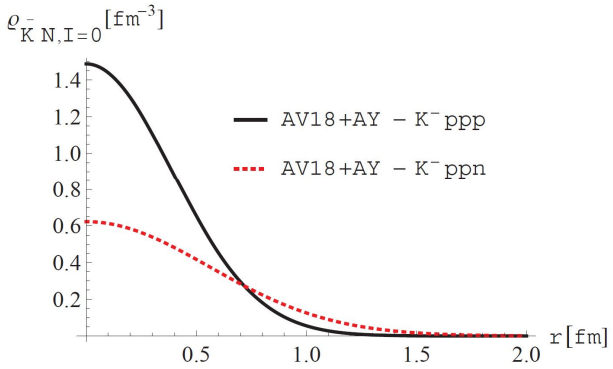

Figure 3 – Dependence of thedensity with isospininandclusters onrelative distance

For the comparison let's mention that the authors of Ref. [29] obtained 29.3 MeV and 32.9 MeV, and 18.5 MeV and 31.0 MeV for the binding energy and the width ofthe K^-ppn and K^-pnn clusters, respectively, while calculation within the Faddeev-Yakubovsky equations [26] with separable potential models for the $\bar{K}$ –nucleon and the nucleon-nucleon interactions leads to very deep ground state energyMeV forsystem. The comparison of our results for the K^-ppn and K^-pnn clusters obtained for AV18NN interaction and HW $\bar{K}N$ interaction with calculations [29] within the variational HH method for the AV14 NNinteraction and shallow chiral $\bar{K}N$ interaction shows a reasonable agreement. The predictions [9] for the binding energy and the width for the kaonic clusters studied

based on a framework of antisymmetrized molecular dynamics and employing adopted AY [5] potential as a bare $\bar{K}N$ interaction and the type of T [44] potential as a bare NNinteraction are presented in the last column of Table 4. In our calculations we use the same parametrization of the AY and HW potentials as in Section III A. As is seen from Table IV there is a reasonable agreement for the widths for the K^-ppn and K^-pnn clusters among the present study and study [29] in case of HW potential. However, the widths of the K^-ppn and K^-pnn systems are largely different among our study and an earlier study [9] in the case of AY potential. To understand these discrepancies and compare our results with Ref. [9], we performed the calculations for the $\bar{K}N$ interaction $V_{\bar{K}N}^{I=0}(r) = -(593 + i\omega_0)\exp[-(r/0.66)^2]$ and use for the imaginary part of the potential the different values of $\omega_0 = 20$, 40, 83 MeV, respectively [5, 9]. The results are the following: K^-ppp = (101.9, 19.8) MeV, (101.9, 38.7) MeV, (101.9, 87.9) MeV; $K^-ppn, (B,\Gamma)$ =(92.1, 18.7) MeV, (92.1, 37.4) MeV, (92.1, 83.4) MeV; $K^-pnn, (B,\Gamma)$ =(64.6, 16.3) MeV, (64.6, 32.6) MeV, (64.6, 74.2) MeV, that are in agreement with the corresponding calculations from Refs. [5, 9] that lead to narrow widths only for small values of ω_0 . If the binding energy is large and lies below the threshold of the main decay channel $\pi\sum$, as a result we have the width of the quasi-stable discrete bound state less than the binding energy and complex part of the $\bar{K}N$ potential should be small. The value $\omega_0 \sim 20$ MeV can reproduce the results of the width from Refs. [5, 6, 7, 8, 9]. In our approach we can reproduce the narrow width reported in Ref. [9] only for the small value of the the imaginary part of the AY potential. Interestingly enough, our calculations for the AY interaction indicate that for the system $\bar{K}NNN$ the cluster K^-ppp is more deeply bound K^-ppn than thethat contradicts to the results [9]. In a shell-model picture, one of three protons in the K^-ppp should be raised up to 0p orbit due to Pauli principle, while all nucleons in K^-ppn occupy the 0s orbit. So, the naïve expectation is that the K^-ppn is lower than the K^-ppp energetically. From the other side the larger number of the strongly attractive K^-p pairs in the $(\frac{3}{2}^+,1)$ state than in $(\frac{1}{2}^-,0)$ state may cause a lowering of theT=1 state, even below the T = 0, although the third proton in the T = 1 state should be flipped up to the orbital $(0p_{3/2})$. The final picture depends on the strength of $\bar{K}N$ interaction. The attractive AY interaction is much stronger than the effective HW interaction. The strength of $\bar{K}N$ interaction plays an important role that may lead to the nuclear compression. Following Ref. [61] we calculated a nucleon density distribution $\varsigma_N(r)$ averaged over angular dependence multiplied by r^2, wherer is the distance of the nucleon from the center of mass for K^-ppp, or K^-ppn clusters, shown in Fig. 1. For K^-ppp cluster one can observe a significant spatial shrinkage when the AY $\bar{K}N$ interaction is used. Since the $\bar{K}N$ potential is much more attractive in the I = 0 channel than in the I=1channel, different distribution of protons and neutrons is expected in kaonic clusters. Such results have already been reported in the early study within a new framework of the antisymmetrized molecular dynamics method in Refs. [8] and [9]. Probably in a $\bar{K}$ – nuclear system is preferable a structure where the proton distribution differs from the neutron distribution, such a structure dynamically produced in the hyperspherical function treatment. Particularly, the composition of the K^-ppp wave function within our formalism is the following:

$$[K^-pp(T=1/2,J=0)+p]^{3/2^+,1}, -93\%,$$
$$[K^-p(T=0,J=1/2)+pp]^{3/2^+,1}, -6.4\%,$$
$$[K^-+(ppp)(T=3/2,J=3/2)+p]^{3/2^+,1}, -0.6\%.$$

Our calculations show that the dominant contribution into the total wave function of the K^-ppp system is the $[K^-pp(T=1/2,J=0)+p]^{3/2^+,1}$ configuration. While the K^-p interaction is much stronger than the K^-n, the protons preferably allocate near the K^- and their kinetic energy increase. However, the total energy decreases due to the strongly attractive AY K^-p interaction. As a result the K^-ppp binding energy of thebecomes larger than that for the K^-ppn. In Table 5 are presented the kinetic energy per nucleon for a proton and a neutron in $\bar{K}NNN$, as well as the expectation value of the $\bar{K}N$ interaction. To estimate the expectation values of the kinetic energy and of the $\bar{K}N$ potential energy per nucleon the particle numbers are counted following Ref. [9] using Clebsch-Gordan coefficients. The particular numbers of protons and neutrons are 2.67 and 0.33, respectively, for K^-ppp and both are equal 1.5 for K^-ppn. Analysis of Table 5 and all above notes gives a possible explanation why the K^-ppp cluster is more deeply bound than the K^-ppn when the strongly attractive AY potential [10] is used, while

when the input is the HW potential we have an opposite picture. To reveal the characteristic structure of K^-ppp and enhancing the difference between the K^-ppp and K^-ppn clusters we calculate density distributions of the NN and $\bar{K}N$ pairs as functions of the respective nucleon-nucleon and antikaon-nucleon distances using Eq. (32) from Ref. [14]. In Fig. 2 is shown two-nucleon density distribution $\varsigma_{NN}(r)$ multiplied by r_2 in the K^-ppp and K^-ppn clusters for the AY and HW potentials. The two-nucleon distribution shows the pronounced maximum at the short-distances 0.63 fm and 1.34 fm for the K^-ppp and K^-ppn clusters, respectively, in the case of strong AY interaction. For relatively shallowly bound by the HW potential K^-ppp and K^-ppn clusters the maximum is pronounced at 2.02 fm and 2.05 fm, respectively, that reflects relatively weak binding of the systems. One can also understand a reason for the deeper binding of K^-ppp and K^-ppn thanin case of AY potential by analyzing thedensity distribution. Because the $\bar{K}N$ potential in isospin-zero channel plays a key role in the deep binding of $\bar{K}$ clusters, we calculate the projected density distributions for $\bar{K}N$ pairs with isospin $I = 0$ in the K^-ppp and K^-ppn clusters. The results of calculations of the normalized projected density $\varsigma_{\bar{K}N,I=0}(r)$ are shown in Fig. 3. As is seen in Fig. 3 the $\bar{K}N$ density distribution with isospin $I = 0$ has its maximum at zero distance between the antikaon and each nucleon that reflects the strong $\bar{K}N$ attraction in the $I = 0$ channel. The comparison of the $\bar{K}N$ density distribution shows that one is bigger for the K^-ppp cluster compare to that for the K^-ppn. From the projected density distributions for the $\bar{K}N$ pairs with isospin $I = 0$ configuration calculated mean-square distances $R_{\bar{K}N}$ are 1.45 fm and 2.04 fm for the K^-ppp and K^-ppn clusters, respectively. The later facts reflect relatively strong binding of the K^-ppp system. Thus, the K^-ppp is compacter than the K^-ppn cluster.

Based on the results of our calculations, we can conclude that the pairwise $\bar{K}N$ interaction plays a major role in the formation of the kaonic bound state and the effective $\bar{K}N$ interaction based on chiral SU(3) dynamics [36] leads to a relatively modest binding for the K^-ppm, K^-pmm and K^-ppp clusters. Our results confirm the calculations [29].

Table 5 – Nucleon energy inandclusters. Expectation values of the kinetic energyand of theinteraction per nucleon calculated in the framework of the method of HH in the momentum representation for the AY and AV18 interactions

		$< T >$MeV/N	$< \bar{K}N >$ MeV/N
K^-ppp	Proton	78.1	-195.2
	Neutron	49.3	-29.1
K^-ppn	Proton	72.4	160
	Neutron	55	38.2

$\bar{K}\bar{K}NN$ cluster

A decade ago in Ref. [7] a deeply bound double K^-K^-pp cluster was predicted to be deeply bound with binding energy of 117 MeV and width 35 MeV. Barnea, Gal and Liverts [29] perform a variational HH calculation in configuration space for the K^-K^-pp system based on the shallow chiral $\bar{K}N$ interaction model with the self-consistent energy dependence taken into account and obtained very shallow bound states with a binding energy that is substantially smaller than earlier prediction [7]. When in our calculation the HW potential is used the similar result to the early study [29] is obtained. In our calculations with the AY interaction, as in Section III D, we employ the potential $V_{\bar{K}N}^{I=0}(r) = -(593 + i\omega_0)\exp[-(r/0.66)^2]$ using for the imaginary part of the potential the values ω_0 = 20, 40, 83 MeV, respectively. In Table VI are presented results when ω_0 = 83 MeV. The corresponding values for the width are 72.4 MeV and 73.7 MeV for AV18 and M potentials, respectively, that are close enough to the widths obtained using the HW interaction. However, the binding energy is almost three times bigger. When $\omega_0 = 20$MeV and 40 MeV, respectively, Γ = 17.9 MeV and Γ = 35.8 MeV for the AV18 potential, and Γ = 18.5 MeV and Γ = 37.1 MeV for M potential. Thus, our results with the AY $\bar{K}N$ interaction are close to the earlier prediction [7] when ω_0 = 40 MeV and the binding energy is in a reasonable agreement with recent Faddeev-Yakubovsky calculations [26].

Table 6 – The binding energyand widthfor thesystem calculated in the framework of the method of HH in the momentum representation for different interactions with results from Refs. [7], [26] and [29].

		AV18+AY	M+AY	AV18+HW	M+HW	[29]	[26]	[7]
K^-K^-pp	B, Mev	91.6	92.7	31.5	31.9	32.1	93	117
	Γ, Mev	72.4	73.7	78.1	79.2	80.5		35

4 Conclusions

Within the framework of a potential model for the kaonic clusters K^-pp, K^-K^-p, $KK\bar{K}$, $\bar{K}NNN$, and K^-K^-pp we perform nonrelativistic three- and four-body calculations using the method of hyperspherical harmonics in the momentum representation. We examine how the binding energy and width of the K^-pp cluster depends on different choices of the $\bar{K}N$ and NN interactions. Our consideration includes the realistic Argonne V14 [41], the semi-realistic MT [43] and T [44] potentials as inputs for the NN interaction and we employ the phenomenological AY potential and HW potential constructed based on chiral SU(3) dynamics, as inputs for the $\bar{K}N$ interaction. For all types of considered NN interactions, our calculations predict deeply bound states for the AY $\bar{K}N$ interaction and a relatively shallowly boundcluster for the effective chiralinteraction. Moreover, the K^-pp cluster is the most strongly quasibound three-body system. The results of our calculations show that the binding energy of the K^-pp system depends entirely on the ansatz for the $\bar{K}N$ interaction and substantially changes when we use the AY and HW $\bar{K}N$ interaction. In regard to the sensitivity of the binding energy to the details of the NN potentials, Ref. [14] found that when the K^-pp system is weakly or deeply bound, the dependence on different types of NN interactions is weak. In fact, our study confirms this conclusion using in calculations Argonne V14 [41], the semi-realistic MT [43] and T [44] NN potentials.

The strong AY $\bar{K}N$ interaction is responsible for the formation of the K^-K^-p system and this cluster is still bound even with a much stronger $K\bar{K}$ repulsion, while the HW potential leads to the bound state with energy of only 0.01 MeV relative to the $K^-p + K^-$ threshold. The mass (binding energy) of the $KK\bar{K}$ system slightly depends on the sets of parameters that determine $K\bar{K}$ and KK interactions and the width falls into the 41-49 MeV range for all sets of these parameters. There is reasonable agreement between these results, the mass obtained using separable AMY interactions [60] and the variational calculation [59]. Our results for the $KK\bar{K}$ system support the conclusion that K (1460) could be considered as a dynamically generated resonance.

Based on the results of our calculations for four-particle kaonic systems we also can conclude that the pairwise $\bar{K}N$ interaction plays a major role in the formation of the kaonic bound state and the effective chiral $\bar{K}N$ interaction gives relatively modest binding for the K^-ppm, K^-ppp and K^-K^-pp clusters.

All our calculations with the effective chiral $\bar{K}N$ interaction show that the width is always larger than the bindingenergy. In some cases the width is more than twice as large as the binding energy. Only for some four-particle kaonic clusters when the input for the $\bar{K}N$ interaction is the AY potential, the binding energy is larger than the width. As a consequence, perhaps, we are facing a situation where it is hard to identify the resonances which would make the experimental observation challenging.

Acknowledgements

This work is supported by the MES Republic of Kazakhstan, the research project IPS 3106/GF4 and the National Science Foundation grant Supplement to the NSF grant HRD-1345219.

References

[1] G.E. Brown. M. Rho. Chiral restoration in hot and/or dense matter // Phys. Rep. – 1996. – Vol. 269. – P.333.

[2] C.H. Lee. Kaon condensation in dense stellar matter// Phys. Rep. – 1996. – Vol. 275. – P. 255.

[3] O.L. Berman. R.Ya. Kezerashvili. G.V. Kolmakov. and Yu.E. Lozovik. Turbulence in a Bose-Einstein condensate of dipolar excitons in coupled quantum wells // Phys. Rev. B. – 2012. – Vol. 86. – P.045108.

[4] O. L. Berman. R. Ya. Kezerashvili. K. Ziegler. Superfluidity and collective properties of excitonicpolaritons in gapped graphene in a microcavity // Phys. Rev. B. – 2012. – Vol.86. – P. 235404.

[5] Y. Akaishi and T. Yamazaki.Nuclear K^- bound states in light nuclei // Phys. Rev. C. – 2002. – Vol. 65. – P.044005.

[6] T. Yamazaki and Y. Akaishi. (K^-,π^-) production of nuclear $\bar{K}$ bound states in proton-rich systems via $\Lambda*$ doorways // Phys. Lett. B. – 2002. – Vol. 535. – P. 70.

[7] T. Yamazaki. A. Doté. and Y. Akaishi. Invariant-mass spectroscopy for condensed single- and double-$\bar{K}$ nuclear clusters to be formed as residues in relativistic heavy-ion collisions // Phys. Lett. B. – 2004. – Vol. 587. – P. 167.

[8] A. Doté. H. Horiuchi. Y. Akaishi. and T. Yamazaki. Invariant-mass spectroscopy for condensed single- and double-$\bar{K}$ nuclear clusters to be formed as residues in relativistic heavy-ion collisions // Phys. Lett. B. – 2004. – Vol. 590. – P. 51.

[9] A. Doté. H. Horiuchi. Y. Akaishi. and T. Yamazaki. Kaonic nuclei studied based on a new framework of antisymmetrized molecular dynamic // Phys. Rev. C. – 2004. – Vol. 70. – P. 044313.

[10] T. Yamazaki and Y. Akaishi. Basic K- nuclear cluster, K^-pp, and its enhanced formation in the $p+p\rightarrow K^+X$ reaction // Phys. Rev. C. – 2007. – Vol. 76. – P. 045201.

[11] A. Doté. H. Horiuchi. Y. Akaishi. and T. Yamazaki.The Study of Deeply Bound Kaonic Nuclei with Antisymmetrized Molecular Dynamics// Prog. Theor. Phys. Suppl. – 2002. – Vol. 146. – P. 508.

[12] A. Doté and W. Weise.Study of Light Kaonic Nuclei with a Chiral SU(3)-Based KN Interaction // Prog. Theor. Phys. Suppl. – 2007. – Vol. 168. – P. 593.

[13] A. Doté. T. Hyodo. and W. Weise. K^-pp system with chiral SU(3) effective interaction // Nucl. Phys. A 804. – 2008. – Vol. – P. 197.

[14] A. Doté. T. Hyodo. and W. Weise. Variational calculation of the ppK$^-$ system based on chiral SU(3) dynamics // Phys. Rev. C. – 2009. – Vol. 79. – P. 014003.

[15] S. Wycech and A. M. Green. Variational calculations for K-–few-nucleon systems // Phys. Rev. C. – 2009. – Vol. 79. – P. 014001.

[16] N. V. Shevchenko. A. Gal. J. Mareš. Faddeev Calculation of a K^-pp Quasibound State // Phys. Rev. Lett. – 2007. – Vol. 98. – P. 082301.

[17] N. V. Shevchenko. A. Gal. and J. Mareš. and J. Révai. K–NN quasibound state and the K–N interaction: Coupled-channels Faddeev calculations of the K–NN–$\pi\Sigma$N system // Phys. Rev. C. – 2007. – Vol. 76. – P.044004.

[18] Y. Ikeda and T. Sato. Strange dibaryon resonance in the K–NN-πYN system // Phys. Rev. C. – 2007. – Vol. 76. – P. 035203.

[19] Y. Ikeda and T. Sato. Resonance energy of the K–NN$-\pi$YN system // Phys. Rev. C. – 2009. – Vol. 79. – P. 035201.

[20] A. Martnez Torres. K. P. Khemchandani. and E. Oset. Solution to Faddeev equations with two-body experimental amplitudes as input and application to JP=1/2+, S=0 baryon resonances // Phys. Rev. C. – 2009. – Vol. 79. – P. 065207.

[21] Y. Ikeda. H. Kamano. and T. Sato. Energy Dependence of $\bar{K}$N Interactions and Resonance Pole of Strange Dibaryons // Prog. Theor. Phys. – 2010. – Vol. 124. – P. 533.

[22] M. Bayar. J. Yamagata-Sekihara. and E. Oset. K–NN system with chiral dynamics // Phys. Rev. C. – 2011. – Vol. 84. – P. 015209.

[23] E. Oset. D. Jido. T. Sekihara. A. Martnez Torres. K.P. Khemchandani. M. Bayar and J. Yamagata-Sekihara. A new perspective on the Faddeev equations and the system from chiral dynamics and unitarity in coupledK–NN channels // Nucl. Phys. A. – 2012. – Vol. 881. – P. 127.

[24] M. Bayar and E. Oset. Improved fixed center approximation of the Faddeev equations for the the K–NN system with S=0 // Nucl. Phys. A. – 2012. – Vol. 883. – P.57.

[25] M. Bayar and E. Oset. The K–NN system revisited including absorption // Nucl. Phys. A. – 2013. – Vol. 914. – P. 349.

[26] . S. Maeda. Y. Akaishi. and T. Yamazaki.Strong binding and shrinkage of single and double K nuclear systems (K^-pp, K^-ppn, K^-K^-p and K^-K^-pp) predicted by Faddeev-Yakubovsky calculations // Proc. Jpn. Acad. Ser. B. – 2013. – Vol. 89. – P. 418.

[27] J. Révai and N. V. Shevchenko. Faddeev calculations of the K^-NN system with a chirally motivated K^-N interaction. II. The K^-pp quasibound state // Phys. Rev. C. – 2014. – Vol. 90. – P. 034004.

[28] R.Ya. Kezerashvili. Sh.M. Tsiklauri. I.N. Filikhin. V. M. Suslov. and B. Vlahovic.Benchmark for a quasi-bound state of the K^-ppsystem // arXiv. – 2015.– P.1508.07638 [nucl-th].

[29] N. Barnea. A. Gal. and E. Z. Liverts. Three-body calculations for the K^-pp system within potential models // Phys. Lett. B. – 2012. – Vol. 712. – P. 132.

[30] . R. Ya. Kezerashvili and Sh. M. Tsiklauri. Investigation of the structure of the few body kaonic nuclei using the method of hyperspherical functions in momentum space // EPJ Web Conf. – 2014. – Vol. 81. – P.02022.

[31] M. Agnello. G. Beer. L. Benussi et al.Evidence for a Kaon-Bound State K−pp Produced in K− Absorption Reactions at Rest // Phys. Rev. Lett. – 2005. – Vol. 94. – P.212303.

[32] -PARC E15 Collaboration: T. Hashimoto. S. Ajimura. G. Beer. et al. Search for the deeply bound K–pp state from the semi-inclusive forward-neutron spectrum in the in-flight K– reaction on helium-3 // Prog. Theor. Exp. Phys. – 2015. – P. 061D01.

[33] J-PARC E27 Collaboration: Y. Ichikawa. et al. Experiment to Search for a Nuclear Kaon Bound State K−pp // Prog. Theor. Exp. Phys. – 2014. – P. 101D03; Y. Ichikawa. et al. Observation of the “K− pp”-like structure in the d(π+, K+) reaction at 1.69 GeV/c // Prog. Theor. Exp. Phys. – 2015. – P. 021D01.

[34] HADES Collaboration: G. Agakishiev. et al. Partial Wave Analysis of the Reaction p(3.5GeV)+p->pK+Λ to Search for the "ppK−" Bound State // Phys. Lett. B. – 2015. – Vol. 742. – P. 242.

[35] T. Yamazaki. et al. Indication of a Deeply Bound and Compact K−pp State Formed in the pp→pΛK+ Reaction at 2.85 GeV // Phys. Rev. Lett. – 2010. – Vol.104. – P. 132502.

[36] T. Hyodoand W. Weise. Effective K−N interaction based on chiral SU(3) dynamics // Phys. Rev. C. – 2008. – Vol. 77. – P. 035204.

[37] W. Weise. Antikaon Interactions with Nucleons and Nuclei // Nucl. Phys. A. – 2010. – Vol. 835. – P. 51.

[38] D. Jido and Y. Kanada-Enyo. KK-N molecule state with I=1/2 and JP=1/2+ studied with a three-body calculation // Phys. Rev C. – 2008. – Vol. 78. – P. 035203.

[39] Y. Kanada-Enyo. and D. Jido. K-K-N molecular state in a three-body calculation // Phys. Rev. C. – 2008. – Vol. 78. – P. 025212.

[40] T. Hyodo. S. I. Nam. D. Jido. and A. Hosaka. Flavor SU(3) breaking effects in the chiral unitary model for meson-baryon scatterings // Phys. Rev. C. – 2003. – Vol.68. – P. 018201; Detailed Analysis of the Chiral Unitary Model for Meson-BaryonScattering with Flavor SU(3) Breaking Effects // Prog. Theor. Phys. – 2004. – Vol. 112.– P.73-97.

[41] R.B. Wiringa. R. A. Smith. and T.L. Ainsworth. Nucleon-nucleon potentials with and without Δ(1232) degrees of freedom // Phys. Rev. C. – 1984. – Vol. 29. – P.1207.

[42] R. B. Wiringa. V. G. J. Stoks. and R. Schiavilla. Accurate nucleon-nucleon potential with charge-independence breaking // Phys. Rev. C. – 1995. – Vol. 51. – P. 38.

[43] R. A. Malfliet and J. A. Tjon. Solution of the Faddeev equations for the triton problem using local two-particle interactions // Nucl. Phys. A. – 1969. – Vol.127. – P. 161.

[44] R. Tamagaki. Superfluid State in Neutron Star Matter. IGeneralizedBogoliubov Transformation and Existence of 3P2 Gap at High Density // Prog. Theor. Phys. – 1970. – Vol. 44. – P. 905.

[45] D. R. Thompson. M. LeMere. Y. C. Tang. Systematic investigation of scattering problems with the resonating-group method // Nucl. Phys. A. – 1977. – Vol.286. – P. 53.

[46] R. I. Jibuti and N. B. Krupennikova. Method of hyperspherical functions for few-body systems. (in Russian) Metsniereba. Tbilisi.– 1984.

[47] J. Avery. Hyperspherical Harmonics. Kluwer Academic. Dordrecht.– 1989.

[48] R. I. Jibuti. K. V. Shitikova. Method of hyperspherical functions in atomic and nuclear physics. (in Russian) Energoatomizdat. Moscow.– 1993.

[49] R. I. Jibuti. N. B. Krupennikova. V. Yu. Tomchinsky. Hyperspherical basis for the continuum spectrum// Nucl. Phys. A. – 1977. – Vol. 276. – P. 421.

[50] R. I. Jibuti. R. Ya. Kezerashvili. Double-charge-exchange reactions of π-mesons on three- and four-particle nuclei // Nucl. Phys. A. – 1985. – Vol.437. – P. 687.

[51] J. Raynal and J. Révai.Transformation coefficients in the hyperspherical approach to the three-body problem // NuovoCimento. – 1970. – Vol.68A. – P. 612.

[52] A. Gal. Recent studies of kaonic atoms and nuclear clusters // Nucl. Phys. A. – 2013. – Vol.914. – P.270.

[53] A. Doté. T. Inoue. and T. Myo.Application of a coupled-channel complex scaling method with Feshbach projection to the K–pp system // Prog. Theor. Exp. Phys.– 2015.– P. 043D02.

[54] A. Doté. T. Inoue. and T. Myo.Essential bar K cluster "K?pp" studied with a coupled-channel Complex Scaling Method + Feshbach method // J. Phys: Conf. Ser. – 2014. – Vol. 569. – P. 012084.

[55] A. Martnez Torres. K. – P.Khemchandani. and E. Oset // Phys. Rev. C. – 2009. – Vol. 79. – P. 065207.

[56] A. Martnez Torres. K. – P.Khemchandani. D. Jido. Y. Kanada-Enyo. and E. Oset // Nucl. Phys. A. – 2013. – Vol. 914. – P. 280.

[57] A. Martnez Torres and D. Jido. Solution to Faddeev equations with two-body experimental amplitudes as input and application to JP=1/2+, S=0 baryon resonance // Phys. Rev. C. – 2010. – Vol. 82. – P.038202.

[58] S. R. Beane. et al.K+K+ scattering length from lattice QCD // Phys. Rev. D. – 2008. – Vol. 77. – P.094507.

[59] A. Martnez Torres. D. Jido. and Y. Kanada-Enyo. Theoretical study of the $KK\bar{K}$ system and dynamical generation of the K(1460) resonance // Phys. Rev. C. – 2011. – Vol. 83. – P. 065205.

[60] Y. Akaishi. K. S. Myint. and T. Yamazaki. Kaonic nuclear systems KbarN and KbarNN as decaying states // Proc. Jpn. Acad. Ser. B. – 2008. – Vol. 84. – P. 2

[61] E. Hiyama. Y. Funaki. N. Kaiser. and W. Weise.Alpha-clustered hypernuclei and chiral SU(3) dynamics // Prog. Theor. Exp. Phys. – 2014. – P. 013D01.

UDC 539

Few-body neutron and kaonic clusters

Kezerashvili R.Ya.[1,2]

[1]*Physics Department, New York City College of Technology, The City University of New York,Brooklyn, NY 11201, USA*
[2]*The Graduate School and University Center, The City University of New York,New York, NY 10016, USA*
e-mail: rkezerashvili@citytech.cuny.edu

In this review, we try to summarize the results of experimental search and theoretical studies within variational methods, the method of Faddeev and Faddeev-Yakubovsky equations, and the method of hyperspherical harmonics for the lightest neutron and kaonic clusters. In particular, we discuss few-body neutron clusters: bineutron, trineutron and tetraneutron. Related to few-body kaonic clusters the results of calculations for binding energies and widths for the $K^- pp$ and $\bar{K}NNN$ kaonic systems are presented and discussed.

Key words: Trineutron, tetraneutron, kaonic clusters.
PACS: 21.10.Dr, 21.45.-v, 27.10.+h

1 Introduction

The cataclysmic events that occur near the end of the life of a star lead to one of only three possible final states: a white dwarf, a neutron star, or a black hole. The mass of the star, particularly that of the core, appears to be the primary factor in determining the final state. A more massive star would need to be hotter to balance its stronger gravitational attraction. While a star is burning, the heat in the star pushes out and balances the force of gravity. When the star's fuel is spent, and it stops burning, there is no heat left to counteract the force of gravity. How much mass the star had when it died determines what it becomes. Detailed calculations have shown that for star with mass less than about 1.4 times the mass of our sun electron degeneracy pressure permanently halts collapse. White dwarfs are stable cold stars that are supported by electron degeneracy pressure. Calculations show that stars that have between 1.4 and 3 times the mass of the sun implode into neutron stars that are the end product of stellar evolution, and their outer core is composed of neutrons at truly enormous densities. The central region of the neutron star is supported by the degeneracy pressure of neutrons. A star with mass greater than 3 times than of the sun gets crushed into a single point - a black hole.

At high density, when the sum of masses of a proton and electron and Fermi energy exceeds the neutron mass, it is energetically favorable to combine a proton and an electron into a neutron: $p + e^- \leftrightarrow n + \nu_e$. Both neutron and neutrino rich matter are produced at the core. Therefore, at higher densities, matter becomes more and more neutron-rich. A progressive neutronization of matter at higher and higher densities makes a lower energy state. An attractive pairing interaction between neutrons, can couple them to form a state with integer spin and, therefore, paired neutrons act like bosons. These "bosons" can form a condensate-like state in which all of the bosons occupy the same quantum state and form a superfluid. Just as the pairing of protons that are charged fermions forms a superconductor. In that same general sense, we also can have superconductivity and superfluidity in neutron stars. Thus, we can have superconductivity and superfluidity in the outer core of neutron stars. Superconductivity and superfluidity, if observed in neutron stars, could tell us a lot about the pairing and hence inform us about aspects of nuclear physics that are mighty difficult to get from laboratories. Information on multineutron forces obtained in studies of multineutron systems is a critical input into theories of neutron stars [1, 2]. Therefore, the study of dineutrons, trineutrons, tetraneutrons as well as multineutrons and neutron drops is important for understanding the structure and processes in neutron stars. From another side, early suggestions for kaon condensate in dense matter [3 – 6] motivated the search for bound states of kaons in nuclei, since the kaon–nucleus interaction could answer the question of whether kaon condensation takes place in the inner core of neutron stars. This is one of the reasons why the study of few-body kaonic systems have attracted much attention in the last decade. Today, our

understanding of the details of the process of neutron star formation is not very well defined. This is presently an active area of research.

Below, I am reviewing and presenting the status of studies of three- and four-body neutron and kaonic systems.

2 Few-body neutron clusters

A simple fact has now been established: all nuclei that are heavier than the hydrogen nucleus are made up of both protons and neutrons. The question then arises as to whether a nuclei made up of only neutrons or protons can exist. On the basis of current knowledge the theoretical answer is probably ... Well, let's discuss this!

During the last 60 years, experimental search and theoretical investigation has continued to focus on atomic nuclei consisting only of neutrons. A recently reported observation of the tetraneutrons [25] and some theoretical results, however, revives old questions: do dineutrons, trineutrons and multineutrons nuclei exist? Can a nucleus be made up of neutrons only? Does neutron matter exist? The existence of a bound dineutron, multineutrons nuclei, neutron drops and neutron matter is of great importance, as it would challenge our understanding of nuclear few-body systems and the evolution of the universe. The answers to these questions would most certainly require a revision of modern realistic models of the nucleon-nucleon force and three-nucleon interaction and more over introduce a four-nucleon interaction.

A free neutron decays into a proton, an electron, and an antineutrino, which is associated with an electron. The time of this decay is about 1000 seconds. In other words, a free neutron may exist for only about 16 minutes. What about the existence of the system of two bound neutrons known as a dineutron? Searching resonances and bound states in a system of two neutrons is a well defined problem and numerically well under control. The two neutron resonances are associated with the poles of the S -matrix, which are embedded in the fourth-quadrant of the complex k plane. They are solutions of the time-dependent Schrödinger equation without the incoming wave and the outgoing wave increasing exponentially at infinity. In Ref. [7] it was mentioned that nonrealistic Volkov potentials [8] do have bound dineutrons. However, these potentials are not realistic; they produce bound ^{2}n, with the same binding energies as their deuterons; they have no tensor or LS terms; and they cannot reproduce modern phase shift analyses in any partial wave [7]. Theoretical calculations show no existence of the resonance or bound states in the system of two neutrons for all the existing realistic and phenomenological models of the nucleon-nucleon interaction. Experimental searches of the dineutron have been also performed using different nuclear reactions but no evidence for the existence of the ^{2}n has been found. Thus, today we are confident that dineutrons do not exist but could very nearly exist: a slight increase in the attraction between the two particles would result in a bound structure, the dineutron being formed. However, in neutron-rich matter like a neutron star where the density 3-times as much as the normal nuclear density would nucleon-nucleon interaction modified so that brings two neutrons to be bound. This question needs to be addressed. Research into the possibility that nuclei have more than two neutrons shows that, very often, adding a further neutron increases the stability of the structure. The question then arises as to whether a neutron system made up of more than two neutrons could exist.

A three-neutron resonance has not yet been firmly established. The weight of early experimental evidence reviewed in Ref. [9] is strongly against the existence of a bound state of the three-neutron system, and only controversial evidence of a three-neutron resonance was cited. The situation up to 1987 has been reviewed in the compilation [10]. Reference [11] reported the possible existence of the trineutron through the reaction ^{3}H(n, p)^{3}n. Later, the same reaction was studied in Ref. [12] and no evidence for the existence of the trineutron was found. Searches for a bound state of the three neutron were conducted in reactions: ^{3}H(π^-, γ)^{3}n, ^{3}H(π^-, π^+)^{3}n and ion collision reactions such as ^{7}Li(^{11}B, ^{15}O)^3 n and ^{2}H(^{12}C, ^{13}N)^3 n. As of yet, none of these reactions have provided evidence for a bound trineutron. The most intensive search for the prediction of a bound trineutron has been performed using a pionic double charge exchange reaction ^{3}He(π^-, π^+)^{3}n. An investigation [13] of the process ^{3}He(π^-, π^+)^{3}n found no evidence of the existence of the ^{3}n or resonance state of three neutrons. Earlier study [14] pointed to resonance in the three neutrons. However, the resonance behavior can be explained by the final state interaction of three neutrons in continuum spectrum as was demonstrated in Refs. [15, 16]. The double charge exchange process on ^{3}He was also investigated in Ref. [17], which while criticizing previous work [14] pointed again to a three-neutron resonance around 12 MeV excitation. For a

trineutron the bound state has been studied extensively in the last four decades resulting in a numerically precise solution of the Faddeev equations in momentum and coordinate space, and using the hyperspherical functions method. Independent of the theoretical framework, such as the Faddeev formalism [18, 19], the method of the hyperspherical functions or variational calculations, most theoretical works do not predict a bound ^{3}n state in the three-neutron system. However, it has been stressed in Ref. [20] that subtle changes in the nucleon-nucleon potential, which would not affect results from phase shift analyses, may lead to bound neutronic nuclei. To summarize, although the double charge exchange reaction of negative pions on ^{3}He nucleus has been examined at various incident energies of pion, from the analysis of the invariant mass spectra for three neutrons, no evidence for the bound trineutron has been found. However, a calculation [21] predicts a resonance state with the width of 13 MeV in the three-neutron system. Although such a resonance would easily fit early interpretation of data on pionic double charge exchange on ^{3}He [14] (this observation was supported by measurements reported in Ref. [17] in 1986), more recent investigations [13, 22, 23] of this process do not give any experimental evidence for it.

Several more recent experiments have strengthened the evidence against the bound trineutron and have failed to discover a resonance structure that cannot be otherwise explained. The study [24] shows that realistic nucleon-nucleon interaction models exclude any possible experimental signature of three-neutron resonances. Thus, today there is no unambiguous answer for the existence of the three-neutron nucleus. Apart from these aspects the question of whether multineutron systems exist is of principal interest by itself.

This year, a candidate resonant tetraneutron state with the energy of $0.83 \pm 0.65(\text{stat}) \pm 1.25(\text{syst})$ MeV above the threshold of four-neutron decay has been found in the missing-mass spectrum obtained in the double-charge-exchange reaction ^{4}He(^{8}He, ^{8}Be) at 186 MeV/u [25]. The experiment was performed at the RI Beam Factory at RIKEN. Previously, in experiments, the system of four bound neutrons ^{4}n was searched through using heavy-ion transfer reactions such as ^{7}Li(^{11}B, ^{14}O)^4 n [26], ^{7}Li(^{7}Li, ^{10}C)^4 n [27], and the pion double charge exchange reaction ^{4}He(π^-, π^+)^{4}n. Early measurements of the ^{4}He(π^-, π^+)^{4}n reaction carried out in search of evidence for ^{4}n are summarized in the compilation [28]. No bound ^{4}n was detected in these early works. Later the momentum spectrum from the pion double charge exchange reaction was measured in Ref. [29] in a search for ^{4}n. Note, however, that the theoretical study of Ref. [30] reported that the final-state interaction in the four-neutron system in continuum spectrum is so strong that the tetraneutron could not be observed in the kinematic region explored in Ref. [29]. Pion spectra and total cross sections for pion double charge exchange were also measured in Refs. [31 – 33] for different incident pion energies. No evidence for ^{4}n was obtained. Several attempts have been made to find a bound tetraneutron system by using a uranium fission reaction [34, 35, 36] and the experimental observation of ^{4}n was claimed in the interaction of 100 MeV α–particle with uranium nucleus in Ref. [36].

Several theoretical studies of pion double charge exchange on ^{4}He have been reported. In Ref. [37] cross sections were calculated in a model in which two single charge exchange scatterings occur. The reaction was studied in the framework of a four-body hyperspherical basis method in Ref. [38] but existing experimental data were interpreted without bound or resonance state of four neutrons. No bound tetraneutron was found in Ref. [39] within the angular potential functions method, in Ref. [40] using the stochastic variational method and in Refs. [41] and [42] within the hyperspherical functions method. In contrast, calculations within the hyperspherical functions method led the authors in Ref. [43] to the conclusion that the tetraneutron may exist as a resonance only for the NN potential that binds the dineutron.

In the new millennium, an experimental search and theoretical study of tetraneutron transitioned to a new phase. In 2002 an international team led by physicists from the Particle Physics Laboratory of Caen, have presented in Ref. [44] experimental results suggesting the existence of a bound tetraneutron. These results have been obtained by using the exotic beams of the French national large heavy-ion accelerator in Caen and by studying the breakup reaction of ^{14}Be into ^{10}Be and bound tetraneutron. The heavy-ion transfer reactions, and the pion double charge exchange reaction require considerable reconfiguration of the target nuclei and should be strongly suppressed. In contrast, the nucleus ^{14}Be consists of a strongly bound core ^{10}Be and four weakly bound neutrons that could form a tetraneutron-like configuration, which might be shaken off in the ^{14}Be breakup. In experiment [44] events were observed that exhibit the tetraneutron cluster liberated in the breakup of ^{14}Be. The lifetime suggested by this measurement would indicate that

the tetraneutron is a stable particle. In 2016, the resonant tetraneutron state was found in the reaction ^{4}He(^{8}He, ^{8}Be) [25]. If confirmed, these discoveries, which would call into question current theoretical models, will have major repercussions in the field of nuclear physics.

The existence of the bound tetraneutron system was also discussed in theoretical studies [45 – 49]. In Ref. [46] it was proposed that, if tetraneutron existed, it could be formed by a bound state of two dineutron molecules. The possibility for a tetraneutron to exist as a low-energy resonance state was studied in Ref. [49]. In [45] the hyperspherical functions method and realistic nucleon-nucleon interactions have been used to argue against the existence of a tetraneutron. It was pointed out that due to the small probability for a pair of neutrons to be in the singlet even state, the two-body nuclear force cannot by itself bind four neutrons, even if it could bind a dineutron. An unrealistic modification of the nucleon-nucleon force or introduction of unrealistic four-nucleon forces would be needed to bind a tetraneutron. As for experimental searches of the other light bound multineutron systems, the calculations presented in Ref. [45] suggest that they might be unsuccessful. It is also important to mention that Ref. [7] shows that it does not seem possible to change any modern two- and three-nucleon interaction to bind a tetraneutron without destroying many other successful predictions of these interactions. This means that, should recent experimental claims [44, 25] of a bound tetraneutron be confirmed, our understanding of nuclear forces will have to be significantly changed.

Theoretical investigations of multineutrons have been carried out for a system of six, eight and ten bound neutrons using the hyperspherical functions method with different nucleon-nucleon interactions [45]. Results of calculations show no bound states for these neutron systems. Theorists are also studying neutron drops [50, 51]. Neutron drops are collections of neutrons held together by both an external nuclear well and the interaction between neutrons. The properties of these drops can be used as "data" for fitting simpler effective interaction models that are employed in the study of large neutron-rich nuclei, the crusts of neutron stars, and neutron matter.

3 Few-body kaonic clusters

Kaonic nuclei carry important information concerning the $\bar{K}$ – nucleon interaction in the nuclear medium. This information is very important in understanding kaon properties at finite density and in determining constraints on kaon condensation in high-density matter. The latter will allow one to adjust the methods developed in condensed matter physics for exciton and excitonic polariton condensates (see, for example, [52, 53]) to study the kaon condensation. The best way to understand the many body kaonic nuclear system is to study the simplest three- and four-body clusters: $\bar{K}NN$, and $\bar{K}NNN$. The light kaonic clusters $\bar{K}NN$, and $\bar{K}NNN$ represent three- and four-body systems and theoretically can be treated within the framework of few-body physics approaches. In the recent past much efforts have been focused on the calculations of quasibound state energies and widths for three- and four-body kaonic clusters. A variety of methods have been used in configuration and momentum spaces, to obtain eigenvalues for energy and width of quasibound states using diverse sets of $\bar{K}N$, and NN interactions. These include but are not limited by variational method approaches [54 – 65], the method of Faddeev equations in momentum and configuration spaces [67 – 79], Faddeev-Yakubovsky equations [77] and the method of hyperspherical harmonics in configuration and momentum spaces [80, 81, 79].

On the experimental side, several experiments have been performed to search for the kaonic clusters using various nuclear reactions starting from the first measurement reported by the FINUDA collaboration for the K^-pp cluster [82] and including the most recent reports of J-PARC E15 and J-PARC E27 collaborations [83, 84] and HADES collaboration [85]. Recent HADES collaboration partial wave analysis of the reaction $pp \rightarrow pK^+\Lambda$ at 3.5 GeV to search for the K^-pp bound state shows that at a confidence level 95% such a cluster cannot contribute more than 2–12% to the total cross section with a $pK^+\Lambda$ final state [85]. However, there are important reports of K^-pp experimental searches done by the DISTO and J-PARC E27 collaborations. They reported some signal at 100 MeV below the K^- and two protons threshold, which may be related to the kaonic cluster K^-pp. J-PARC E27 collaboration has observed a K^-pp -like structure in the $d(\pi^+, K^+)$ reaction at 1.69 GeV/c, while Ref. [86] reports an indication of a deeply bound K^-pp state in the $pp \rightarrow p\Lambda K^+$ reaction at 2.85 GeV. The authors of Refs. [87], [88] (experiment E471) announced the experimental discovery of the bound state $\bar{K}ppn$, named $S^0(3115)$, with quantum numbers $I(J^P) = 1(\frac{3}{2}^+)$. The results have been checked in a new experiment

with larger statistics, and have been withdrawn. The ambiguous situation with the search of kaonic clusters has led the KEK-PS collaboration, experiment E549 [89], [90] to carry out a new experimental search with improved resolution and higher statistics compared with the E471 experimental setup. In the search for the neutral tribaryon with strangeness $S = -1$ and isospin 1 by missing-mass analysis of the inclusive $^4He(K^-_{stopped}, p)$ reaction with the quite high statistics for protons, no statistically significant signal of the narrow structure was observed. Therefore, the situation is still controversial and the existence, for example, of the K^-pp quasibound state has not been established yet. Thus, the theoretical and experimental study of composite systems of K – mesons and nucleons is still a challenging issue in nuclear physics.

Table 1 – Summary of the theoretical studies for the K^-pp cluster.

Method	B(K^-pp) MeV	Width, Γ MeV	$\bar{K}N$	References
Variational	48	61	AY	[54], [55], [59]
Methods	20 ± 3	40-70	Chiral model	[62], [63]
	40-80	40-85	Sep.	[64]
	20-35	20-65	Chiral model	[65]
	124	12	AY	[66]
Methods of	47-70	90-100	Sep. En. Indep.	[67], [68], [78]
Faddeev	~ 32	$\sim$ 50-65	Sep. En. Dep.	[78]
equations	45-95	45-80	Sep. En. Indep.	[69], [70], [72]
	9-16	34-40	Sep. En. Dep.	[72]
	30-40	50-80		[73]-[76]
	~ 52		Sep. En. Indep.	[77]
	46.3-47.3		AY	[79]
	20.6-21.6		HW	[79]
Methods of HH	~ 16	~ 41	Chiral model	[80]
	15-17	36-43	Chiral model	[81]
	40-48	75-96	AY	[81]
	46.3-46.5	74.5-84.3	AY	[79]
	20.5-206	48.1-49.5	HW	[79]

Let us focus on results of the calculations of the binding energy and width for the three-body $\bar{K}NN$ and four-body $\bar{K}NNN$ kaonic clusters. To describe these system were used an energy-independent and energy-dependent local as well as a separable $\bar{K}N$, effective interactions. The local energy-independent effective $\bar{K}N$, interaction was constructed in Ref. [54, 59] based on a phenomenological approach so as to reproduce the existing experimental data for the $\bar{K}N$ scattering length, the mass and width of the Λ (1405) hyperon and the $1s$ level shift caused by the strong $\bar{K}N$, interaction in the kaonic hydrogen atom. We refer to this potential as the Akaishi–Yamazaki (AY) potential. The energy-dependent local effective $\bar{K}N$, interaction given in Ref. [91] was derived based on the chiral unitary approach for the $s-$ wave scattering amplitude with strangeness $S = -1$, and reproduces the total cross sections for the elastic and inelastic K^-p scattering, threshold branching ratios, and the $\pi\Sigma$ mass spectrum associated with the Λ (1405). Hereafter we refer to this potential as the HW potential. For the calculations of the binding energy and the width with the variational method, the method of hyperspherical harmonics (HH) and the Faddeev equations in configuration space as input for the $\bar{K}N$, interaction were used the energy-dependent effective HW and the phenomenological AY potentials, and different NN

interaction. When the kaonic clusters treated within the Faddeev or Faddeev-Yakubovsky equations separable potentials are used as the input for the NN and $\bar{K}N$, interactions.

Calculations for a binding energy and width of the kaonic three-body system are presented in Table 1 are performed using different potentials for the NN interaction, as well as the energy-independent and the energy-dependent effective potentials for the description of the kaon–nucleon interaction. Such an approach allowed us to examine how the K^-pp cluster's structure depends on different choices of the $\bar{K}N$, interactions for the same NN potential, as well as to investigate its dependence on different choices of the NN interaction for the same $\bar{K}N$, interaction, and to understand the sensitivity of the system to the input interactions. Therefore, the use of different NN potentials and $\bar{K}N$, interactions allows one to perform a validity test for the lightest kaonic clusters against various NN and $\bar{K}N$, interactions.

One can address the theoretical discrepancies in the binding energy and the width for the K^-pp system presented in Table 1 related to the different NN and $\bar{K}N$, interactions or a method of calculations. However, analysis of theoretical studies indicates that mostly the discrepancies of the results of calculations for the binding energy and the width are related to the treatment of effective $\bar{K}N$, interaction. The binding energy found in Ref. [79] using the differential Faddeev equations and HH methods are in good agreement with the one obtained with the variational method. This is a good sign that the binding energy does not depend significantly on the method of calculation. Different variational approaches are of comparable quality in their high degree of consistency and all results are consistent. Differences are mostly due to a different $\bar{K}N$, input and possibly slightly due to the NN input.Variational calculations as well as calculations using the differential Faddeev equations and HH methods confirm that the effective $\bar{K}N$, interaction derived from chiral SU(3) dynamics yields a shallowly bound K^-pp cluster, while the phenomenological energy independent AY potential predicts much deeper binding energy for all considered NN interactions. Most importantly, the results support the conclusion that the key role in binding the K^-pp system is played by the $\bar{K}N$ interaction and the $\bar{K}N$ potential obtained based on chiral SU(3) dynamics leads to binding energies of relatively low values.

The calculations with the Faddeev equations for the three-body system with coupled $\bar{K}NN$ and $\pi\Sigma N$ channels performed in Refs. [67], [68] with separable two-body potentials yield larger bindings than obtained in a similar approach in Ref. [69]. Later, two of the authors of [69] repeated their calculation in [70, 72] using two models with the energy-independent and energy-dependent potentials for the s – wave $\bar{K}N$, interaction, and their calculations yield smaller values for the binding energy 44-58 MeV and width 34-40 MeV [72]. The Faddeev calculations [78] for the $\bar{K}NN$ quasibound state with the two phenomenological and the energy-dependent chirally motivated models of the $\bar{K}N$ interaction lead to the following results for the K^-pp cluster: 32 MeV with the chirally motivated models and 47 - 54 MeV with the phenomenological $\bar{K}N$ potentials. Therefore, one can conclude that the Faddeev calculations for the energy-independent models for the $\bar{K}N$ interaction predict a deeper binding energy than that of the energy-dependent description of the $\bar{K}N$ interaction.

Recently, Faddeev-Yakubovsky calculations [77] were made for the four-particle K^-pp kaonic cluster, where the quasibound states were treated as bound states by employing real s – wave two-body separable potential models for the $\bar{K}$ – nucleon interactions as well as for the NN interaction. Fully four-body nonrelativistic realistic calculations of $\bar{K}NNN$, quasibound states within the method of HH in configuration space, using realistic NN potentials and subthreshold energy dependent chiral $\bar{K}N$ interactions, were presented in Ref. [80]. Given that below we present the results of our calculations for the $\bar{K}NNN$ quasibound states in the framework of the method of HH in momentum representation using AV18 [93] and M [96] NN potentials and AY and HW $\bar{K}N$, interactions as inputs. To find the binding energies with the above-mentioned set of potentials, we solve a system of coupled integral equations for the hyperradial functions [79]. In the calculations we limit our consideration with the value 10 for the global momentum getting a reasonable convergence for the binding energy. In Table 2 we present our results for the $\bar{K}NNN$, cluster that we compare with those obtained via different methods. The results of our calculations for the energy and the width show dependence on the NN potentials and on the $\bar{K}N$, interactions. However, this dependence is dramatically different: for the same $\bar{K}N$ interaction

and different *NN* potentials the ground state energy and the width change by about $3-15\%$, while for the same *NN* potential and different $\bar{K}N$ interaction the energy changes by a factor of more than 3 and the width changes by more than twice. The comparison of our results for the K^-ppn and K^-pnn clusters obtained for theAV18 *NN* interaction and the HW $\bar{K}N$ interaction with calculations [80] within the variational HH method for the AV14 *NN* interaction and shallow chiral $\bar{K}N$ interaction shows a reasonable agreement. The predictions [58] for the binding energy and the width for the kaonic clusters studied based on a framework of antisymmetrized molecular dynamics and employing adopted AY [54] potential as a bare $\bar{K}N$ interaction are presented in the last column of Table 2. As is seen from Table 2 there is a reasonable agreement for the widths for the K^-ppn and K^-pnn clusters among the present study and study [80] in case of HW potential. However, the widths of the K^-ppn and K^-ppp systems are largely different among our study and an earlier study [58] in the case of the AY potential. Interestingly enough, our calculations for the AY interaction indicate that for the system $\bar{K}NNN$, the cluster K^-ppp is more deeply bound than the K^-ppn, which contradicts the results [58]. In a shell-model picture, one of three protons in the K^-ppp should be raised up to 0 p orbit due to the Pauli principle, while all nucleons in K^-ppn occupy the 0 s orbit. So, the nave expectation is that the K^-ppn is energetically lower than the K^-ppp. From the other side the larger number of the strongly attractive K^-p pairs in the $(\frac{3}{2}^+,1)$ state than in the $(\frac{1}{2}^-,0)$ state may cause a lowering of the $T=1$ state, even below the $T=0$, although the third proton in the $T=1$ state should be flipped up to the orbital $(0p_{3/2})$. The final picture depends on the strength of the $\bar{K}N$ interaction. The attractive AY interaction is much stronger than the effective HW interaction. The strength of the $\bar{K}N$ interaction plays an important role that may lead to the nuclear compression.

Table 2 – The binding energy B and width Γ for the $\bar{K}NNN$ system calculated in the framework of the method of HH in the momentum representation for different interactions with results from Refs. [58], [77] and [80]. The parity π includes the eigen parity of antikaon

	J^π	T		AV18		M		[77]	[80]	[58]
				AY	HW	AY		HW		
K^-ppn	$\frac{1}{2}^-$	0	B, MeV	92.1	28.6	97.9	29.3	28.9	69	110.3
			Γ, MeV	83.4	30.3	84.1	32.9	30.8		21.2
K^-pnn	$\frac{1}{2}^-$	1	B, MeV	64.6	17.2	66.7	18.5	18.7		
			Γ, MeV	74.2	27.1	80.4	31.0	31.4		
K^-ppp	$\frac{3}{2}^+$	1	B, MeV	101.9	25.8	107.6		28.1		96.7
			Γ, MeV	87.9	28.1	89.8		31.2		12.5

4 Conclusions

Today there is no unambiguous answer for the existence of the trineutron as a bound or resonance state. There are three claims of the experimental observation of ^{4}n: one in a fission reaction [36], and the recent two in the breakup reaction of ^{14}Be into ^{10}Be and ^{4}n [44], and in the double-charge-exchange reaction ^{4}He(^{8}He, ^{8}Be) [25]. However, in theoretical studies, no evidence for ^{4}n was obtained within the existing modern two- and three-nucleon interaction. If the experimental discoveries [44] and [25] would be confirmed, this would call into question current theoretical models of nuclear forces.

The results of calculations within the different theoretical methods show that the binding energy and the width of the K^-pp system depend entirely on the ansatz for the $\bar{K}N$ interaction and substantially change when the AY and HW potentials are used. The predicted values for the binding energy and the

width are in considerable disagreement.Model calculations with the $\bar{K}N$ interaction derived based on the chiral unitary approach predict a shallow binding state with large width for the K^-pp cluster. For example, for the K^-pp cluster, the predicted values for the binding energy and the width are 9–95 MeV and 20–110 MeV, respectively. The sensitivity of the binding energy and the width to the details of the *NN* potentials as long as the K^-pp kaonic system is strongly or weakly bound dependence on different types ofinteraction is weak.

Finally, the situation is still controversial and the existence of theandquasibound states have not been established yet. Many calculations show that, for theand four-particle kaonic clusters, the binding energy is larger or comparable to the width. As a consequence, perhaps, we are facing a situation in which it is hard to identify the resonances that would make the experimental observation challenging. Thus, the theoretical and experimental study of composite systems of mesons and nucleons is still a challenging issue in nuclear physics.

References

[1] P. B. Demorest. T. Pennucci. S.M. Ransom. M.S.E. Roberts. and J.W.T. Hessels. Nature (London)– 2010. – Vol. 467.– P. 1081.

[2] E. Hiyama. Few-Body Syst. – 2015. – Vol. 56.– P. 787.

[3] D. B. Kaplan and A. E. Nelson. Strange goings on in dense nucleonic matter // Phys. Lett. B. – 1986. – Vol. 175. – P. 57.

[4] G. E. Brown. The equation of state of dense matter: supernovae. neutron stars and black holes // Nucl. Phys. A. – 1994. – Vol. 574. – P. 217.

[5] G. E. Brown. M. Rho. Chiral restoration in hot and/or dense matter // Phys. Rep. – 1996. – Vol. 269. – P.333.

[6] C. H. Lee. Kaon condensation in dense stellar matter// Phys. Rep. – 1996. – Vol. 275. – P. 255.

[7] S. C. Pieper. Can Modern Nuclear Hamiltonians Tolerate a Bound Tetraneutron? // Phys. Rev. Lett. – 2003. – Vol. 90. – P. 252501.

[8] A. B. Volkov. Equilibrium deformation calculations of the ground state energies of 1p shell nuclei // Nucl. Phys. – 1965. – Vol. 74. – P. 33.

[9] S. Fiarman. S. S. Hanna. Energy levels of light nuclei A = 3 // Nucl. Phys. A. – 1975. – Vol. 251. – P. 1.

[10] D. R. Tilley. H. R. Weller. and Hasan. Energy levels of light nuclei A = 3 // Nucl. Phys. A. – 1987. – Vol.474. – P. 1.

[11] V. Ajdaic. M. Cerineo. B. Lalovi. G. Pai. I. laus. and P. Toma. Reactions H3(n.p)3n and H3(n.H4)γ at En=14.4 MeV // Phys. Rev. Lett. – 1965. – Vol. 14. – P.444.

[12] S. T. Thornton. J.K. Bair. C.M. Jones. and H.B. Willard. Search for the Trineutron // Phys. Rev. Lett. – 1966. – Vol. 17. – P. 701.

[13] J. Grater. P. A. Amaudruz. R. Bilger. et al. // Eur. Phys. J. A. – 1999. – Vol. 4. – P. 5

[14] J. Sperrinde. et al. // Phys. Lett. B. – 1970. – Vol.32. – P. 185.

[15] R. I. Jibuti. R. Ya. Kezerashvili. Sov. J. Nucl. Phys. – 1984. – Vol. 39. – P. 264.

[16] R.I. Jibuti. R.Ya. Kezerashvili. Double-charge-ex change reactions of π-mesons on three- and four-particle nuclei // Nucl. Phys. A. – 1985. – Vol.437. – 1q 687.

[17] A Stez et al.Pion double charge exchange on 3He and 4He // Nucl. Phys. A. – 1986. – Vol. 457. – P. 669.

[18] H. Witala. W. Glöckle. Resonances in the three-neutron system // Phys. Rev. C. – 1999. – Vol. 60. – P. 024002.

[19] A. Hemmdan. W. Glöckle. and H. Kamada. Indications for the nonexistence of three-neutron resonances near the physical region // Phys. Rev. C. – 2002. – Vol. 66. – P. 054001.

[20] A. I. Baz. V.N. Bragin. Do multineutrons really exist? // Phys. Lett. B. – 1972. – Vol. 39. – P. 599.

[21] A. Csoto. H. Oberhummer. R. Pichler. Searching for three-nucleon resonances // Phys. Rev. C. – 1996. – Vol. 53. – P. 1589

[22] J. Grater. et al.Inclusive measurements of pionic double charge exchange on 3He at low energies // Phys. Lett. B. – 1999. – Vol. 471. – P. 113.

[23] M. Yuly et al.Pion double charge exchange and inelastic scattering on 3He // Phys. Rev. C. – 1997. – Vol.55. – P. 1848.

[24] R. Lazauskas and J. Carbonell. Three-neutron resonance trajectories for realistic interaction models // Phys. Rev. C. – 2005. – Vol. 71. – P. 044004.

[25] K. Kisamori. et al. Candidate Resonant Tetraneutron State Populated by the He4(He8,Be8) Reaction// Phys Rev. Lett. – 2016. – Vol. 116. –P.052501.

[26] A. V. Belozyorov. C. Borcea. Z. Dlouhy. and A. M. Kalininю Search for the tri- and tetra-neutron in reactions induced by 11B and 9Be ions on 7Li // Nucl. Phys. A. – 1988. – Vol. 477. – P. 131.

[27] D. V. Aleksandrov. et al. Yad. Fiz. 47. – 1988. – P. 3.

[28] D. V. Aleksandrov. E. Y. Nikol. B. G. Novatski. S. B. Sakuta. and D. N. Stepanov.Search resonances in systems of three and four neutrons in the reactions 7Li (7Li, 11C) and 7Li (7Li, 10C) in the nuclei 7Li // JETP Lett. – 2005. – Vol. 81. – P. 43.

[29] S. Fiarman. W.E. Meyerhof. Energy levels of light nuclei A = 4 // Nucl. Phys. A. – 1973. – Vol. 206. – P.1.

[30] J. E. Urgan. et. al.Search for the tetraneutron by the double-charge-exchange of negative pions // Phys. Lett. B. – 1984. – Vol. 144. – P. 333.

[31] R. Ya. Kezerashvili. Sov. J. Nucl. Phys. – 1986. – Vol. 44. – P. 542.

[32] A. Stetz. at. al.Pion Double Charge Exchange on He4 and Meson Exchange Currents// Phys. Rev. Lett. – 1981. – Vol. 47. – P. 782

[33] E. R. Kinney. et. al.Inclusive pion double charge exchange in He4// Phys. Rev. Lett. – 1986. – Vol. 57. – P.3152.

[34] T. P. Gorringe. et. al.Search for the tetraneutron using the reaction He4(π−,π+)4n // Phys. Rev. C. – 1989. – Vol. 40. – P. 2390.

[35] J. P. Schiffer and R. Vanderbosch. Search for a particle-stable tetra neutron // Phys. Lett. 5. – 1963. – P.292.

[36] S. Cierjacks. G. Markus.W. Michaelis. and W. Ponitz // Phys. Rev. B. – 1965. – Vol. 345. – P. 137.

[37] V. A. Ageev. I. N. Vishnevskii. V. I. Gavrilyuk. et.al. Ukr. J. Phys. – 1986. – Vol. 31. – P. 1771.

[38] W. R. Gibbs. B. F. Gibson. A. T. Hess. and G. J. Stephenson. Pion double charge exchange on He4 // Phys. Rev. C. – 1977. – Vol. 15. – P. 1384.

[39] R. I. Jibuti. R. Ya. Kezerashvili. K. I. Sigua. Investigation of π−(π+)+4He→π+(π−) + 4n (4p) // Phys. Lett. B. – 1981. – Vol. 102. – P. 381;

[40] Yad. Fiz. – 1980. – Vol. 32. – P. 1536

[41] A. M. Gorbatov. et. al. Yad. Fiz. – 1989. – Vol.50. – P. 347.

[42] K. Vagra. Y. Suzuki.Precise solution of few-body problems with the stochastic variational method on a correlated Gaussian basis // Phys. Rev. C. – 1995. – Vol.52. – P. 2885.

[43] A. M. Badalyan. T. I. Belova. N. B. Konyuhova. V.D. Efros. Sov. J. Nucl. Phys. – 1985. – Vol. 41. – P.926.

[44] S. A. Sofianos S. A. Rakityansky. G. P. Vermaak. Subthreshold resonances in few-neutron systems // J.Phys. G: Nucl. Part. Phys. – 1997. – Vol. 23 – P. 1619.

[45] I. F. Gutich. A. V. Nesterov. I. P. Okhrimenko Yad. Fiz. – 1989. – Vol. 50. – P. 19.

[46] F. M. Marques. et. al.Detection of neutron clusters// Phys. Rev. C. – 2002. – Vol. 65. – P. 0444006.

[47] N. K. Timofeyuk.Do multineutrons exist? // J.Phys. G: Nucl. Part. Phys. – 2003. – Vol. 29. – P. L9 .

[48] C. A. Bertulani and V. Zelevinsky.Is the tetraneutron a bound dineutron–dineutron molecule? // J.Phys. G. – 2003. – Vol. 29. – P. 2431.

[49] L.V. Grigorenko. N. K. Timofeyuk. and M.V.Zhukov. Broad states beyond the neutron drip line // Eur. Phys. J. A. – 2004. – Vol. 19. – P. 187.

[50] I. V. Simenog. B. E. Grinyuk. Yu. M. Bidasyuk. Asymptotic properties of structuralfunctions of nucleus6Li and 6He whitin three-particle models // Ukr. J. Phys. – 2006. – Vol. 51. – P. 954.

[51] Y. A. Lashko and G. F. Filippov. Cluster Structure of a Low-Energy Resonance in Tetraneutron // Phys. At. Nucl. – 2008. – Vol. 71. – P. 209.

[52] B. S. Pudliner. A. Smerzi. J. Carlson. V. R. Pandharipande. S. C. Pieper. and D. G. Ravenhall // Phys. Rev. Lett. – 1996. – Vol. 76. – P. 2416 .

[53] P. Maris. J. P. Vary. S. Gandolfi. J. Carlson. and S. C. Pieper. Properties of trapped neutrons interacting with realistic nuclear Hamiltonians // Phys. Rev. C. – 2013. – Vol. 87. – P. 054318.

[54] O.L. Berman. R.Ya. Kezerashvili. G.V.Kolmakov. and Yu.E. Lozovik. Turbulence in a Bose-Einstein condensate of dipolar excitons in coupled quantum wells // Phys. Rev. B. – 2012. – Vol. 86. – P.045108.

[55] O. L. Berman. R. Ya. Kezerashvili. K. Ziegler // Phys. Rev. B. – 2012. – Vol. 86. – P. 235404.

[56] Y. Akaishi and T. Yamazaki. Superfluidity and collective properties of excitonic polaritons in gapped graphene in a microcavity // Phys. Rev. C. – 2002. – Vol.65. – P. 044005.

[57] T. Yamazaki and Y. Akaishi. (K−, π−) production of nuclear $\bar{K}$ bound states in proton-rich systems via Λ□ doorways // Phys. Lett. B. – 2002. – Vol.535. – P. 70.

[58] T. Yamazaki. A. Doté. and Y. Akaishi. Invariant-mass spectroscopy for condensed single- and double-$\bar{K}$ nuclear clusters to be formed as residues in relativistic heavy-ion collisions // Phys. Lett. B. – 2004. – Vol. 587. – P. 167.

[59] A. Doté. H. Horiuchi. Y. Akaishi. and T.Yamazaki. High-density Full-size image (<1 K) nuclear systems with isovector deformation // Phys. Lett. B. – 2004. – Vol. 590. – P. 51.

[60] A. Doté. H. Horiuchi. Y. Akaishi. and T.Yamazaki. Kaonic nuclei studied based on a new framework of antisymmetrized molecular dynamics // Phys. Rev. C. – 2004. – Vol. 70. – P. 044313 .

[61] T. Yamazaki and Y. Akaishi. Basic K– nuclear cluster, K–pp, and its enhanced formation in the p+p→K++X reaction // Phys. Rev. C. – 2007. – Vol. 76. – P. 045201.

[62] A. Doté. H. Horiuchi. Y. Akaishi. and T. Yamazaki. The Study of Deeply Bound Kaonic Nuclei with Antisymmetrized Molecular Dynamics // Prog. Theor. Phys. Suppl. – 2002. – Vol. 146. – P. 508.

[63] A. Doté and W. Weise. // Prog. Theor. Phys. Suppl. – 2007. – Vol. 168. – P. 593.

[64] A. Doté. T. Hyodo. and W. Weise. Study of Light Kaonic Nuclei with a Chiral SU(3)-Based KN Interaction // Nucl. Phys. A. – 2008. – Vol. 804. – P. 197.

[65] A. Doté. T. Hyodo. and W. Weise. Variational calculation of the ppK system based on chiral SU(3) dynamics // Phys. Rev. C. – 2009. – Vol. 79. – P. 014003.

[66] S. Wycech and A. M. Green. Variational calculations for K– few-nucleon systems // Phys. Rev. C. – 2009. – Vol. 79. – P. 014001.

[67] A. Doté. T. Inoue. and T. Myo. J. Phys: Conf. Ser. – 2014. – Vol. 569. – P. 012084.

[68] Y. H. Li and S.S. Wu. // Chinese Phys. C. – 2009. – Vol. 33. – P. 76 .

[69] N. V. Shevchenko. A. Gal. J. Mareš. Faddeev Calculation of a K−pp Quasibound State // Phys. Rev. Lett. – 2007. – Vol. 98. – P. 082301.

[70] N. V. Shevchenko. A. Gal. and J. Mareš. and J.Révai. K–NN quasibound state and the K–N interaction: Coupled-channels Faddeev calculations of the K–NN–πΣN system // Phys. Rev. C. – 2007. – Vol. 76. – P.044004.

[71] Y. Ikeda and T. Sato. Strange dibaryon resonance in the K–NN-πYN system // Phys. Rev. C. – 2007. – Vol.76. – P. 035203.

[72] Y. Ikeda and T. Sato. Resonance energy of the K–NN−πYN system // Phys. Rev. C. – 2009. – Vol. 79. – P. 035201.

[73] A. Martnez Torres. K. P. Khemchandani. and E.Oset. Solution to Faddeev equations with two-body experimental amplitudes as input and application to JP=1/2+, S=0 baryon resonances // Phys. Rev. C. – 2009. – Vol. 79. – P. 065207.

[74] Y. Ikeda. H. Kamano. and T. Sato. Energy Dependence of K¯N Interactions and Resonance Pole of Strange Dibaryons // Prog. Theor. Phys. – 2010. – Vol. 124. – P. 533.

[75] M. Bayar. J. Yamagata-Sekihara. and E. Oset. K–NN system with chiral dynamics // Phys. Rev. C. – 2011. – Vol. 84. – P. 015209.

[76] E. Oset. D. Jido. T. Sekihara. A. Martnez Torres. K. P. Khemchandani. M. Bayar and J. Yamagata-Sekihara. A new perspective on the Faddeev equations and the system from chiral dynamics and unitarity in coupledK–NN channels // Nucl. Phys. A. – 2012. – Vol. 881. – P. 127.

[77] M. Bayar and E. Oset. Improved fixed center approximation of the Faddeev equations for the the K–NN system with S=0 // Nucl. Phys. A. – 2012. – Vol. 883. – P.57.

[78] M. Bayar and E. Oset. The K–NN system revisited including absorption // Nucl. Phys. A. – 2013. – Vol. 914. – P. 349.

[79] S. Maeda. Y. Akaishi. and T. Yamazaki.Strong binding and shrinkage of single and double K nuclear systems (K−pp, K−ppn, K−K−p and K−K−pp) predicted by Faddeev-Yakubovsky calculations // Proc. Jpn. Acad. Ser. B. – 2013. – Vol. 89. – P. 418.

[80] J. Révai and N. V. Shevchenko. Faddeev calculations of the K−NN system with a chirally motivated K−N interaction. II. The K−pp quasibound state // Phys. Rev. C. – 2014. – Vol. 90. – P. 034004.

[81] R. Ya. Kezerashvili. Sh. M. Tsiklauri. I. N. Filikhin. V. M. Suslov. and B. Vlahovic. Three-body calculations for the K−pp system within potential models // J. Phys. G: Nucl. Part. Phys. – 2003. – Vol. 43. – P. 065104.

[82] N. Barnea. A. Gal. and E. Z. Liverts. Three-body calculations for the K−pp system within potential models // Phys. Lett. B. – 2012. – Vol. 712. – P. 132 .

[83] R. Ya. Kezerashvili and Sh. M. Tsiklauri. Investigation of the structure of the few body kaonic nuclei using the method of hyperspherical functions in momentum space // EPJ Web Conf. – 2014. – Vol. 81. – P. 02022.

[84] M. Agnello. G. Beer. L. Benussi et al.Evidence for a Kaon-Bound State K−pp Produced in K− Absorption Reactions at Rest // Phys. Rev. Lett. – 2005. – Vol. 94. – P. 212303.

[85] J-PARC E15 Collaboration: T. Hashimoto. S.Ajimura. G. Beer. et al.Search for the deeply bound K–pp state from the semi-inclusive forward-neutron spectrum in the in-flight K– reaction on helium-3 // Prog. Theor. Exp. Phys. – 2015. – P. 061D01.

[86] J-PARC E27 Collaboration: Y. Ichikawa. et al.Experiment to Search for a Nuclear Kaon Bound State K−pp // Prog. Theor. Exp. Phys. – 2014. – P. 101D03;

[87] Y. Ichikawa. et al.Observation of the “K− pp”-like structure in the d(π+, K+) reaction at 1.69 GeV/c // Prog. Theor. Exp. Phys. – 2015. – P. 021D01.

[88] HADES Collaboration: G. Agakishiev. et al.Partial Wave Analysis of the Reaction p(3.5GeV)+p->pK+Λ to Search for the "ppK−" Bound State // Phys. Lett. B. – 2015. – Vol. 742. – P. 242.

[89] T. Yamazaki. et al.Indication of a Deeply Bound and Compact K−pp State Formed in the pp→pΛK+ Reaction at 2.85 GeV // Phys. Rev. Lett. – 2010. – Vol. 104. – P. 132502.

[90] T. Suzuki et al.Discovery of a strange tribaryon S0(3115) in 4He(K− stopped,p) reaction // Phys. Lett. B. – 2004. – Vol. 597. – P. 263.

[91] T. Suzuki et al.A search for deeply bound kaonic nuclear states// Nucl. Phys. A. – 2005. – Vol. 754. – P.375.

[92] M. Sato et al. Search for strange tribaryon states in the inclusive 4He(K− stopped,p) reaction // Phys. Lett. B. – 2008. – Vol. 659. – P. 107.

[93] M. Sato. et al. // Int. J. Mod. Phys. A.– 2009. – Vol.24. – P. 442.

[94] T. Hyodoand W. Weise. Effective K−N interaction based on chiral SU(3) dynamics // Phys. Rev. C. – 2008. – Vol. 77. – P. 035204 .

[95] R. B. Wiringa. R. A. Smith. and T.L. Ainsworth. Nucleon-nucleon potentials with and without Δ(1232) degrees of freedom // Phys. Rev. C. – 1984. – Vol. 29. – P. 1207.

[96] R. B. Wiringa. V. G. J. Stoks. and R. Schiavilla. Accurate nucleon-nucleon potential with charge-independence breaking // Phys. Rev. C. – 1995. – Vol. 51. – P. 38.

[97] R. A. Malfliet and J. A. Tjon. Solution of the Faddeev equations for the triton problem using local two-particle interactions // Nucl. Phys. A. – 1969. – Vol. 127. – P. 161.

[98] R. Tamagaki.Superfluid State in Neutron Star Matter. I: Generalized Bogoliubov Transformation and Existence of 3P2 Gap at High Density // Prog. Theor. Phys. – 1970. – Vol. 44. – P. 905.

[99] D. R. Thompson. M. LeMere. Y. C. Tang. Systematic investigation of scattering problems with the resonating-group method // Nucl. Phys. A. – 1977. – Vol. 286. – P. 53.

[100] Y. Akaishi. K. S. Myint. and T. Yamazaki. Kaonic nuclear systems KbarN and KbarNN as decaying states// Proc. Jpn. Acad. Ser. B. – 2008. – Vol.84. – P. 264.

UDC 539

Probe diagnostics of plasma generated by a volume source of fission fragments in the active zone of stationary nuclear reactor WWR-K

Kunakov S.[1], Son E.[2], Shapiyeva A.[1]

[1]*International University of Information Technologies, 34 "A"/8 "A" Manasa/Zhandosov str., 050040 Almaty, Kazakhstan*
[2]*Joint Institute of High Temperature AS, Russian Federation*
[*]*e-mail: sandybeck.kunakov@gmail.com*

This paper presents the theory and the experimental results of probe diagnostics for high-pressure nuclear induced plasma in the presence of negative ions and mathematical description based on the hydrodynamic approximation and methodological recommendations are given to define that concentrations of charged particles in the plasma on the basis of numerical calculations. $^3He + UF_6$ plasma is generated by the nuclear reaction products $^3He + n + p \rightarrow p + T + 0.76\ MeV$.

Key words: probe diagnostics, helium plasma, fission fragments, nuclear reactor.
PACS number(s): 28.41.-i

1 Introduction

The probe method is easy to implement and commonly used as an effective local experimental tool among plasma diagnostics methods. Nevertheless, the correct theoretical description of the electric currents formation in the region disturbed by electric probe is very complicated. As it's well known, the current-voltage characteristics (CVC) are used to define the concentration of charged particles and electrons temperature. The degree of ionization in nuclear induced plasma is supposed to be small $N_e \leq N_0$, where N_0 – the concentration of neutral atoms) and the frequency of electron collisions with electrons and ions in plasma is assumed to be negligible small compared with the electrons collisions with neutrals. The electron free flight length as well as the ions length is assumed to be much more less then the charged particles characteristic length. These physical conditions imply that the plasma is collisional and might be described in the hydrodynamical approximation. The major part of the experimental results implemented in nuclear test-reactor WWR-K is presented in paper [1].

The theory of electrostatic probes in the not-self-maintained plasma for the probes of different geometry and for the weakly ionized plasma of high-pressure flow were developed by Ulyanov [2], [3]. In this paper the disturbed zone was subdivided into the two zones: the region of charged layer, the region of diffusion layer.

In the paper [4] the asymptotic theory of spherical electrostatic probe is presented for the case of chemically active, weakly ionized high-pressure plasma in the presence of small concentrations of negative ions. It is also assumed that Debye radius is small compared with the probe size, and electron energetic length of relaxation is much more smaller then the length of microscopic scale, and function of electrons energy distribution is defined by local magnitudes of electron density and temperature.

2 The theory of electrostatic probe in nuclear induced plasma with negative ions

2.1Basic equations

We take the case of stationary plasma and the probe potential is different from the plasma potential. We shall take the distance from the probe till any point of disturbed by the probe region as a basic coordinate. The non dimensionless basic equations describing the formation of electron and ion currents might be presented in the following way:

$$\omega^+ \frac{d}{d\xi}\left(-\frac{dn^+}{d\xi} + \gamma n^+ \frac{d\Psi}{d\xi}\right) = 1 - an^e n^+ - bn^- n^+, \quad (1)$$

$$\omega^- \frac{d}{d\xi}\left(-\frac{dn^-}{d\xi} + \gamma n^- \frac{d\Psi}{d\xi}\right) = cn^e - bn^- n^+, \quad (2)$$

$$\omega^e \frac{d}{d\xi}(-\frac{dn^e}{d\xi} + n^e \frac{d\Psi}{d\xi}) = 1 - cn^e - an^e n^+, \quad (3)$$

$$\varepsilon \frac{d^2\Psi}{d\xi^2} = n^e - n^- + n^+, \quad (4)$$

where $\xi = \frac{r}{r_p}$, $\omega^+ = \frac{t_{ion}}{t_{D^+}}$, $\omega^- = \frac{t_{ion}}{t_{D^-}}$, $\omega^e = \frac{t_{ion}}{t_{D^e}}$,

$t_{ion} = \frac{n_\infty}{S}$, $t_{D_+} = \frac{r_p^2}{D_+}$, $t_{D_e} = \frac{r_p^2}{D_e}$, $t_{D_-} = \frac{r_p^2}{D_-}$,

$\varepsilon = (\frac{r_d}{r_p})^2 = \frac{KT_e}{4\pi e^2 n_\infty^+ r_p^2}$, $\Psi = \frac{\varphi}{\frac{kT_e}{e}}$, $a = \frac{\alpha_e (n_\infty^+)^2}{S}$,

$b = \frac{\alpha_i (n_\infty^+)^2}{S}$, $c = \frac{\beta n_\infty^+}{S}$, $\gamma = \frac{T_e}{T}$, $\delta = \frac{n_\infty^e}{n_\infty^+}$,

$S = \frac{n_{He_3} * \Phi * \sigma_f * E_0}{\Omega}$,

n^+, n^-, n^e – concentration of electrons, positive and negative ions, D^+, D^-, D^e, b^+, b^-, b^e – coefficients of diffusion and mobility of electrons, negative and positive ions, β – affinity coefficient [4] defining the formation of negative ions, r_p – probe radius, S – ionization rate, Φ – neutron flux density, σ_f – fission cross section of the helium-3, E_0 – the kinetic energy of the fission fragments, Ω – the energy value of the formation of an electron an ion pair, n_{He_3} – the helium-3 concentration.

Boundary conditions on the probe and on the limits of disturbed region are defined as follows:

$$n^+(1) = n^-(1) = n^e(1) = 0, \Psi(r_p) = \Psi_p, \quad (5)$$

$$n^+(\xi_1) = 1, n^-(\xi_1) = 1 - \delta, n^e(\xi_1) = \delta, \Psi(\xi_1) = 0, \quad (6)$$

where ξ_1 – the length of disturbed region.

2.2Charged layer

Following the results of work [2], we divide the disturbed region into two layers: the charged layer $1 \le \xi \le \xi_0$ and the layer of ambipolar diffusion $\xi_0 \le \xi \le \xi_1$.

In the charged layer the equations which form the probe currents of positive and negative particles presented as follows:

$$\omega^+ \frac{d}{d\xi}(\gamma n^+ \frac{d\Psi}{d\xi}) = 1, \quad (7)$$

$$\omega^- \frac{d}{d\xi}(\gamma n^- \frac{d\Psi}{d\xi}) = 0, \quad (8)$$

$$\omega^e \frac{d}{d\xi}(n^e \frac{d\Psi}{d\xi}) = 1, \quad (9)$$

$$\varepsilon \frac{d^2\Psi}{d\xi^2} = n^e - n^- + n^+. \quad (10)$$

From equations (7-10) the lengths of charged layer for the plane, cylindrical and spherical probes will be presented like these:

for plane probe:

$$r_0 = r_p[1 + \kappa_+^{-\frac{1}{2}} r_p^{-2}(\phi_p - \phi_0)]^{\frac{1}{2}}, \quad (11)$$

for cylindrical probe:

$$r_0 = r_p[1 + \sqrt{2}\kappa_+^{-\frac{1}{2}} r_p^{-2}(\phi_p - \phi_0)]^{\frac{1}{2}}, \quad (12)$$

for spherical probe:

$$r_0 = r_p[1 + \sqrt{3}\kappa_+^{-\frac{1}{2}} r_p^{-2}(\phi_p - \phi_0)]^{\frac{1}{2}}, \quad (13)$$

where $\kappa_+ = (\frac{4\pi e S}{b_+})^{\frac{1}{2}}$.

For the negative probe potential the electric currents on the plane, cylindrical and spherical probes are presented as follows:

for plane probe:

$$I_p = eSAr_0, \quad (14)$$

for cylindrical probe:

$$I_p = eS\frac{\phi_p - \phi_0}{\sqrt{\kappa_+}}L, \quad (15)$$

for spherical probe:

$$I_p = \frac{4}{3}\pi e S r_p^3[1 + \sqrt{\frac{3}{\kappa_+}}\frac{\phi_p - \phi_0}{r_p^2}]^{\frac{3}{2}}, \quad (16)$$

where A – plane probe area, L – length of cylindrical probe, and the lengths of charged layer for different geometry might be presented as follows:

If the full voltage drop is in the charged layer then following to [3] we have the simple way of charged particle concentration definition. This method is based on the use of linear part of electronic branch of CVC near the zero. Parameter δ varies from $0 \le \delta \le 1$. This an equality describes limited cases when plasma consists of only negative and positive ions or electrons and positive ions.

In the case when voltage drop is taken place in the charged layer the concentration of positive ions and parameter δ is defined from ion and electron branches of CVC by the following expressions (spherical probe) [5]:

$$n_{\infty}^{+} = \frac{J_{np}^{+}(1+\frac{3}{4}\frac{I_{np}}{\pi eSr_p^3})^{\frac{1}{3}}-1}{\varphi_{np} r_p (1+\frac{3}{4}\frac{I_{np}}{\pi eSr_p^3})^{\frac{2}{3}}}, \quad (17)$$

$$\delta = \frac{J_{np}^{-} - 4\pi e r_p b^{-} n_{\infty}^{+} \varphi_{pp} (1+\frac{J_{np}^{-}}{4\pi eSr_p^3})^{\frac{1}{3}}}{4\pi e r_p (b^e - b^{-}) \varphi_{pp} (1+\frac{J_{np}^{-}}{4\pi eSr_p^3})^{\frac{1}{3}}}, \quad (18)$$

where J^{+}_{np}, φ_{np} – probe current and negative probe potential, J^{-}_{np}, φ_{np} – probe current and positive probe potential.

2.3Ambipolar diffusion layer

Basic equations in diffusion layer:

$$\omega_a^{+} \frac{d}{d\xi}(-\frac{dn^{+}}{d\xi}) = 1 - an^e n^{+} - bn^{-} n^{+}, \quad (19)$$

$$\omega_a^{-} \frac{d}{d\xi}(-\frac{dn^{-}}{d\xi}) = cn^e - bn^{-} n^{+}, \quad (20)$$

$$\omega_a^{e} \frac{d}{d\xi}(-\frac{dn^{e}}{d\xi}) = 1 - cn^e - an^e n^{+}, \quad (21)$$

$$\varepsilon \frac{d^2\Psi}{d\xi^2} = n^e - n^{-} + n^{+}, \quad (22)$$

where $\omega_a^{+} = \frac{t_{ion}}{t_{D_a^{+}}}$, $\omega_a^{-} = \frac{t_{ion}}{t_{D_a^{-}}}$, $\omega_a^{e} = \frac{t_{ion}}{t_{D_a^{e}}}$.

Everywhere faraway from the probe the following relations are valid:

$$J^{+} - J^{-} - J^{e} = 0, \quad (23)$$

$$J_p = eJ^{+} + eZJ^{-} + eJ^{e}, \quad (24)$$

$$\frac{d\varphi}{dx} = -(\frac{D^{+} - (1-\delta)D^{-} - \delta D^{e}}{b^{+} + (1-\delta)b^{-} + \delta b^{e}}) \frac{dln(n^{+})}{dx}, \quad (25)$$

$$J^{+} = -D_a^{+} \frac{dn^{+}}{dx}, \quad (26)$$

$$J^{-} = -D_a^{-} \frac{dn^{-}}{dx}, \quad (27)$$

$$J^{e} = -D_a^{e} \frac{dn^{e}}{dx}, \quad (28)$$

where D_a^{+}, D_a^{-}, D_a^{e} – ambipolar diffusion coefficients:

$$D_a^{+} = \frac{\delta(D^{+}b^{e} + D^{e}b^{+}) + (1-\delta)(D^{+}b^{-} + D^{-}b^{+})}{b^{+} + (1-\delta)b^{-} + \delta b^{e}}, \quad (29)$$

$$D_a^{-} = \frac{(D^{+}b^{-} + D^{-}b^{+}) + \delta(D^{+}b^{e} + D^{e}b^{-})}{b^{+} + (1-\delta)b^{-} + \delta b^{e}}, \quad (30)$$

$$D_a^{+} = \frac{(D^{+}b^{e} + D^{e}b^{+})}{b^{+} + (1-\delta)b^{-} + \delta b^{e}}. \quad (31)$$

In diffusion layer for negative probe potentials electric currents for plane, cylindrical and spherical geometry are as follows:

for plane probe:

$$I_p = e(1+\frac{b_{+}}{b_{+} + (1-\delta)b_{-} + \delta b_e}) D_a^{+} n_{\infty}^{+} r_p^{-1} [\frac{2}{\omega_{+}}(1-\frac{\rho}{3})]^{\frac{1}{2}} A \quad (32)$$

for cylindrical probe:

$$I_p = 2\pi e(1+\frac{b_{+}}{b_{+} + (1-\delta)b_{-} + \delta b_e}) D_a^{+} n_{\infty}^{+} L [\frac{2}{\omega_{+}}(1-\frac{\rho}{3})]^{\frac{1}{2}} (1+\frac{\phi_p - \phi_0}{\sqrt{\kappa} r_p^2})^{\frac{1}{2}} \quad (33)$$

for spherical probe:

$$I_p = \pi e(1+\frac{b_{+}}{b_{+} + (1-\delta)b_{-} + \delta b_e}) D_a^{+} n_{\infty}^{+} r_p [\frac{2}{\omega_{+}}(1-\frac{\rho}{3})]^{\frac{1}{2}} (1+\frac{\phi_p - \phi_0}{\sqrt{\kappa} r_p^2})^{\frac{1}{2}}. \quad (34)$$

The value n_0 of boundary concentration for the negative and positive probe is defined by the following:

$$(\frac{r_p}{r_d})^2 n_0^+ = \vartheta[\frac{2}{\omega_+}\frac{1}{(n_0^+)^2}(1-\frac{\rho}{3}-n_0^+ + \frac{\rho(n_0^+)^3}{3}) - \frac{1}{n_0^+}(1-\rho(n_0^+)^2)], \quad (35)$$

$$(\frac{r_p}{r_d})^2 n_0^e = \vartheta[\frac{2}{\omega_e}\frac{1}{(n_0^e)^2}(\delta-\frac{\delta\rho}{3}-n_0^e + \frac{\rho(n_0^e)^3}{3}) - \frac{1}{n_0^e}(1-\rho(n_0^e)^2)]. \quad (36)$$

If the main potential drop is taken place in diffusion zone then we have the following:

$$n_0^+ = (\frac{\vartheta\varepsilon}{\omega_+})^{\frac{1}{3}}[2(1-\frac{1}{3}\rho)]^{\frac{1}{3}}, \quad (37)$$

$$n_0^e = (\frac{\vartheta\varepsilon}{\omega_+})^{\frac{1}{3}}[2\delta(1-\frac{1}{3}\rho)]^{\frac{1}{3}}, \quad (38)$$

where $\vartheta = \frac{D_+ - (1-\delta)D_- - \delta D_e}{b_+ + (1-\delta)b_- + \delta b_e}(\frac{kT_e}{e})^{-1}$,

$\omega_+ = \frac{D_{a+}n_{+\infty}^2}{Sr_p^2}$, $\omega_e = \frac{D_{ae}n_{+\infty}^2}{Sr_p^2}$, $\varepsilon = (\frac{r_d}{r_p})^2$,

$\rho = \frac{\alpha_e n_{+\infty}^2}{S}\delta + \frac{\alpha_i n_{+\infty}^2}{S}(1-\delta)$, $\delta = \frac{n_\infty^e}{n_\infty^+}$.

3 The electrostatic probe experimental data obtained in plasma $^3He + UF_6$ diagnostics in the active zone of nuclear reactor WWR-K

WWR-K reactor is research test-reactor working on thermal neutrons. Moderator as well as reflector of neutron flux as well as the cooler is artesian water desalinated by ion-exchange absorber AB-17, KU-2. Active zone consists from assembly of uranium fuel elements which are placed in hexagonal space symmetry. The high of the test-reactor is about $60cm$. The cooling system of the reactor is made by two independent cooling cycles. The cooler of the first cycle is transferring the heat of fuel elements with the speed 5 m/s^{-1}, and the volume rate 1600 m^3/h. The cooling temperature is maintained on the constant level and does not exceed 400 ^oC.

The vertical projection of the active zone is presented on the figure 1a. The active zone is set in the vessel with artesian water and surrounded by biological protection shield made from the cast iron and heavy concrete. The water layer over the active zone is about 4 meters. The top of the apparatus is closed by rotating iron cover with a bung, through which the core services, loading and unloading through the vertical experimental channel samples and testing products are carried out.

The central testing channel of active zone is located in the beryllium moderator which is set in the centre of active zone replacing four or seven fuel elements (which corresponds to the diameter testing channels 96 mm and 140 mm). The reactor experiments are specific and the operation with experimental sets are connected with the ionising radiation.

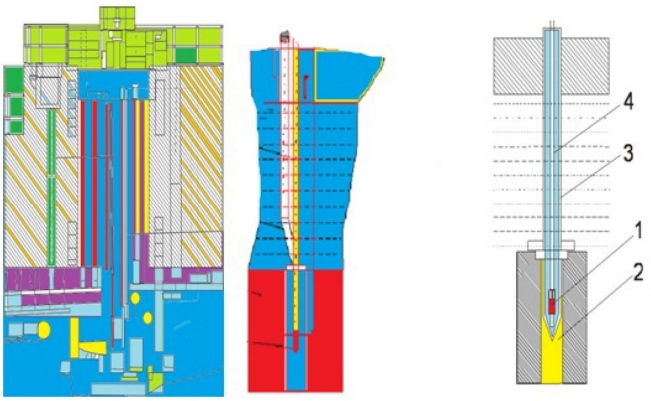

Figure 1 – WWR-K reactor scheme, diagnostic channel and diagnostic cell
(1 – testing ampule, 2 – active zone, 3 – diagnostic channel, 4 – signal wires))

The main specific feature of reactor experiments is that the experimental measurements control might be done only remotely and the experimental set might be used only single time. Due to the high induced radiation the experimental construction elements are not available. The construction elements as well as the optical parts should be highly resistant to the radiation flux. As a source of radiation the ^3He isotope is used which has large cross-section value with thermal neutrons $5.3 \cdot 10 - 21\ cm^2$ (5.3 * 10 – 21 *cm*2) and the undergoing products of this reaction $He(n,p)T$ will cause the ionization of the testing gas mixture:

$$^3He + n \rightarrow p + T + (0.76\text{MeV}), \qquad (39)$$

The input energy per unit of volume might be evaluated by the following expression:

$$P = 1.65J * n\,\text{W/cm}^2, \qquad (40)$$

where J – the flux of thermal neutrons in the units $10^{14}\ cm^{-2}c^{-1}$, and n – isotope pressure in ^3He atm.

To ensure uniform volume ionization it is needed to choose in the reactive zone of reactor some definite place with the homogeneous neutron flux distribution. Taking to the concentration the vertical and horizontal neutron flux distribution within the central diagnostic channel of the WWR-K reactor (Figure 2) the area within diameter 30 mm and the high h = 300 *mm* (from –150 mm to +150 mm) was chosen to run the planned experiments and it is corresponding to the most suitable uniform neutron flux distribution. Following to this preferences the ampules size was taking around the $d \leq 30$ *mm,* $h \leq$ 300 *mm*. Nuclear reactions in ionising testing gas should be chosen due to the following conditions: sufficiently enough fission cross section and large value of released energy of its products.

Following to the internal WWR-K constructional elements and specific features of the reactor experiments the special construction of diagnostic channel was designed to insure effective radiation of testing gases in the centre of active zone. The probe diagnostic experimental channel to study plasma created by the products of nuclear reactions is schematically presented in the Figure 1. The diagnostic channel is made from the steel tube. At the same picture the diagnostic ampule is presented which has the cylindrical form with the diameter $40mm$, at the bottom of which the special inlet was attached to fill into the cell testing gas mixture of a given composition. At the top side of the ampule the special vacuum sealed entry was installed at the tips of which the cylindrical, spherical and plane probe are attached. The probes are fixed on the ceramic holders. Not operating part of the probe is protected from the plasma contact by isolator made from ceramic tubes. Heating, pumping and gas filling of the testing mixture were conducted on the high vacuum experimental set (10^{-11} *Torr*).

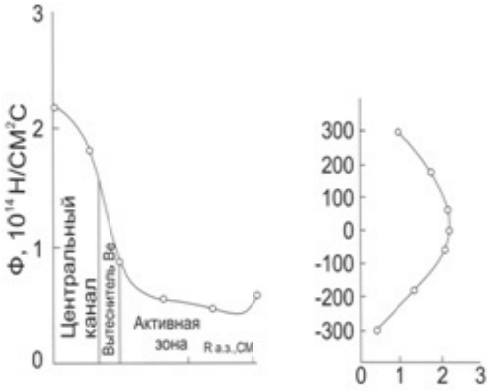

Figure 2 – Space energy distribution of the thermal neutron fluxes along the vertical and horizontal projections within the active zone of WWR-K reactor

The interaction of electrons, ions, neutrals and fission fragments with the probe wall different physical phenomena are taking place that namely the scattering of incident particles, secondary electronic emission, cathode spraying and absorption processes and thin film creation. With the temperature (higher then 800*K*) these processes are associated with the evaporation neutral and charged particles from the metal surface and thermo-electronic emission is appearing. The secondary electronic emission initiated by the positive ions, photons and metastable atoms collisions against the metal surface of the probe and has sufficient influence on the formation electric currents on the negative probe. Secondary emission will cause the increase of the ion electric currents on the probe. The positive probe is not so influenced by the secondary electrons due to the slowing electric field.

The number of secondary electrons created by the incident ion striking the surface of the metal is called the secondary emission coefficient γ [6]. The value of the γ is defined most of all by the kinetic energy of the incident particles the physical and chemical structure of the metal surface.

The value of the γ within the region $10^{-1} – 10^{-2}$. The emission current density caused by nuclear

fragments interactions with the wall might be evaluated from the following expression:

$$J = \frac{eN_i \bar{\upsilon}_i}{4} \gamma_{ei}, \qquad (41)$$

where N_i , $\bar{\upsilon}_i$, γ_{ei} вЂ“ concentration, average velocity, secondary emission coefficient of the fission fragments, ions or excited atoms.

The secondary electrons emission also might be caused by photons and the density of the electric current emission caused by the electromagnetic radiation is defined by expression:

$$J = \frac{eN_i^*}{4\pi\mu_\Phi} \gamma_\Phi, \qquad (42)$$

where N^* – excited atoms concentrations emitting radiation, τ вЂ“ life-time of the excited atom, ($\tau = 10^{-7} - 10^{-8} s$), μ_Φ – photon absorption coefficient ($\mu_\Phi \approx 10^2$), γ_Φ – photoelectrons quantum output ($\gamma_\Phi \approx 10^{-4}$). Evaluations show that the emission electric current is less than – $<10^{-8}$ Acm^{-2}.

The isolating properties of ceramic tubes in the centre of active zone are not so sufficiently changed and value of electric current leakage might be neglected compared with the electric current on the probe. The evaluation shows that density of emission current $<10^{-8}$ Acm^{-2} while the density of measured electric current of the probe is not less then $<10^{-6}$ Acm^{-2}. To avoid the cathode spray effect on the CVC the probes are made from refractory metals like wolfram, stainless steel. Not operating part of the probe is protected by isolator which has the following composition: $Si \sim 47\%$, $Al2O3 \sim 22\%$, $Fe2O3 \sim 5.7\%$, $CaO \sim 2\%$, $MgO \sim 3\%$, $K2O \sim 3\%$, $N2O \sim 1.5\%$, $SO3 \sim 0.41\%$, $H2O \sim 0.02\%$.

3.1Probe diagnostics of the plasma of gaseous mixture $^3He : N_2 : O_2$

For different geometry of the probe measurements in variety of density of the testing gas and neutron flux 1 – Φ = 1.5 10^{12} $cm^{-2}s^{-1}$, 2 – Φ = 3.0 · $10^{\Phi}12$ $cm^{-2}s^{-1}$ are presented on the figure 3,4,5. The results of the experiments in plasma $^3He : N_2 : O_2$ are presented in the Table 1, where the formulas (17-18) have been used.

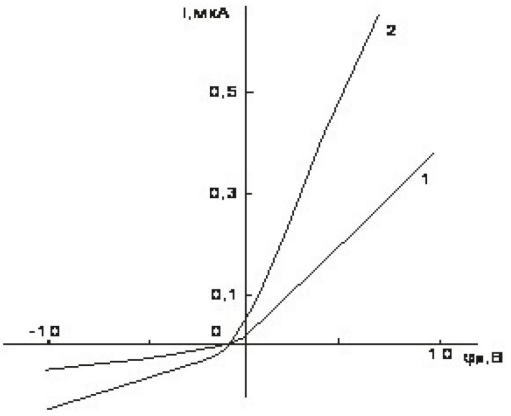

Figure 3 – CVC of cylindrical probe in plasma $^3He : N_2 : O_2(760:1:4Torr)1 - \Phi =$ $= 1.5 \cdot 10^{12} \text{cm}^{-2}s^{-1}, 2 - \Phi = 3.0 \cdot 10^{\Phi}12\text{cm}^{-2}s^{-1}$

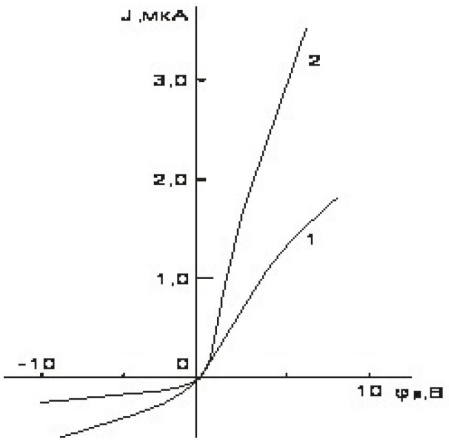

Figure 4 – CVC of cylindrical probe in plasma $^3He : N_2 : O_2(760:1:4Torr)1 - \Phi =$ $= 1.5 \cdot 10^{13} \text{cm}^{-2}s^{-1}, 2 - \Phi = 3.0 \cdot 10^{\Phi}13\text{cm}^{-2}s^{-1}$

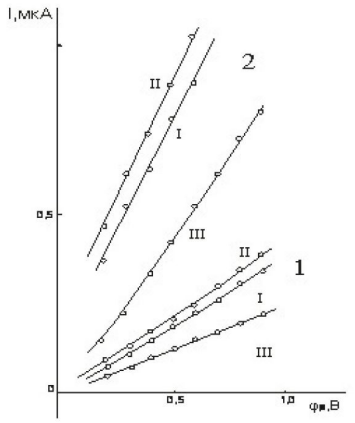

Figure 5 – electronic CVC branches $^3He : N_2 : O_2(760:1:4Torr)1 - \Phi =$ $= 1.5 \cdot 10^{12} \text{cm}^{-2}s^{-1}, 2 - \Phi = 3.0 \cdot 10^{\Phi}12\text{cm}^{-2}s^{-1}$.
1 – cylindrical probe, 2 – spherical probe, 3 – plane probe

The values of the electron and ion concentrations obtained from the experimental CVC measurements are presented in the Table 1. The presented results are in satisfactory agreement between each other and compared with the theoretical calculations.

Table 1 – The charged particles concentrations obtained from experimental measurements in plasma of gaseous mixture $^3He - N_2 - O_2$

Reactorpower	Gas temperature, K	Probe	Probe current 10^{-7} A	n^+10^{10} cm^{-3} [11]	n^+10^{10} cm^{-3} [11]	$\sigma^\infty 10^{-6}$ Ohm^{-1} cm^{-1}	n^e10^{10} cm^{-3} [11]
		I	0.7	1.7	1.8	36.6	1.4
200	340	II	0.4	1.8	1.8	35.1	1.4
		I	1.8	2.9	2.8	66.1	2.4
500	350	II	0.8	2.7	3.0	64.2	2.5
		I	4.6	5.2	3.9	87.1	4.0
800	375	II	2.5	5.5	4.2	90.4	4.3
		I	7.0	6.2	4.5	105.0	5.0
1000	400	II	3.8	6.4	4.8	107.9	5.3

CVC of the semispherical (R = 0.1 *cm*) and plane probe (R = 0.1 *cm*), were measured in the helium plasma of special purity which was equal to 0.0001%. Pumping, heating and an ampule filling was accomplished on the high level vacuum experimental set. ^3He plasma of the pressure 430*Torr* was studied under the different power levels 200, 500, 800, 100 kW., which corresponded to the neutral flux values $\Phi = (6, 15, 24, 30) * 10^{11}\ cm^{-2}s^{-1}$. The temperature was measured by thermocouple device and was equal to 340, 350, 373, 400 K which corresponded to each previously mentioned power level of reactor.

The typical probe CVC measured in plasma created in the active zone of reactor are presented in the Figure (6-8).

As it might be seen from this pictures in the region not so large potentials of the probe $(0 \div 0.1)B$ it is possible to distinguish linear part of CVC.

The values of conductivity obtained from the linear part of CVC probe of different geometrical configuration are presented in the Table 2. As it follows from the Table 2 the maximum experimental error is about 20%.

Table 2 – The conductivity values obtained from the experiment $^3He - N_2 - O_2$

Power mW	Probe	Cell's number [1]	Cell's number [2]	Cell's number [3]	Cell's number [7]
		σ_∞ 10^{-6} Ohm^{-1}cm^{-1}	σ_∞ 10^{-6} Ohm^{-1}cm^{-1}	σ_∞ 10^{-6} Ohm^{-1}cm^{-1}	σ_∞ 10^{-6} Ohm^{-1}cm^{-1}
	1	0.5	0.4	0.6	0.5
0.5	2	0.6	0.5	0.7	0.6
	3	0.7	0.7	0.8	0.7
	1	1.4	1.2	1.5	1.4
1.0	2	1.4	1.2	1.7	1.4
	3	1.9	1.6	1.9	1.8

3.2 Uranium hexafluoride plasma probe diagnostics (UF_6)

The experimental study of high pressure UF_6 plasma created by a volume source of fission fragments is a part of large scientific programs connected with the nuclear energy transformation in other different application forms. The UF_6 probe diagnostics in the active zone of WWR-K are presented on the Figures (6-9). Uranium hexafluoride UF_6 also might be used as a fuel in nuclear reactor [7].

In spite of definite number of obstacles which are coming dealing with materials like the fuel of nuclear

reactors as well as due to it is high chemical aggression the future prospects of UF_6 use and applications are very attractive.

The calculations of the charges particle concentrations in the uranium hexafluoride UF_6 are presented in the Table 3 [7].

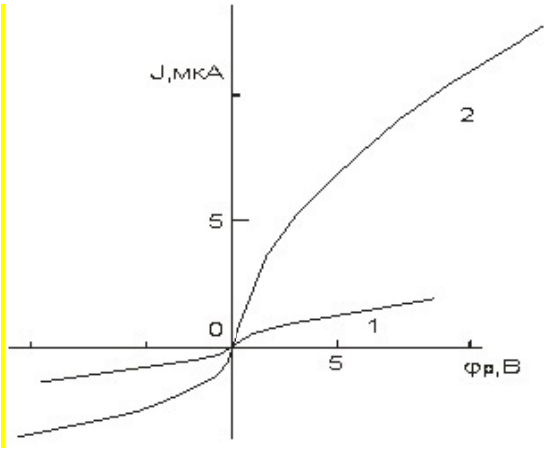

Figure 6 – CVC of UF_6 plasma measured under the different levels of the nuclear WWR-K power ($1-1.1012n/cm^2s-2s, 2-11013n/cm^2s-2s$)

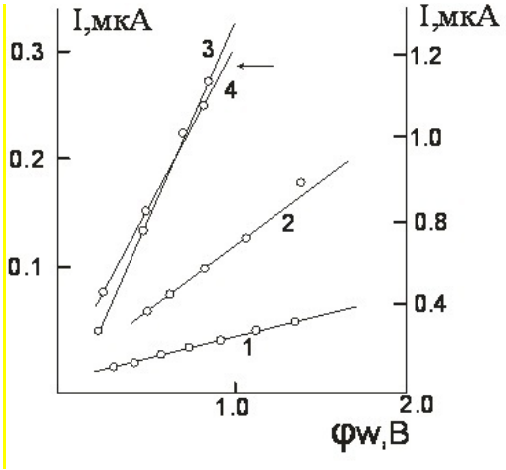

Figure 7 – CVC of UF_6 plasma measured under the different levels of the nuclear WWR-K power (small positive potentials)

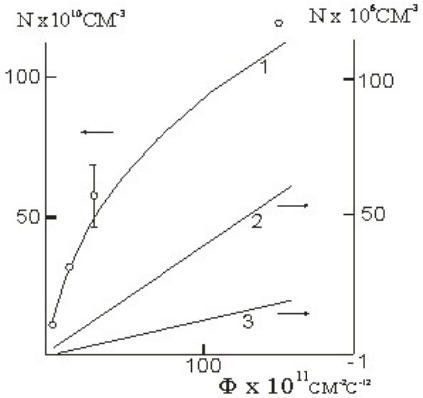

Figure 8 – The charged particle concentrations dependences on the neutron flux level (– calculations; 0 – experiment; 1 – UF_{6^+}; 2 – N_e; 3 – UF_{5^-})

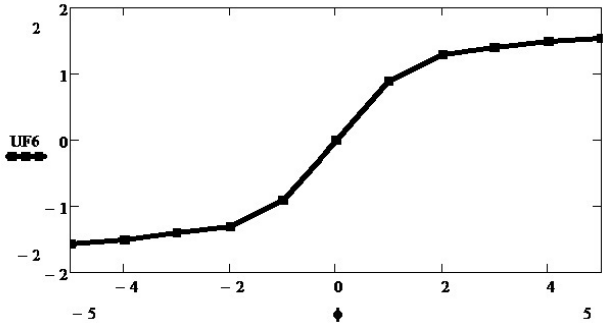

Figure 9 – CVC of UF_6 plasma (typical CVC)

Table 3 – Uranium hexafluoride UF_6 component concentrations, cm^{-3}

N_e $5.9*10^6$	UF_{6^+} $2.6*10^{11}$	UF_{6^-} $2.6*10^{11}$	UF_{5^-} $2.1*10^6$	F^- $4.2*10^4$
F $7.7*10^{13}$	F_2 $7.7*10^{16}$	UF_5 $3.9*10^{14}$	UF_4 $4.0*10^4$	

As it follows from the Table 3, the major part of negative ions in the given mixture is UF_{6^-}. This concentration is equal to the concentration UF_{6^+} with the accuracy of 0.0001%. The concentrations of the ions UF_{6^+} defined by ionization and recombination rates with UF_{6^-}. The electron concentration is relatively small. As the theoretical calculations show that the ratio of electrons density

to the density of negative ions is equal to 10^{-4}. Also it follows from theoretical calculations that the electron concentration is defined by ionization rate and affinity rate to molecules UF_6.

Conclusion

1. The precise experimental CVC measurements of the plane and spherical probe in helium plasma are carried ut within the pressure of the gas 430 *Torr* and the nuclear reactor power level under 100, 200, 500, 800, 1000 *kW*. Electron concentrations are defined by used the linear CVC dependence of the positive probe [5].

2. The uranium hexafluoride CVC measurements are also carried out. It was found that at the nuclear power levels 100-200 *kW* negative and positive parts of the UF_6 CVC are symmetric ones. From the CVC symmetry it might be concluded that the electrons influence on the plasma conductivity is very small $b^- n^- \gg b_e n_e$ but $b^- \ll b_e$, then $n_- \gg n_e$

References

[1] M. Benilov. Teoriya electricheskih zondov v potokah slaboionizirovannoi plazmy vysokogo davleniya. Teplofizika vysokih temperatur. –1988. – Vol. 26. – P. 5.

[2] M. Bektursunova. S. Kunakov. Asimptoticheskaya teoriya sfericheskogo electrostaticheskogo zonda v stolknovitelnoi plazme. obrazovannoi produktami yadernyh reakcyi. Teplofizika vysokih temperatur. – 1992. – Vol.30. – P. 2.

[3] S.K. Kunakov. E.Ye. Son. A. Ye. Shapiyeva. Probe diagnostics of 3He+UF6 plasma. generated in the core of nuclear reactor WWW–K // International Journal of Mathematics and Physics. – 2015. – Vol. 6. – No.1. – P. 69–74.

[4] I. Bronshtein. B.Fraiman. Vtorichnaya electronnaya emissiya. – Moscow, 1969.

[5] V. Dmitrievski. Ye. Voinov. S. Tetelbaum. Primenenie UF6 v yadernyh energeticheskih ustanovkah // Atomnaya energiya. – 1970. – N.4. – Vol. 29. – P. 45–52.

UDC 539

Analyzing power of Inverse Diproton Photodisintegration at Intermediate Energies

Baimurzinova B.

Laboratory of Nuclear Problems, Joint Institute for Nuclear Research, RU-141980 Dubna, Russia
e-mail:baymurzinova@jinr.ru

The reaction $\gamma + \{pp\}_s \rightarrow p + p$, where diproton $\{pp\}_s$ is a proton pair in $^1S_0$ state, is a spin-isospin partner of the fundamental reaction of deuteron photodisintegration. The inverse reaction, the hard bremsstrahlung $p + p \rightarrow \gamma + \{pp\}_s$, has been observed with the ANKE spectometer at COSY-Jülich. In addition to differential cross section measured earlier, in this work it's analyzing power has been measured at forward angles at several energies in the region of Δ(1232) isobar exictation.

Key words: diproton, analyzing power, hard bremsstrahlung.
PACS number(s): 25.40.Ep, 13.60.-r, 25.20.Dc

1 Introduction

The formation of a so-called "diproton", i.e. a proton pair $\{pp\}$, in $^1S_0$ state, is being researched at ANKE collaboration in various processes: $pd \rightarrow \{pp\}_s\, n$, $pp \rightarrow \{pp\}_s\, \pi^0$, $pp \rightarrow \{pp\}_s\, \gamma$ [1-5]. Such reactions are of interest for several reasons. Firstly, they are the elementary inelastic processes in few-nucleon systems which could give valuable information on dynamics of nucleon-nucleon interaction. Secondly, restriction to only one partial wave (*S*-wave) in the final state considerably simplifies the reactions theoretical consideration in comparison to other reactions of this kind, for example deuteron photodisintegration $\gamma d \rightarrow pn$. The diproton photodisintegration $\gamma\{pp\}_s \rightarrow pp$ is kinematicly very similar to $\gamma d \rightarrow pn$, however dynamically they significantly differ from each other. The matter is that the quantum numbers of a diproton state ($I = 1$, $S = 0$, $L = 0$) differ from the corresponding quantum numbers of a deuteron ($I = 0$, $S = 1$, $L = 0.2$). As a result multipole contributions will also be significantly different. Therefore the data received for these two reactions mutually supplement each other, indicating that we should study such processes more carefully.

In absence of a free bound diproton, $\gamma\{pp\}_s \rightarrow pp$ is traditionally investigated for diproton which bound within a nucleus. At ANKE an alternative approach was applied for the first time – the study of the inverse reaction $pp \rightarrow \gamma\{pp\}_s$ [4], free from background created by the deuteron photoabsorption. Particulary, the goal of this work is to find analyzing power of this reaction.

2 Measurements and analysis

The experiment was carried out in Germany using ANKE facility of the synchroton storage ring COSY-Jülich (Fig. 0) [6]. A hydrogen cluster-jet target was positioned in the proton beam and secondary particles were detected with wire chambers and scintillation hodoscope. The proton beam was transversely polarized with it's polarization direction varying from up to down. The trajectories and three-momenta of the particles were reconstructed.

The first step in the identification of our reaction was the selection of two coincident protons among all the detected pairs of positively charged particles. The scintillation hodoscope allowed measurement of the difference between the times of flight from the target to detector for two recorded particles. If we assume the masses of the particles, we can also calculate this time of difference, using the measured momenta and trajectories. If our assumption was correct then these two values would coincide. With time resolution better than 2 ns, the comparison of this value with that calculated from the measured particle momenta and trajectories led to a very good identification of proton pairs. At low excitation energy $E_{pp} < 3$ MeV the diproton is predominantely in the $^1S_0$ state. The resolution of the ANKE setup $\sigma(E_{pp}) < 0.6$ MeV allowed reliable selection of $E_{pp} <$ 3 MeV diprotons.

As the next step, histograms for missing mass squared were created at $T_p = 0.500, 0.550, 0.700$ GeV (Fig. 1). There is a clear visible γ peak that could be separated from the pion peak associated with the *pp*

$\rightarrow pp\pi^0$ reaction. The peak shapes were obtained by a detailed Monte Carlo simulation at each energy, which took into account all the known features of the setup. The free parameters of interest used to fit the missing-mass spectra were the number of events in the γ peak and the number of events in the pion peak. In order to compensate for the lack of knowledge of the beam spatial distribution, additional parameters were inserted into the fits: a shift of the pion peak position and correction factors for the γ and pion peak widths. The results of the fit can be seen in Fig. 1 as well.

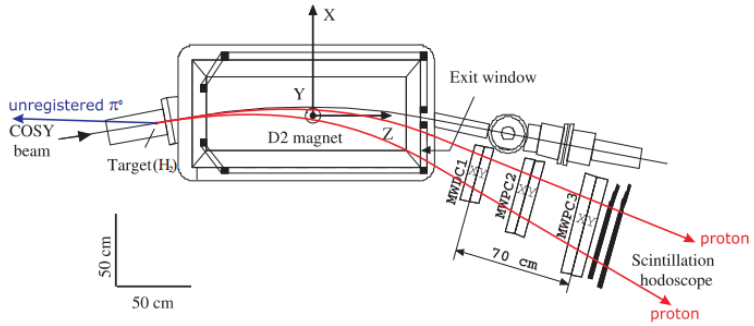

Figure 1 – Experimental setup

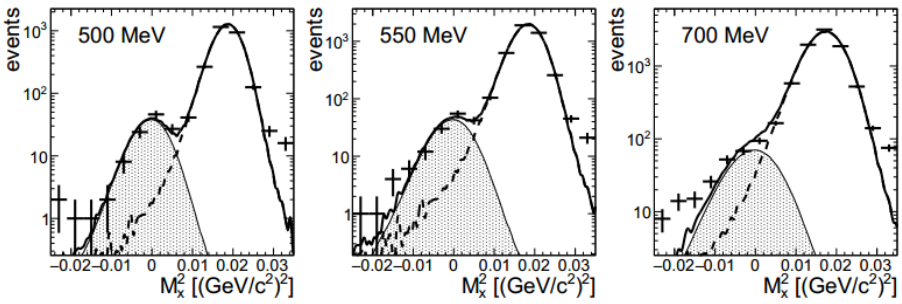

Figure 2 – Distribution of the missing mass squared in the $p + p \rightarrow \{pp\}_s + X$

To estimate the angular dependence of the analyzing power, the events were divided into two θ_{pp} intervals 5–13°, 13–30° and separate fits were made for each of these ranges. Firstly, we had to find polarization assymetry given by equation (1).

$$\varepsilon = \frac{N_\uparrow / L_\uparrow - N_\downarrow / L_\downarrow}{N_\uparrow / L_\uparrow + N_\downarrow / L_\downarrow}, \qquad (1)$$

where $N_\uparrow$ and $N_\downarrow$ are the numbers of events with beam proton spin up and down, and $L_\uparrow$ and $L_\downarrow$ are the corresponding luminosities. It is needed to calculate the analyzing power using equation (2).

$$A_y = \frac{\varepsilon}{P\langle \cos\phi_{pp} \rangle}, \qquad (2)$$

where P is the transverse polarisation of the beam and $\langle \cos\phi_{pp} \rangle$ the average over the diproton azimuthal angular distribution. Different approaches were applied to obtain the analyzing power. The numbers of events can be determined either by fitting separately $N_\uparrow$ and $N_\downarrow$, or directly $N_\uparrow - N_\downarrow$ and $N_\uparrow = N_\downarrow$ histograms. Concerning $\cos\phi_{pp}$ there are two possibilities, either to divide by the average value of $\cos\phi_{pp}$ distribution or to correct by $\cos\phi_{pp}$ event-by-event. Hence, four approaches were applied, each repeated for fine and gross histogram binning. These 8 values with errors were averaged. The dispersion of the values was considered as a systematic error. Polarization P was estimated using the known values of A_y for elastic pp and $pp \rightarrow d\pi^+$ reactions, registered in parallel with our reaction.

3 Results and outlook

In Fig. 2 and Table 0 the preliminary results are shown for analyzing power of the $pp \rightarrow \gamma\{pp\}_s$ reaction at T_p = 0.500, 0.550, 0.700 GeV.

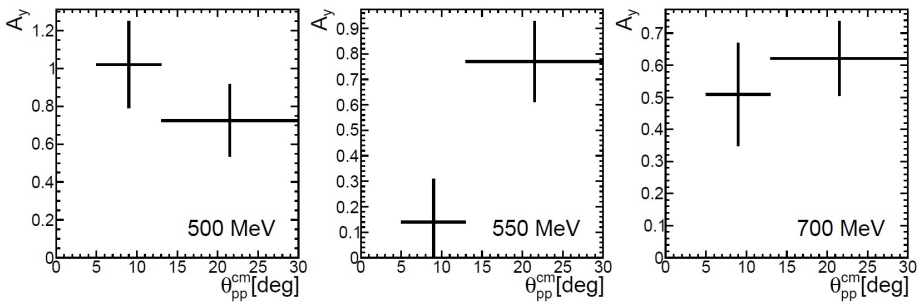

Figure 3 – Analyzing power for reaction $p + p \to \gamma + \{pp\}_s$, preliminary results.

Table 1 – Numerical values of analyzing power with systematical and statistical errors, preliminary results.

	500	550	700
$5 - 13^\circ$	$1.02 \pm 1.80 \pm 0.02$	$0.14 \pm 1.03 \pm 0.67$	$0.51 \pm 1.23 \pm 0.014$
$13 - 30^\circ$	$0.72 \pm 1.45 \pm 0.03$	$0.77 \pm 0.99 \pm 0.01$	$0.62 \pm 0.92 \pm 0.002$

Since multipole contributions $M1$ and non-spin-flip part of $E1$ are forbidden, it might be sufficient to retain only $E2$, $M2$ and spin-flip part of $E1$. The qualitative estimate of the results [7] suggests that there may be significant contribution of the $M2$ multipole contrary to the predictions of [8]. The numerical evaluation of $E1$, $E2$, $M2$ multipole contributions to the data is in progress.

Acknowledgements

The authors wish to think other members of the ANKE collaboration for their help and assistance in the running of the experiment and in the data analysis.

References

[1] S. Dymov et al.Deuteron breakup pd→{pp}sn with forward emission of a fast 1S0 diproton// Phys. Rev. C. – 2010. –Vol. 81. –P. 044001.

[2] V. Kurbatov et al.Energy dependence of forward 1S0 diproton production in the pp→ppπ0 reaction// Phys. Lett. B. – 2008. – Vol. 661. –P. 22.

[3] D. Tsirkov et al.Differential cross section and analysing power of the pp→{pp}sπ0 reaction at 353 MeV// Phys. Lett. B. – 2012. – Vol. 712. – P. 370.

[4] V. Komarov et al.Observation of Inverse Diproton Photodisintegration at Intermediate Energies// Phys. Rev. Lett. – 2008. – Vol. 101. – P. 102501.

[5] D. Tsirkov et al.Energy dependence of hard bremsstrahlung production in proton–proton collisions in the Δ(1232) region// J. Phys. G: Nucl. Part. Phys. – 2010. –Vol. 37. –P. 105005.

[6] S. Barsov et al.ANKE, a new facility for medium energy hadron physics at COSY-Jülich// Nucl. Instrum. Methods. Phys. Res. – 2001. –Vol. 462. –P. 364.

[7] P. Wilhelm et al. Signatures from polarization observables for photon absorption on a 1S0 proton pair // Nucl. Phys. A. – 1996. –Vol 597. – P. 613.

[8] P. Wilhelm et al. Photon absorption on a proton-proton pair in He3// Phys. Lett. C. – 1995. – Vol.51. – P. 2841.